

Repair Strategies for Corroded Steel Bridge Girder End Regions

by

Jason Anthony Mash

Bachelor of Science in Civil Engineering, West Virginia University, 2012

Master of Science in Civil Engineering, West Virginia University, 2015

Submitted to the Graduate Faculty of the
Swanson School of Engineering in partial fulfillment
of the requirements for the degree of
Doctor of Philosophy

University of Pittsburgh

2022

UNIVERSITY OF PITTSBURGH

SWANSON SCHOOL OF ENGINEERING

This dissertation was presented

by

Jason Anthony Mash

It was defended on

May 16, 2022

and approved by

Dr. John Brigham, PhD, Associate Professor, Civil and Environmental Engineering

Dr. Amirhossein Alavi, PhD, Assistant Professor, Civil and Environmental Engineering

Dr. Joel Haight, PhD, Professor, Industrial Engineering

Dissertation Director: Dr. Kent Harries, PhD, Professor, Civil and Environmental Engineering

Copyright © by Jason Anthony Mash

2022

Repair Strategies for Corroded Steel Bridge Girder End Regions

Jason Anthony Mash, PhD

University of Pittsburgh, 2022

The objective of this research is to investigate practical *in situ* repair methods, using high performance and traditional materials, which can be applied to corroded and/or damaged steel girder ends. The focus of the study is on girder end repairs associated with corrosion and damage typically resulting from leaking deck joints. Resulting corrosion damage patterns may be exacerbated or mitigated by local details such as the presence of stiffeners or the nature of the bearing provided. Through an integrated analytical and experimental study, the existing capacity of archetypal corroded end regions was assessed. Techniques for providing *in situ* rehabilitation of these regions using both high performance and conventional means were explored. Six W24 girders were tested over short shear spans. The girders had significant deterioration including section loss on the web and holes (100% section loss) over the bearing region. For each girder, End A was tested under static load conditions to failure. If an acceptable result was achieved after testing End A, End B was fatigue conditioned for 1 million cycles and subsequently tested to failure in a similar manner to End A. Repair methods considered included conventional bolted steel repairs, ultra-high performance and normal strength reinforced concrete encasement and adhesively applied fiber-reinforced polymer (FRP) plates. All methods but FRP plates were able to restore the original, undeteriorated bearing and shear capacities of the girders. A nonlinear finite element model was developed for each repair method. These models clearly identified the transition of failure modes based on repair methods and identified the ability of stiffer bearing

stiffeners to permit tension field action to develop in the girder end panels. Finally an extensive qualitative assessment of all repair methods considered is presented.

Table of Contents

Acknowledgments	xviii
1.0 Literature Review	1
1.1 Introduction and Motivation	1
1.2 Characterizing Beam End Corrosion	3
1.3 Residual Capacity of Bearing Regions Exhibiting Beam End Corrosion	7
1.3.1 Web Shear	7
1.3.2 Web Yield due to Bearing	9
1.3.3 Web Crippling due to Bearing	9
1.3.4 Bearing Stiffeners	11
1.4 Experimental Study of Bearing Regions Exhibiting Beam End Corrosion	12
1.5 Computational Study of Bearing Regions Exhibiting Beam End Corrosion	14
1.5.1 MassDOT Report 19-008	16
1.6 Conventional Structural Repair of Beam End Corrosion Damage	19
1.6.1 Temporary Support During Repair	21
1.7 Partial Encasement of Damaged Beam Ends in High Performance Concrete	21
1.7.1 Ultra High-Performance Concrete	22
1.7.2 Implementation of UHPC	24
1.7.3 University of Connecticut Study	25
1.7.3.1 Zmerta (2015)	25
1.7.3.2 McMullen (2019)	34
1.7.4 Field Applications of UHPC Repair	39

1.7.5 UHPC versus Conventional Concrete	40
1.8 Shear Stud Capacity	43
1.8.1 Other Shear Connectors	45
1.9 Fiber Reinforced Polymer (FRP) Based Repairs	47
1.9.1 Mitigating Crippling Induced by High Local Stresses	50
1.9.2 FRP Repair of Corroded Beam Ends.....	51
2.0 Condition Review of Pennsylvania Bridges.....	54
2.1 Girder Section Distortion.....	57
2.2 Previous repairs	58
2.3 Selection of Archetypal Damage	59
3.0 Repair Strategies	62
3.1 Sample Designs	63
3.2 Conventional Steel Repair	64
3.2.1 Pros of Conventional Steel Repair.....	64
3.2.2 Cons of Conventional Steel Repair	65
3.2.3 Sample Design: Conventional Steel Retrofit.....	66
3.3 UHPC Encasement	67
3.3.1 Pros of UHPC Encasement.....	67
3.3.2 Cons of UHPC Encasement.....	68
3.4 Concrete Encasement	68
3.4.1 Pros of Concrete Encasement	69
3.4.2 Cons of Concrete Encasement	69
3.5 Shear Studs for Encasement Repairs	69

3.6 Sample Design: Concrete Encasement	70
3.7 Repair Using Adhesively Bonded FRP Plate or Sections.....	72
3.7.1 Pros of Adhesively Bonded FRP Repairs.....	73
3.7.2 Cons of Adhesively Bonded FRP Repairs.....	73
3.7.3 Sample Design: Bonded FRP Repair – Case 1	73
3.7.4 Sample Design: Bonded FRP Repair – Case 2	76
3.8 Wet Lay Up FRP Repairs	77
3.8.1 Pros of Wet Lay-up	78
3.8.2 Cons of Wet Lay-up	78
3.8.3 Sample Design: Bonded FRP Repair – Case 1	78
3.9 Selection of Adhesive, Surface Preparation, and Details for Adhesive Bonding....	80
3.10 Section Replacement	81
4.0 Test Specimens	83
4.1 Constraints on Test Specimen Selection.....	83
4.2 Test Specimen Design.....	84
4.3 As-Received Test Specimens.....	87
4.3.1 Impact of As-Received Details	90
4.3.2 Test Specimen Material Properties	91
4.4 Repair Designs	91
4.4.1 Girder 3 - Conventional Bolted Steel Repair.....	92
4.4.2 Girder 4 - UHPC Repair.....	94
4.4.3 Girder 5 - Reinforced Concrete (RC) Repair	96
4.4.4 Girder 6 - Glass Fiber Reinforced Polymer (GFRP) Repair	98

5.0 Experimental Testing Program	102
5.1 Test Set Up	102
5.1.1 Monotonic Tests to Failure.....	102
5.1.2 Fatigue Conditioning	103
5.1.3 Instrumentation.....	104
5.2 Girder End A Monotonic Test Results	105
5.2.1 Girder End 1A	109
5.2.2 Girder End 2A	110
5.2.3 Girder End 3A	111
5.2.4 Girder End 4A	112
5.2.5 Girder 5A	113
5.2.6 Girder End 6A	115
5.3 Fatigue Conditioning (Girder End B).....	118
5.3.1 Girder End 3B	119
5.3.2 Girder End 4B	120
5.3.3 Girder End 5B	120
5.4 Girder End B Post Fatigue Conditioning Monotonic Test Results.....	121
5.4.1 Girder 3B	125
5.4.2 Girder End 4B	126
5.4.3 Girder End 5B	126
5.5 Composite Behavior of Reinforced Concrete Encased Girder 5.....	127
5.6 Interpretation of Test Results and Correlation with <i>In Situ</i> Conditions	129
6.0 Finite Element Modeling	130

6.1 Finite Element Model Parameters	131
6.1.1 Modeling Steel Girders	131
6.1.2 Modeling Section Loss	132
6.1.3 Steel Material Properties	132
6.1.4 Concrete Material Properties.....	134
6.1.5 Concrete Material Model	134
6.1.5.1 Concrete Compression	135
6.1.5.2 Concrete Tension	135
6.1.5.3 Failure Surface.....	136
6.1.5.4 Shear Retention.....	137
6.1.6 Internal Reinforcing Steel	138
6.1.7 Boundary Conditions	138
6.1.7.1 Interaction with Bearing Plate	139
6.1.7.2 Applied Load.....	139
6.1.8 Contact Interfaces around 100% Section Loss	140
6.1.9 Geometric Imperfections	140
6.2 Modeling Test Specimens.....	142
6.2.1 Girder 1A	142
6.2.2 Girder 2A	143
6.2.3 Girder 3A	144
6.2.4 Girder 4A	145
6.2.5 Girder 5A	146
6.3 Modeling Archetypal Plate Girders.....	147

6.3.1 Undamaged Plate Girder.....	148
6.3.2 Case I Archetypal Damage.....	149
6.3.3 Conventional Bolted Steel Repair.....	151
6.3.4 UHPC Encasement.....	152
6.3.5 NSC Encasement	153
6.3.6 Tension Field Action	155
6.3.7 Concrete Encasement.....	156
7.0 Conclusions and Future Work.....	158
7.1 Conclusions of Experimental Results	158
7.2 Conclusions of Numerical Modeling Results	159
7.3 Qualitative Assessment of Repair Methods	160
7.4 Future Work	164
Appendix A - Test Specimen Fabrication Drawings	166
Appendix B - Test Specimen Web Thickness Measurements.....	168
Bibliography	169

List of Tables

Table 1 Beam End Corrosion Pattern Characterization.....	4
Table 2 Values of Parameters Required for Equations 1-10 and 1-11.....	11
Table 3 Experimental Results Reported by Gerasimidis and Brena	12
Table 4 Experimental Results Reported by Kim	14
Table 5 Summary of Analytical Studies of Beam End Corrosion	15
Table 6 Typical Properties of UHPC, HPC, and NSC	23
Table 7 Girder geometry and test results reported	27
Table 8 FE Models of UHPC Repaired Girder End Regions	33
Table 9 Test Results Reported by McMullen	37
Table 10 Typical Properties of FRP Systems	49
Table 11 Condition Review Summary	56
Table 12 Bearing Region Capacities of Archetypal Damage Cases	61
Table 13 Summary of Specimen Design Checks for W24x55	86
Table 14 “Corrosion Damage” and Web Thickness	88
Table 15 Test Matrix	91
Table 16 UHPC Mix Protocol and Measured Material Properties	95
Table 17 RC Mix and Measured Material Properties	97
Table 18 Material Properties of Pultruded GFRP and Adhesive	100
Table 19 Summary of Key Parameters of Monotonic End A Tests	107
Table 20 Summary of Key Parameters of Monotonic End B Tests	123
Table 21 Typical Properties of UHPC, HPC, and NSC.....	136

Table 22 Summary of Predicted Capacities for Test Specimen Modeling	142
Table 23 Summary of Predicted Capacities for Plate Girder Modeling.....	148
Table 24 Bearing Stiffener Stiffness and Observed Behavior	156
Table 25 Web Shear Capacity	157
Table 26 Quantitative Assessment of Repair Techniques	162
Table 27 Test Specimen Web Thickness Measurements.....	168

List of Figures

Figure 1 National and International Descriptions of Beam End Corrosion	2
Figure 2 Examples of Beam End Corrosion	3
Figure 3 Details of FE Model of Specimen 1	18
Figure 4 Steel Beam End Repair – Replacing Deteriorated Region	20
Figure 5 Steel Patch Repairs of Deteriorated Beam End Regions	20
Figure 6 Test Set-up and Damaged Girders.....	28
Figure 7 UHPC Repaired Girder	30
Figure 8 FE Models of Test Girders.....	31
Figure 9 Test Set Up and Damage Reported	35
Figure 10 UHPC Repairs.....	36
Figure 11 Failure Modes of UHPC Encased Girders	37
Figure 12 Field Implementation of UHPC Repair.....	39
Figure 13 Field Implentation of UHPC.....	40
Figure 14 Masters Road Belle River Bridge.....	40
Figure 15 Push Out Tests of HSC and UHPC.....	42
Figure 16 Alternatives to Welded Shear Stud Connectors	47
Figure 17 Use of FRP to Mitigate Crippling	51
Figure 18 Schematic Representation of CFRP Repair	51
Figure 19 CFRP Repair of Corroded Bearing Stiffener	52
Figure 20 Shear Repair of Corroded Beam End using CFRP.....	53
Figure 21 Geographic Distribution of 15 Bridges Reviewed	55

Figure 22 Lateral Distortion of Web	57
Figure 23 Flexural Distortion of Flange.....	58
Figure 24 Previous Repairs Identified in Review of Bridge Inspection Reports	59
Figure 25 Archetypal Damaged Cases	60
Figure 26 Conventional Steel Repair for Damage Case I	66
Figure 27 Conceptual Representation of Concrete Encasement Repairs.....	72
Figure 28 Adhesive Bonded FRP Repairs for Plate Girders	75
Figure 29 Adhesive Bonded FRP Repairs for Rolled Girders.....	77
Figure 30 Details of Wet Lay Up CFRP Web Patch.....	80
Figure 31 Dapped Plate Girders	82
Figure 32 Proposed W24x55 Specimen.....	87
Figure 33 Section Distortion of Girder Specimens	90
Figure 34 Bolted Steel Repair Detail for Girder 3.....	93
Figure 35 UHPC Repair Detail for Girder 4.....	96
Figure 36 Reinforced Concrete Repair Detail for Girder 5.....	98
Figure 37 GFRP Repair Detail for Girder 6	101
Figure 38 Overall Views of Test Set Ups	102
Figure 39 Instrumentation	105
Figure 40 Shear Stress versus Displacement Curves from Monotonic Tests	108
Figure 41 Principal Shear Strains	109
Figure 42 Girder 1A Following Testing.....	110
Figure 43 Girder 2A During and After Testing	111
Figure 44 Girder 3A Following Testing.....	112

Figure 45 Girder 4A Following Testing	113
Figure 46 Girder 5A During and Following Testing	115
Figure 47 Girder 6A Following Testing	117
Figure 48 Shear Strain and Displacement Histories during Fatigue Conditioning.....	119
Figure 49 Cracking Observed during Fatigue Conditioning of Girder 5B	121
Figure 50 Shear Stress versus Displacement Curves from Monotonic Tests	124
Figure 51 Principal Shear Strains	124
Figure 52 Girder 5B Following Testing	125
Figure 53 Girder 4B Following Testing	126
Figure 54 Girder 5B Following Testing	127
Figure 55 Proportion of Shear Resisted by Steel Web in Girder 5	129
Figure 56 Mesh Geometry	132
Figure 57 Engineering (experimental) and True (ABAQUS) Stress Strain	133
Figure 58 ABAQUS Smeared Crack Concrete Model.....	137
Figure 59 Modeling Internal Reinforcing Steel of Girder 5A.....	138
Figure 60 Numerical Model Boundary Conditions	140
Figure 61 Girder Imperfections.....	141
Figure 62 Girder 1A Loaded End Elevation	143
Figure 63 Bearing Region Failure of Girder 2A	144
Figure 64 Bolted Steel Repair	145
Figure 65 UHPC Encasement Repair	146
Figure 66 NSC Encasement Repair	147
Figure 67 Undamaged Girder Predicted Behavior at Failure	149

Figure 68 Bearing Region Failure of Case I	150
Figure 69 Failure of Case I Damaged Girder.....	150
Figure 70 Bolted Steel Repair	152
Figure 71 UHPC Encasement Repair	153
Figure 72 NSC Encasement Repair.....	154
Figure 73 Test Specimen Fabrication Drawings	166
Figure 74 Test Specimen Fabrication Details.....	167

Acknowledgments

I would like to express my gratitude to Dr. Kent Harries for his guidance and support during my graduate studies and dissertation. I thank him for his insight and knowledge. His work ethic has been inspirational. Further, I would like to thank my committee, Dr. John Brigham, Dr. Amir Alavi, and Dr. Joel Haight for their support and assistance. I am very appreciative of Chase Rogers and Charles “Scooter” Hager for their countless hours of help in the lab.

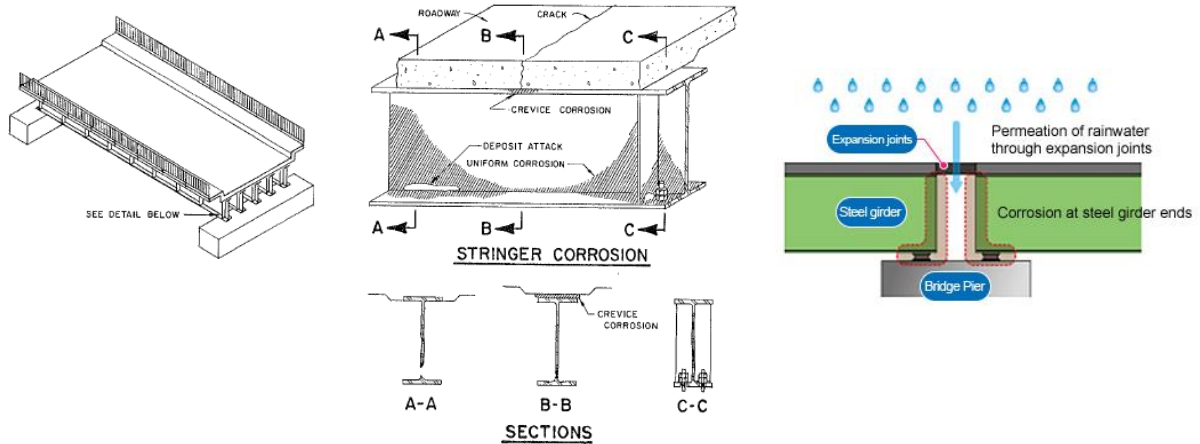
I would also like to thank the Lord above, my wife Emily, and my daughters Grace and Rosalie. I am very grateful for my wife and daughters’ love and patience throughout this process and dealing with all the late nights.

Finally, I would like to thank the Pennsylvania Department of Transportation for funding this research and to High Steel Structures for fabrication services.

1.0 Literature Review

1.1 Introduction and Motivation

The objective of this research is to investigate practical *in situ* repair methods, using high performance and traditional materials, which can be applied to corroded and/or damaged steel girder ends. The focus of the study is on girder end repairs associated with corrosion and damage typically resulting from leaking deck joints as shown schematically in Figure 1. Resulting corrosion damage patterns may be exacerbated or mitigated by local details such as the presence of stiffeners or the nature of the bearing provided. Effects and extent of the corrosion are also affected by the environment in which the bridge is situated (including micro-climates beneath the bridge) and sea or road salt exposure. Local air circulation in the vicinity of girder bearings and the accumulation of debris (trapping moisture) also effect the extent and pattern of damage. Such damage will be collectively referred to as ‘beam end corrosion’ in this dissertation. Typical examples of beam end corrosion found in the literature, illustrating the spectra of damage possible, are shown Figure 2. A review of beam end corrosion examples in Pennsylvania is provided in Chapter 2.



- a) description of stringer corrosion in NCHRP Report 333 (1990)
- b) description of expansion joint leaking (Hanshin Expressway 2020)

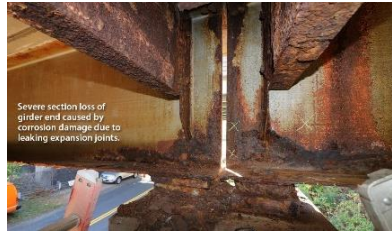
Figure 1 National and International Descriptions of Beam End Corrosion

PennDOT DM-4 §5.5.2.6b states in part: “Deteriorated steel beam ends shall be cleaned, strengthened if needed, painted and protected from future deterioration by providing continuity or leakproof joints.” The scope of this research is structural strengthening including assessment of extant conditions, particularly the residual capacity that may be relied upon following strengthening.

It should be clear that any strengthening should be accompanied by mitigation of the causes of deterioration. This will often involve, as DM-4 §5.5.2.6b states, painting and repairs to the deck and/or joints. These are beyond the scope of this study although will be addressed when they are integral to a strengthening scheme.



Connecticut
(Zmeta et al. 2017)



Connecticut
(McMullen and Zaghi 2020)



Nebraska
(Al Badran 2003)



Web failure, Korea
(Ahn et al. 2013)



New York
(Bao et al. 2018)



Japan
(Liu et al. 2011)

Figure 2 Examples of Beam End Corrosion

1.2 Characterizing Beam End Corrosion

Gerasimidis and Brena (2019) report a review of 168 bridges in Massachusetts. From this, 808 corroded beam ends were reviewed, and a method of categorizing beam end damage was established. This characterization is shown in Table 1 and will be adopted (with some revision) to describe beam end corrosion damage described in the present study. In addition to the beam end corrosion pattern, the degree of section loss is also reported. Damage may also be characterized as a combination of the patterns shown. For example, the image in Table 1 accompanying M1 shows a through hole (M1) surrounded by a generally triangular corroded area (W5). Multiple holes are also common (e.g., M1+M3).

Patterns W1 and W3 (Table 1) were most commonly reported: 84% of observed cases for beams with end diaphragms and 76% for cases without. In most cases (59%), the vertical extent

of the corroded region (C_H) was less than 20% of the overall beam depth. Nonetheless, in 18% of cases, the corroded region extended the full beam depth (Gerasimidis and Brena 2019). Furthermore, Gerasimidis and Brena reported 15% of beam ends reviewed had through-web holes (M1 – M4).

Flange corrosion was characterized by Gerasimidis and Brena by its length along the flange and section loss (an example is seen in the image accompanying W1). Flange section loss was assumed to extend across the entire flange width.

Gerasimidis and Brena were silent on damage to bearing stiffeners. Considering that the role of a bearing stiffener is the same as that of the web at a bearing, the same damage patterns can be used. For bearing stiffeners, patterns W1 and M1 are typical and should be reported.

Table 1 Beam End Corrosion Pattern Characterization (adapted from Gerasimidis and Brena 2019)

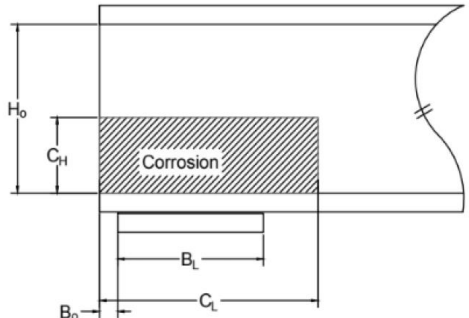

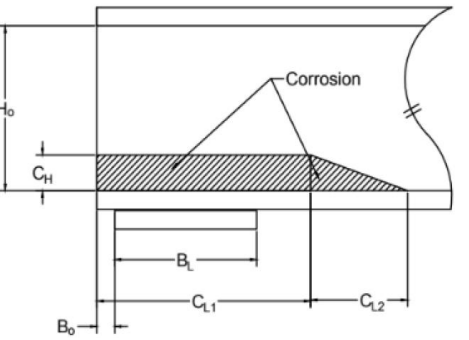

Pattern	Drawing	Representative Image
<p>W1</p> <p>Rectangular shape corrosion pattern at the beam end above the bearing.</p>		
<p>W2</p> <p>Similar to W1, with the addition of a triangular-shaped corrosion area at the end of the rectangular shape.</p>		

Table 1 (continued)

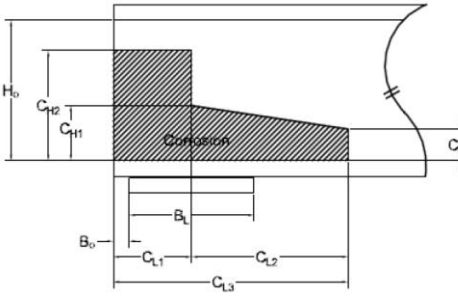

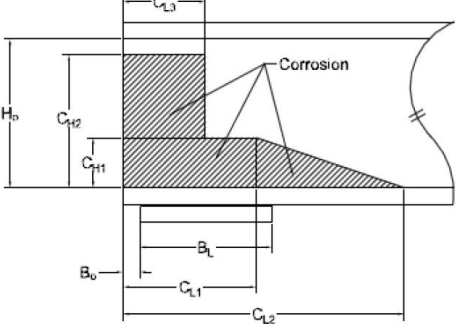

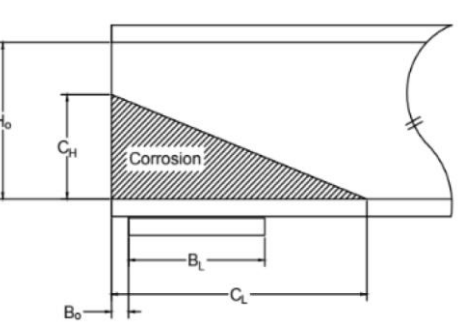

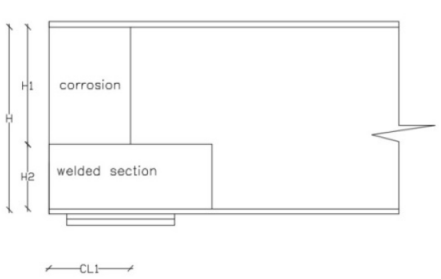

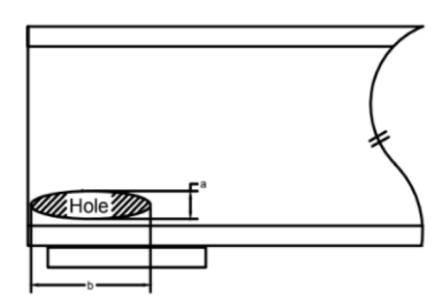

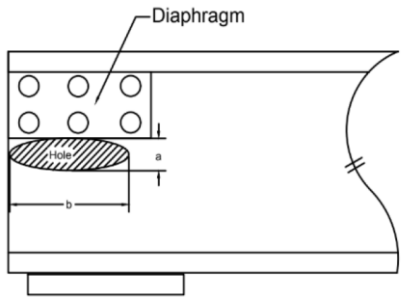

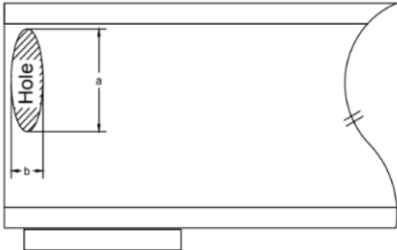

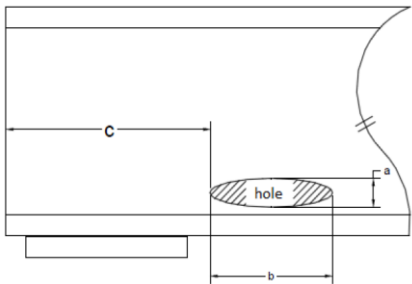

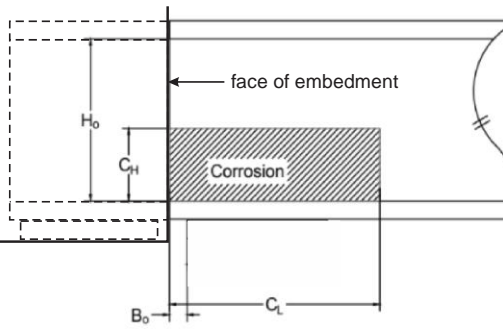

<p>W3</p> <p>More complex shape generally described by three areas of corrosion.</p>	 <p>The diagram shows a cross-section of a beam with a complex corrosion area shaded in hatching. The corrosion area is defined by three regions: a top rectangular area with width C_{L1} and height C_{H1}, a middle trapezoidal area with top width C_{L2} and bottom width C_{L3} and height C_{H2}, and a bottom rectangular area with width C_{L4} and height C_{H3}. The total height of the beam is H_0 and the total width is B_0. The corrosion area is labeled 'Corrosion'.</p>	 <p>A photograph showing a close-up of a corroded steel beam. The corrosion is extensive, with a large area of rust and scale. The beam is supported by a concrete pier.</p>
<p>W4</p> <p>Modification of W3 to having variation of complex shape.</p>	 <p>The diagram shows a cross-section of a beam with a complex corrosion area shaded in hatching. The corrosion area is defined by three regions: a top rectangular area with width C_{L1} and height C_{H1}, a middle trapezoidal area with top width C_{L2} and bottom width C_{L3} and height C_{H2}, and a bottom rectangular area with width C_{L4} and height C_{H3}. The total height of the beam is H_0 and the total width is B_0. The corrosion area is labeled 'Corrosion'.</p>	 <p>A photograph showing a close-up of a corroded steel beam. The corrosion is extensive, with a large area of rust and scale. The beam is supported by a concrete pier.</p>
<p>W5</p> <p>Triangular shape corroded area.</p>	 <p>The diagram shows a cross-section of a beam with a triangular corrosion area shaded in hatching. The corrosion area is defined by a base width C_L and a height C_H. The total height of the beam is H_0 and the total width is B_0. The corrosion area is labeled 'Corrosion'.</p>	 <p>A photograph showing a close-up of a corroded steel beam. The corrosion is extensive, with a large area of rust and scale. The beam is supported by a concrete pier.</p>
<p>W6</p> <p>Corrosion above welded [repair] plate.</p>	 <p>The diagram shows a cross-section of a beam with a corrosion area shaded in hatching. The corrosion area is defined by a height H_1 and a width C_L. The total height of the beam is H_0 and the total width is B_0. The corrosion area is labeled 'corrosion'. Below the corrosion area is a 'welded section'.</p>	 <p>A photograph showing a close-up of a corroded steel beam. The corrosion is extensive, with a large area of rust and scale. The beam is supported by a concrete pier.</p>
<p>M1</p> <p>Hole through lower part of web over bearing.</p>	 <p>The diagram shows a cross-section of a beam with a hole through the lower part of the web over a bearing. The hole is defined by a width b and a height c. The total height of the beam is H_0 and the total width is B_0. The hole is labeled 'Hole'.</p>	 <p>A photograph showing a close-up of a corroded steel beam. The corrosion is extensive, with a large area of rust and scale. The beam is supported by a concrete pier. The text 'Span #1, Beam #11, End face' is visible in the top right corner.</p>

Table 1 (continued)

<p>M2</p> <p>Hole below diaphragm.</p>		
<p>M3</p> <p>Hole through top part of beam.</p>		
<p>M4</p> <p>Hole through lower part of beam away from bearing.</p>		
<p>E-W1</p> <p>Rectangular shape corrosion pattern at the face of the beam embedment into the diaphragm</p> <p>Adding E- to all other patterns shifts point of reference to face of embedment.</p>		

1.3 Residual Capacity of Bearing Regions Exhibiting Beam End Corrosion

The following three subsections report AASHTO-LRFD (2020) prescribed capacity calculations for web shear buckling, bearing-induced web yielding and bearing-induced web crippling, respectively. In order to rate an existing structure having beam end corrosion, these equations are applied using the corroded web geometry as described.

1.3.1 Web Shear

The shear capacity of an end panel of a stiffened web is given as:

$$V_{cr} = \phi C [0.58 F_y D t_w] \quad \text{Equation 1-1}$$

Where F_y = yield strength of web plate

D = depth of the web plate

t_w = average thickness of the web accounting for loss of section due to corrosion

$\phi = 1.0$ for shear

Collectively, the term in brackets in Equation 1-1 is the web plastic shear capacity. Web instability is accounted for using the coefficient C , the ratio of shear buckling resistance to the shear yield strength:

$$\frac{D}{t_w} \leq 1.12 \sqrt{\frac{Ek}{F_y}} \quad C = 1 \quad \text{Equation 1-2}$$

$$1.12 \sqrt{\frac{Ek}{F_y}} < \frac{D}{t_w} \leq 1.40 \sqrt{\frac{Ek}{F_y}} \quad C = \frac{1.12}{D/t_w} \sqrt{\frac{Ek}{F_y}} \quad \text{Equation 1-3}$$

$$\frac{D}{t_w} > 1.40 \sqrt{\frac{Ek}{F_y}} \quad C = \frac{1.57}{(D/t_w)^2} \frac{Ek}{F_y} \quad \text{Equation 1-4}$$

Where E = Young's modulus for steel = 29,000 ksi = 200 GPa

$k = 5 + 5(d_o/D)^2$ for stiffened web panels having stiffener spacing d_o

$k = 5$ for unstiffened web panels

NCHRP *Report 333* (Kulicki 1990) states that buckling capacity of corroded webs may be assessed using Equation 1-1 with t_w taken as the nominal uncorroded web thickness, t_{web} , and applying a factor related to the ratio of corroded web thickness to nominal web thickness:

$$\varphi = (t_w/t_{web})^3 \quad \text{Equation 1-5}$$

Similarly, Ahn et al. (2013) reported a reduction factor for accounting for web corrosion which is applied to the nominal shear capacity of the section; i.e., Equation 1-1 with t_w taken as the nominal uncorroded web thickness (t_{web}). The strength reduction factor is given as a function of affected web volume:

$$\varphi = 0.7368 + \left[0.2859 / \left(1 + e^{-\left(\frac{C_c/C_s - 8.8318}{-3.4666} \right)} \right) \right] \quad \text{Equation 1-6}$$

Where C_c = volume of the corroded web panel

C_s = volume of the uncorroded web panel

1.3.2 Web Yield due to Bearing

The yield capacity of a web at the beam end subject to a concentrated compressive (or tensile) load is:

$$R_{n,yield} = \phi_b(2.5K + N)F_y t_{wc} \quad \text{Equation 1-7}$$

Where K = distance from the outer face of the flange to the web toe of the fillet; if the fillet size is unknown, $K = t_f$ is a conservative approximation; where t_f is the thickness of the flange subject to bearing.

N = length of the bearing

t_{wc} = average thickness of the web within the bottom 4 in. of the web height over the length $2.5K + N$ (Gerasimidis and Brena 2019)

$\phi_b = 1.0$ for bearing

In applying Equation 1-7, through web holes (M1 in Table 1) are accounted for in the calculation of t_{wc} by including regions of zero thickness in the calculation of average thickness. In the calculations presented by Gerasimidis and Brena, N is reduced to account for through web holes and t_{wc} is calculated based on remaining steel. While mathematically the same, the presentation adopted here results in a slightly less complex calculation.

1.3.3 Web Crippling due to Bearing

The web crippling (local instability) capacity at a girder bearing is:

$$\text{for } N/d > 0.2 \quad R_{n,crip} = \phi_w 0.4 t_{wc}^2 \left[1 + \left(\frac{4N}{d} - 0.2 \right) \left(\frac{t_{wc}}{t_f} \right)^{1.5} \right] \sqrt{\frac{E F_y t_f}{t_{wc}}} \quad \text{Equation 1-8}$$

$$\text{for } N/d \leq 0.2 \quad R_{n,crip} = \phi_w 0.4 t_{wc}^2 \left[+3 \left(\frac{N}{d} \right) \left(\frac{t_{wc}}{t_f} \right)^{1.5} \right] \sqrt{\frac{E F_y t_f}{t_{wc}}} \quad \text{Equation 1-9}$$

Where d = total depth of the steel section

t_f = thickness of the flange subject to bearing

$\phi_w = 1.0$ for web crippling.

For interior pier reactions of continuous beams and beams having an extension beyond the bearing greater than or equal to $d/2$, $R_{n,crip}$ is found as twice that calculated using Equation 1-9. Once again, crippling is affected only immediately above the bearing and the calculation of t_{wc} is the same as that given for Equation 1-7.

Gerasimidis and Brena (2019) recognize that non-uniform web corrosion results in ‘amplitude imperfections’, i.e., the load path through the web is no longer planar due to material loss. Real out-of-plane distortions of the web may also exist. Such imperfections will further reduce the web crippling capacity. Based on regression analysis of hundreds of corrosion scenarios, Equations 1-8 and 1-9 are modified as follows:

for $N/d > 0.2$:

$$R_{n,crip} = \phi_w \left[a \sqrt{E F_{yw} t_f} t_{wcc}^{1.5} + b \left(\frac{d}{3N} \right) \left(\frac{4N}{d} - 0.2 \right) \sqrt{E F_{yw} t_f} \left(\frac{t_{wcc}^2}{t_f} \right)^{1.5} \right] \left(\frac{CL}{N+md} \right)^h \quad \text{Equation 1-10}$$

for $N/d \leq 0.2$:

$$R_{n,crip} = \phi_w \left[a \sqrt{E F_{yw} t_f} t_{wc}^{1.2} + b \left(\frac{N}{d} \right) \sqrt{E F_{yw} t_f} \left(\frac{t_{wcc}^2}{t_f} \right)^{1.5} \right] \left(\frac{t_{wcc}}{t_{web}} \right)^h \quad \text{Equation 1-11}$$

Where t_{wcc} = average remaining thickness of the web within the bottom 4 in. of the web height over the length $md + N$

t_{web} = nominal uncorroded web thickness

the remaining empirically derived parameters are given in Table 2

Table 2 Values of Parameters Required for Equations 1-10 and 1-11

	for $N/d > 0.2$			for $N/d \leq 0.2$		
Imperfection amplitude	t_{web}	$0.5t_{web}$	$0.1t_{web}$	t_{web}	$0.5t_{web}$	$0.1t_{web}$
a	0.37	0.32	0.57	0.33	0.32	0.38
b	0.17	0.50	0.23	0	0.17	0
h	0.10	0.40	0.40	0.40	0.20	0.15
m	0.20	0.20	0.10	0.10	0.10	0

1.3.4 Bearing Stiffeners

The presence of adequate bearing stiffeners mitigates the web yield and crippling limit states reported in Section 1.3.2 and 1.3.3 (see AASHTO LRFD (2020) §6.10.11.2). The capacity of the fitted ends of a bearing stiffener is:

$$R_{sb} = \phi_b 1.4 A_{pn} F_y \quad \text{Equation 1-12}$$

Where A_{pn} = the area of the stiffener bearing upon the flange

$\phi_b = 1.0$ for bearing

The axial resistance of a bearing stiffener arrangement is:

$$P_{sb} = \phi_c \pi^2 E A_g / (0.75 D / r)^2 \leq A_g F_y \quad \text{Equation 1-13}$$

Where $\phi_c = 0.95$ for compression.

For a conventional arrangement having $b_{sb} \times t_{sb}$ bearing stiffeners on both sides of the web, the gross stiffener area, A_g , and radius of gyration, r , may be [marginally conservatively] approximated as: $A_g = 2b_{sb}t_{sb}$ and $r = 0.289(2b_{sb})$. Corrosion of bearing stiffeners is captured by

reducing the thickness t_{sb} to account for partial section loss and reducing b_{sb} for instances of 100% loss of stiffener section.

As a result of section loss, corroded bearing stiffeners may fall below the AASHTO-prescribed slenderness limit intended to prevent local buckling of the stiffener and therefore become inadequate to serve their intended role. In order to adequately behave as a bearing stiffener Equation 1-14 must be satisfied.

$$b_{sb} \leq 0.48t_{sb}(E/F_y)^{0.5} \quad \text{Equation 1-14}$$

1.4 Experimental Study of Bearing Regions Exhibiting Beam End Corrosion

Gerasimidis and Brena (2019) and subsequently Tzortzinis et al. (2019) report tests of six corroded beam end specimens obtained from two decommissioned bridges (Table 3). The unstiffened beam segments were tested over simple spans of 25 feet (Specimens 1-3) or 20 feet (Specimens 4-6) with the load applied 5 feet from the tested end in all cases. This results in different shear span-to depth ratios of 1.8 and 2.9 for Specimens 1-3 and 4-6, respectively. All beams had extensive section loss at the bearings, and many had significant holes leading to very low predicted capacities (Table 3).

Table 3 Experimental Results Reported by Gerasimidis and Brena (2019)

Specimen	1	2	3	4	5	6
Shape	33WF125			21WF73		
bearing failure load (kips)	99.1	67.6	84.3	42.8	30.9	40.9
predicted bearing failure load (Eq. 7) (kips)	38.3	102.2	0	91.5	17.6	6.1

Specimens 3 and 6 were both reported to have large holes over the bearing resulting in the very low predicted capacities in Table 3. When tested, these holes ‘collapsed’, and the residual capacity reported resulted from the edges of the holes coming into contact and subsequently transmitting bearing forces.

In Gerasimidis and Brena, only bearing failures (i.e., web yield and crippling) were considered. However, the authors report that the failures of Specimens 1 and 5 were “characterized by a buckling wave appearing in the web” and Specimen 4 exhibited a “long wave instability” which interacted with web crippling.

The low-test capacity of Specimen 2 was affected by a significant web imperfection which initiated the authors’ development of Equations 1-8 and 1-9 to account for this. Subsequent recalculation of the capacity using Equations 1-8 of this specimen reduced the predicted capacity 21% to 81.2 kips.

Although not discussed by Gerasimidis and Brena, the relatively high degree of variability and unpredictable behaviors of the highly damaged decommissioned beam ends suggests that residual capacity of the steel section may be unreliable in repair scenarios; that is, the repair may need to be able to resist the entire demand at the bearing without relying on residual capacity of the corroded beam.

Kim et al. (2013) report five large scale tests of specimens having a depth of 31.5 in. The 15/64 in. webs had artificially induced (machined) uniform section loss of 5/64 in. or 10/64 in. over the lower 4 in. or 8 in. of the web (Table 4). The specimens were tested in a simple span arrangement such that each half of the beam represented a single shear panel. Bearing stiffeners were used to mitigate local failures and thus, in this study, only the web shear (Equation 1-1) is assessed. Results and predicted capacities are summarized in Table 4.

Table 4 Experimental Results Reported by Kim et al. (2013)

Specimen	00T6	10T4	20T4	10T2	0'T6
thickness lower portion of web (in)	15/64	10/64	10/64	5/64	15/64
height of lower portion of web (in)	0	4	8	4	0
uncorroded volume ratio	1.00	0.96	0.92	0.92	1.00
shear buckling strength (kips)	289.2	286.8	259.1	266.7	228.7
predicted shear buckling strength (Eq. 1-1) (kips)	151				

The results presented by Kim et al. illustrate the relatively conservative nature of shear buckling provisions in the absence of local effects such as web crippling. The relatively small amount of uniform and controlled ‘damage’ in these specimens resulted in quite uniform behavior that may not be representative of the kind of variability likely in the field. The results reported by Kim et al. were subsequently used by Ahn et al. (2013) in their development of Equation 1-6.

1.5 Computational Study of Bearing Regions Exhibiting Beam End Corrosion

Several studies have reported finite element (FE) simulations of beam end corrosion behavior; these are summarized in Table 5. All studies report quasi-static nonlinear analyses. All but Gerasimidis and Brena (2019) focus on web buckling and generally provide model details that will mitigate local bearing effects. With a focus on web buckling behavior, bilinear (including elastic-plastic) material properties are likely adequate as used in most studies. To accurately capture buckling effects, the effects of residual stress should also be modeled although this is only done in half of the available studies.

Table 5 Summary of Analytical Studies of Beam End Corrosion

citation	Liu et al. (2011)	Ahn et al. (2013)	Yamaguchi et al. (2014)	Khurram et al. (2014)	Bao et al. (2018)	Gerasimidis and Brena (2019)
behavior considered	web buckling of beam in flexure	web buckling of beam in flexure	web buckling of beam in flexure	web buckling of vertical stub test	web buckling of vertical stub test	web yield and crippling of beam in flexure
instability analysis	distortion	eigenvalue	eigenvalue	eigenvalue	not reported	distortion
FE program	DIANA 9.3	MARC 2010	ABAQUS	ABAQUS	ABAQUS	ABAQUS
element type	8-node shell (CQ40S)	4-node shell	4-node shell	coupled shell-solid element	not reported	4-node shell (SR4)
mesh size in critical area	2.0 in.	0.40 in.	not reported	0.1 in.	3.0 in.	0.50 in.
corrosion simulation	element thickness reduction	element thickness reduction	element thickness reduction	element thickness reduction	element thickness reduction	element thickness reduction
hole simulation	no holes	no holes	no holes	no holes	elements removed	elements removed
material	elastic- plastic	elastic- plastic	bilinear (0.01E post yield stiffness)	measured nonlinear	bilinear [inferred from text]	measured nonlinear
residual stress	yes	no	yes	yes	no	no
validated	single uncited prototype	Kim et al. (2013)	no	Khurram et al. (2014)	1:10 scale vertical stub test	Gerasimidis and Brena (2019)
parameters considered in parametric study	corrosion pattern and thickness	corrosion thickness, corrosion volume, and bearing support condition	corrosion pattern and thickness	corrosion height and thickness stiffener damage	hole size area loss	corrosion topology, beam geometry, material properties, boundary conditions, and web distortion

Most studies shown take a similar approach of using shell elements with reduced thickness to model corrosion damage and removing elements entirely to simulate holes. Khurram et al. (2014) report using a coupled shell-solid element utilizing multi-point constraints to reduce the integration. This is thought to be necessary due to the small mesh size used (0.1 in.) which is only a fraction of the 0.5 in. web thickness. Curiously, only Gerasimidis and Brena (2019) report having conducted a convergence study to determine mesh size.

To date, no analytic study has addressed the complete behavior of a corroded beam end. Most studies have focused on web buckling neglecting local effects. As described below, Gerasimidis and Brena (2019) focused on local effects, neglecting buckling. Khurram et al. (2014) and Bao et al. (2018) base their models and experimental validation using vertical stub tests. These are short sections of beams tested in vertical compression. While such tests may be conducted rapidly and can theoretically capture all behaviors of interest depending on support conditions provided, they do not simulate realistic *in situ* boundary conditions of beam ends.

The results of the studies reported in Table 5 are all quite similar: shear capacity is reduced in the presence of corrosion. In general, the results presented are limited by chosen specimen geometry and extrapolation to other geometries is inappropriate. The results generally confirm well-established shear buckling behavior as described by Equations 1-1 to 1-5.

1.5.1 MassDOT Report 19-008

In their extensive study, Gerasimidis and Brena (2019) validate a high-fidelity FE model of their test specimens (reported in Table 3), providing an excellent basis for modelling beam end corrosion; some critical aspects of their modeling campaign are summarized here.

Gerasimidis and Brena implemented a quasi-static analysis using ABAQUS, a general-purpose FE program that engages the nonlinear analysis routines necessary for failure and instability analysis of the corroded beam ends. The beam end models were implemented using general purpose shell elements (element designation: S4R) having specifically assigned thickness based on detailed corrosion mapping of the test specimens (Figures 3a and 3b). In subsequent parametric analyses, reduced element thickness was assigned uniformly in deteriorated regions. Holes were simulated by removing elements.

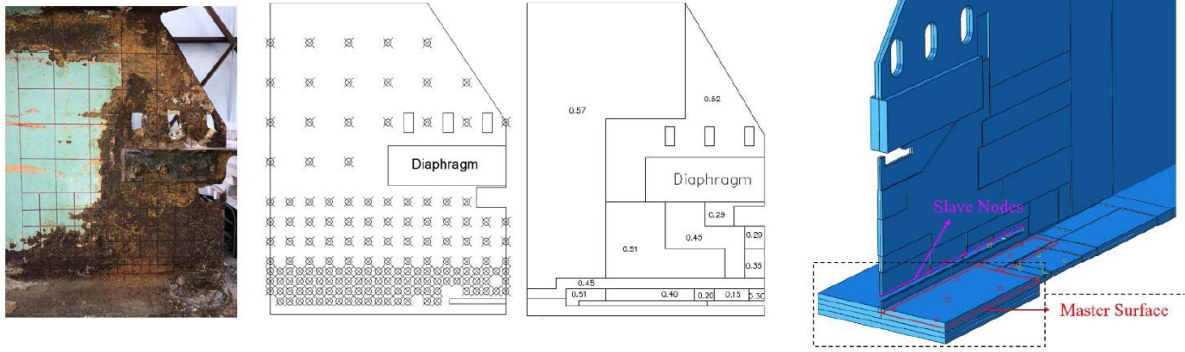
A mesh convergence study led to using 2 in. elements over the span of the beam and a denser 0.5 in. mesh at the corroded beam end. The denser mesh was extended 5 in. beyond the modeled corrosion. The mesh and transition can be seen in Figure 3d.

Interaction between the bottom flange and bearing (Figure 3c) was modeled using ‘softened contact’ in the normal direction in which contact interaction is defined using a linear contact pressure-overclosure relationship. This was calibrated to experimental results which were found to have a stiffness of approximately 20 kips/in. In the transverse directions, a frictional interaction was applied. Following calibration with experimental results, a coefficient of friction of 0.74 was selected. The sensitivity of model results to this parameter is reported to be negligible.

When holes were modeled at the flange-web interface, ‘hard contact’ interaction in the normal direction was implemented, eliminating the penetration of web slave nodes into flange master nodes (Figure 3d) and permitting the holes to “close” and transmit load. Finally, the use of shell elements permits plate distortions to be modelled (Figure 3e).

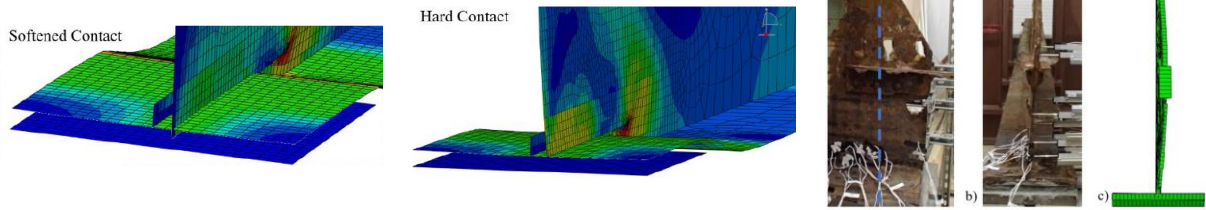
Gerasimidis and Brena report an extensive parametric study of over 2000 cases which were used to calibrate Equations 1-10 to 1-11. Parameters considered in the study include a) beam type;

b) material; c) presence or absence of stiffener; d) beam length; e) boundary condition (bearing type); f) corrosion topology (Table 1); g) presence of holes; and h) initial distortion magnitude.



a) corrosion mapping (note horizontal hole at web-flange interface at end of girder)

b) FE model



c) softened contact of flange to bearing (note resulting variation of flange stress)

d) hard contact following hole closure

e) initial distortion of web

Figure 3 Details of FE Model of Specimen 1 Reported by Gerasimidis and Brena (2019)

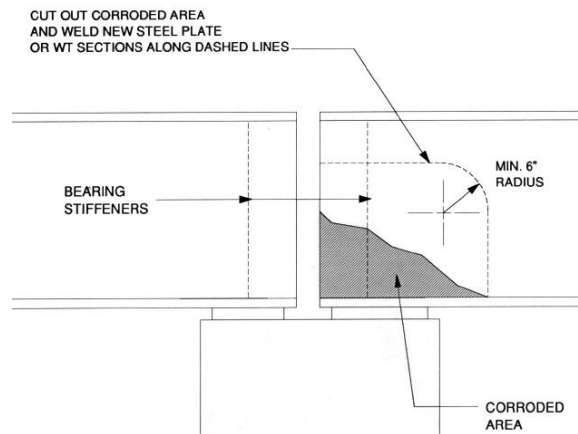
The extensive modeling efforts of Gerasimidis and Brena informed the models developed as part of the present study reported in Chapter 6.

1.6 Conventional Structural Repair of Beam End Corrosion Damage

For the purposes of this discussion, ‘structural repair’ is load bearing and is provided to stabilize, restore or improve the capacity of the beam end region. The repair measures may resist some of the load, relying on residual capacity of the existing beam end, or the repair measures may entirely replace the load carrying capacity of the beam end. Repairs can also be envisioned that do not augment the strength of the beam end, but enhance only its stability, permitting greater loads to be carried.

The current state of practice for structural repair of beam ends is the complete replacement of the affected region as shown schematically in Figure 4. This approach requires the girder to be temporarily supported (‘jacked’) away from the beam end. This will often require modification of the beam (addition of bearing stiffener(s) at the jacking location, for instance) to accept the jacking loads in addition to erection of temporary supports. The damaged beam end region is cut out and a new section (often a WT in order to replace the bottom flange without the need for additional fabrication) is installed with full penetration groove welds all around (Figure 4a). Figure 4b shows an example of a bolted installation in which the web and flange splices can be seen. A variation of this approach may see only the web replaced with a new plate. The new section is finally sand-blasted and painted. Clearly this operation requires the bridge to be closed to traffic and will impact carriageways under the bridge.

In some cases of relatively minor or localized damage to the web, other viable steel-based repairs may include the addition of web doubler plates (patches), web-flange stiffening, or replacing or providing new/additional bearing stiffeners (Figure 5b). These methods require field welding or bolting (Figure 5) but can often be accomplished with only lane closures on the bridge.

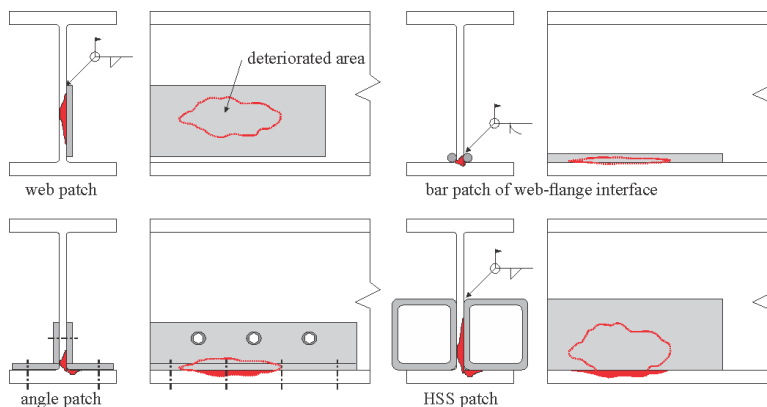


a) schematic representation (PennDOT 2010)



b) bolted beam end replacement
(Wakabayashi et al. 2013)

Figure 4 Steel Beam End Repair – Replacing Deteriorated Region



a) schematic examples of patch repairs



b) bolted repair of web-flange
region and bearing stiffener
(Wakabayashi et al. 2013)

Figure 5 Steel Patch Repairs of Deteriorated Beam End Regions

Addition of corbels and new bearings ‘inboard’ of existing deteriorated beam ends may also be feasible in some cases – most typically at interior pier locations where ‘balanced corbels’ can be post-tensioned to cap beams. This method is similar that used to enhance the length of bearing regions to accommodate seismic movement (Wakabayashi et al. 2013). Such an approach may also be feasible for simple span bridges having their bearings embedded in concrete diaphragms.

The focus of this study, however, is the investigation of alternate methods of beam end strengthening. These methods may leverage high-performance materials and the intent is that they may be implemented without the need to provide temporary support for the bridge and preferably that they may be installed without closing the bridge to traffic.

1.6.1 Temporary Support During Repair

The objective of not requiring temporary support has an inherent implication that the existing structure is adequate to resist whatever loads are present during the repair (and subsequent curing, if applicable) procedure. Without pre-loading, prestressing or post-tensioning of some kind, any repair scheme is only able to resist loads applied after its installation. Repairs that are called upon to resist any portion of the bridge self-weight, for instance, must have this load relieved during installation.

Preloading during repair installation may be effectively used on continuous structures but is not an available option for simple spans. While some potentially applicable prestressed technology has been proposed, none has been demonstrated at full scale and none in any application like the repair of deteriorated beam ends.

1.7 Partial Encasement of Damaged Beam Ends in High Performance Concrete

Considerable interest has recently been developed in the use of ultra-high-performance concrete (UHPC) as a means of steel beam end repair. Reported in McMullen and Zaghi (2020), and Zmerta et al. (2017), this work has been conducted primarily at the University of Connecticut

and is represented by the doctoral theses of Zmerta (2015), Kruszewski (2018), and McMullen (2019).

1.7.1 Ultra High-Performance Concrete

Ultra high-performance concrete (UHPC) is a “cementitious composite material composed of an optimized gradation of granular constituents, a water-to-cementitious materials ratio less than 0.25, and a high percentage of discontinuous internal fiber reinforcement” (Graybeal 2014). Today, a variety of UHPC products are available on the market, most provided as premixed ‘powders’ to which fibers, water and liquid admixtures are added. The preblended mixes typically contain a proprietary blend of cement ($\approx 30\text{-}40\%$ by weight), silica sand ($\approx 35\text{-}40\%$), silica fume ($\approx 10\text{-}15\%$) and ground quartz ($\approx 10\%$) having a relative uniform grading between 0.1 and $1000\text{ }\mu\text{m}$ (Graybeal 2014). To obtain such grading, components are often ground finer than for other applications resulting in components being referred to as silica ‘flour’ or nanosilica. UHPC contains no coarse aggregate and will not intentionally include particle sizes exceeding $2000\text{ }\mu\text{m}$ (Graybeal 2014).

UHPC exhibits compressive strength greater than 21.7 ksi (150 MPa) and sustained postcracking tensile strength greater than 0.72 ksi (5 MPa). UHPC has a discontinuous pore structure that reduces liquid ingress, enhancing durability compared to conventional and high-performance concretes (Graybeal 2014). Table 6 contrasts typical material properties of UHPC with those of high strength concrete (HSC) and conventional normal strength concrete (NSC). In terms of mechanical behavior, although considerably stronger, UHPC does not differ considerably from conventional concrete. Due to the lack of large aggregate, UHPC has a proportionally lower modulus when estimated using compression strength. Although initial tensile strength is also

similar, UHPC, due to the inclusion of a high volume of fibers, exhibits significant post cracking tensile strength.

Table 6 Typical Properties of UHPC, HPC, and NSC (equations express f_c' in ksi units)

	UHPC	high strength concrete (HSC)	conventional concrete (NSC)
primary citation	Russell and Graybeal (2013)	ACI 363R-10 & Burg and Ost (1994)	AASHTO LRFD
density, ρ_c	150 to 156 pcf	150 to 156 pcf	≈ 145 pcf
compressive strength, f_c'	20 to 30 ksi	10 to 17 ksi	4 to 8 ksi
tensile cracking strength, f_t	0.9 to 1.5 ksi	0.7 to 1.0 ksi	0.4 to 0.7 ksi
direct tensile strength, f_t	$f_{ct} \approx 0.25(f_c')^{0.5}$	$f_{ct} \approx 0.24(f_c')^{0.5}$	$f_{ct} \approx 0.23(f_c')^{0.5}$
modulus of rupture, f_r	$f_r \approx 0.25(f_c')^{0.5}$ [no fibers] $f_r \approx 0.44(f_c')^{0.5}$ [with fibers]	$f_r \approx 0.24$ to $0.37(f_c')^{0.5}$	$f_r \approx 0.23(f_c')^{0.5}$
elastic modulus, E_c	6000 to 10,000 ksi	7200 to 8200 ksi	3600 to 5200 ksi
elastic modulus estimate	$E_c = 1460(f_c')^{0.5}$	$E_c = 1260(f_c')^{0.5} + 1000$ ≈ 1500 to $1570(f_c')^{0.5}$	$E_c = 1820(f_c')^{0.5}$
Poisson's ratio	0.20	0.20	0.20
CTE	5.5 to $8.5 \times 10^{-6}/^{\circ}\text{F}$	5 to $7 \times 10^{-6}/^{\circ}\text{F}$	$\approx 6 \times 10^{-6}/^{\circ}\text{F}$
specific creep	0.04 to $0.3 \times 10^{-6}/\text{psi}$	0.2 to $0.4 \times 10^{-6}/\text{psi}$	0.1 to $1.0 \times 10^{-6}/\text{psi}$
total shrinkage	up to $900 \mu\epsilon \times 10^{-6}$	up to $750 \mu\epsilon \times 10^{-6}$	up to $800 \mu\epsilon \times 10^{-6}$

Durability of UHPC is typically quantified as being very good to excellent. Haber et al. (2018) reports tests of six UHPC mixes. All exhibit “very low” (<1000 Coulombs passing) chloride permeability and “very low” ($>37 \text{ k}\Omega\text{cm}$) surface resistivity. Both results indicating impermeable mixes that will be resistant to corrosion of internal reinforcement. Haber also reports negligible

mass loss and change in relative dynamic modulus following 600 freeze-thaw cycles, once again indicative of very durable mixes.

Russell and Graybeal (2013) summarize the four primary characteristics that distinguish UHPC from conventional concrete as: a) higher compressive strength; b) higher tensile strength with ductility; c) increased durability; and d) higher initial unit cost. Early studies of UHPC focused on utilizing its high compression strength and improved tensile behavior to optimize material use for superstructure elements. More recently, UHPC is recognized as a material suited to durability-driven applications including repair. UHPC is increasingly specified for field-cast closure pours or as grout material in prefabricated superstructure elements (often those used in accelerated bridge construction (ABC) projects) (Graybeal 2014). UHPC is also being investigated for a variety of other applications including precast concrete piles, seismic retrofit of substandard bridge substructures, thin-bonded overlays on deteriorated bridge decks, and security and blast mitigation applications (FHWA 2019).

1.7.2 Implementation of UHPC

Bridge owners perceive one of the primary advantages of UHPC to be its long-term durability, presumably resulting in structures with a longer service life and reduced life-cycle costs compared with structures built with conventional concrete (Russell and Graybeal 2013). However, Russell and Graybeal point out that “no studies were identified to show that this is the case.” They go on to suggest that UHPC may not prove to be cost-effective for large superstructure elements due to its remarkably high differential cost.

Russell and Graybeal identify scenarios in which UHPC can be used to address performance issues without a major cost impact. They cite the use of UHPC as cast-in-place

connections between prefabricated elements, likely the most common use of UHPC today. In this application, the incremental cost of using UHPC is small while the improved performance (eliminating cracking and leaking that occurs when conventional concretes or grouts are used) is significant. UHPC is also potentially beneficial for producing simplified connection details having shorter reinforcement splice lengths and fewer conflict points (Russell and Graybeal 2013).

Today, few producers or contractors have experience with UHPC. In general, UHPC requires specialized mixing equipment or longer mixing times in conventional concrete mixers, longer set times, and more rigorous curing regimes. Quality control methods and tolerances are significantly different. For example, the use of small-size cylinders for measurement of compressive strength is required in order that tests may be conducted using available machines.

1.7.3 University of Connecticut Study

As part of a multi-phase project, the University of Connecticut investigated the use of UHPC as a repair method to recover beam end bearing capacity, which was reduced due to steel section loss induced by corrosion. The repair takes the form of a cast-in-place UHPC panel connected to the girder using headed shear studs welded to the undamaged steel portions of the girder web.

1.7.3.1 Zmerta (2015)

Zmerta (2015; summarized in Zmerta et al. 2017)), as a proof-of-concept, reports tests of three W21x55 girders. The girders were tested over a span of 12 feet with the load placed 32 in. from the test end (resulting $a/d = 1.5$) in order to simulate the shear critical condition for the girder (Figure 6a). Although additional stiffeners were provided for the test, the “studied end”, shown in

Figure 6a, remained unstiffened. The compression flange was braced laterally along the longer shear span to prevent lateral buckling. The nominal bearing capacity of a W21x55 loaded in the manner tested is 123 kips, governed by web crippling (the length of the bearing was reported to be $N = 5.625$ in.) as indicated in Table 7. Despite the short span, flexural capacity ($525 \text{ kip-ft} = 197 \text{ kip bearing capacity for geometry tested}$) of the section controls the response and crippling can be mitigated using a bearing stiffener, for instance.

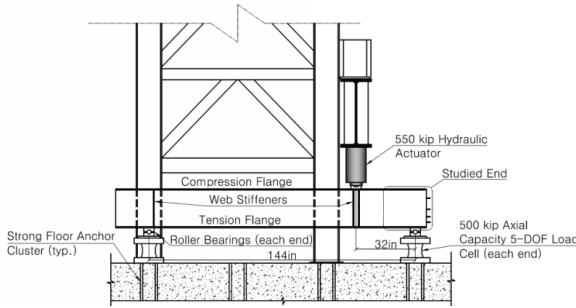
An undamaged control specimen and two specimens having artificial corrosion damage (Figures 6b and c), produced by thinning the web using a milling machine, were tested. The rectangular damaged region extended 19 in. along the girder and extended 3.75 in. up the web (i.e., Pattern W1 with $C_L = 19$ in. and $C_H = 3.75$ in.). A portion of the flange was also damaged as seen in Figures 6b and c. The resulting plate thickness of each damaged girder is given in Table 7. The nominal residual capacity of this damaged girder based on web crippling capacity is only 18.4 kips (the other capacities will not fall as dramatically). A quirk of this study is that to produce the damage, a tee-section was cut from the original girder, the damaged simulated on this, and then the tee was replaced into the girder using full-penetration groove welds. The cutline is shown in Figure 6b and only the tee is shown in the left image in Figure 7b. A second concern that must be noted is that the reported measured flange and web dimensions of the undamaged W21x55 girders were well out of expected rolling tolerance.

The undamaged girder behaved largely as expected, exhibiting a web crippling failure (Figure 6d) at an applied bearing load of 180 kips, demonstrating considerable reserve capacity. The damaged girder exhibited a web crippling failure at an applied bearing load of 43.4 kips. This failure is characterized by a 'kink in the web at the top of the damaged region (i.e, at the change in section) as seen in Figure 6e. The damaged girder exhibited considerably greater residual

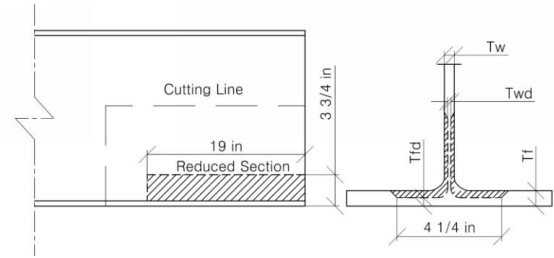
capacity than predicted although it only achieved about 35% of its nominal capacity exhibiting about 66% web material loss.

Table 7 Girder geometry and test results reported by Zmerta (2015) [capacities calculated by author]

girder	plate thickness (in.) (% remaining)				bearing capacity (kips)	limit state
	undamaged flange	damaged flange	undamaged web	damaged web		
W21x55 nominal capacity	0.522	n.a.	0.375	n.a.	226 123 260 197	web shear (Eq. 1-1) web crippling (Eq. 1-8 and 1-9) web bearing (Eq. 1-7) flexure: $M_n = ZF_y$
undamaged	0.558	n.a.	0.339	n.a.	180	web buckling
damaged	0.558	0.325 (58%)	0.335	0.113 (34%)	43.4	web crippling
repaired	0.504	0.271 (54%)	0.383	0.102 (27%)	35 69 176	first crack of UHPC shear crack in UHPC flange flexure



a) test set up



b) simulated damage



c) simulated damage



d) crippling of undamaged web



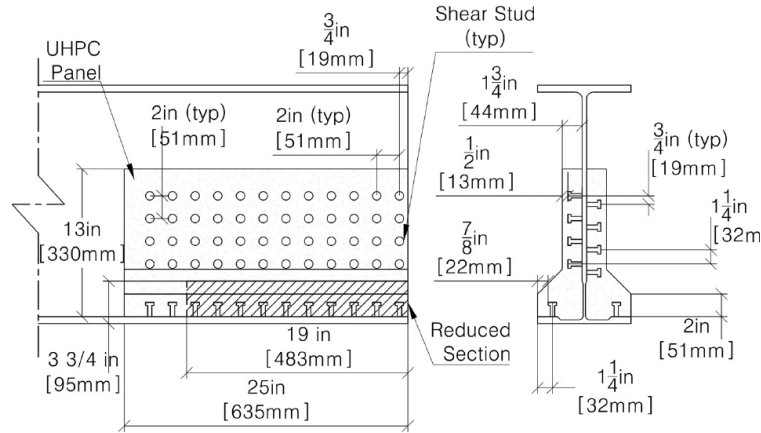
e) crippling of damaged web

Figure 6 Test Set-up and Damaged Girders Reported by Zmerta (2015)

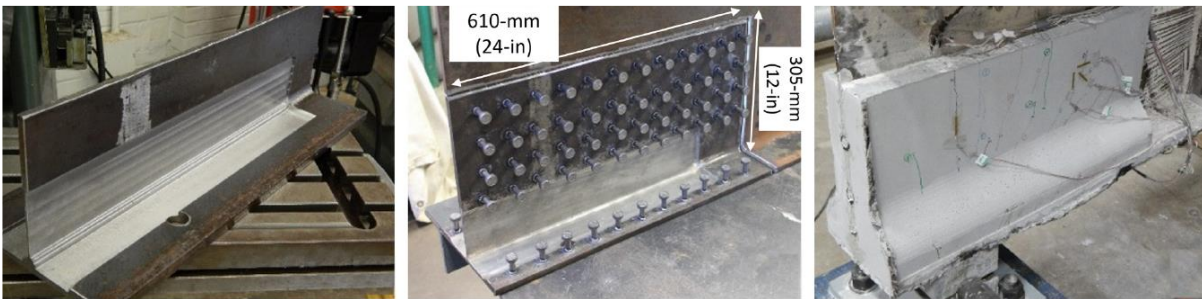
The second damaged specimen was repaired using UHPC as shown in Figure 7. The repair, shown in Figure 7, consisted of 1.75 in. thick cast-in-place UHPC panels on both sides of the web extending 25 in. along the beam and 13 in. (about two-thirds) up the web. Forty-eight 3/8 in. diameter by 1.25 in. long headed shear studs were applied to both sides of the undamaged region of the girder web (96 studs in all). Twelve additional studs were applied to each bottom flange outstand (24 in all). All studs were applied on a 2 in. pattern as shown in Figure 7a. The stud patterns were offset 1 in. on either side of the web (Figure 7a). ‘Bulb-shaped’ UHPC panels were installed as shown in Figure 7b; the single-use forms were reportedly milled from 2 in. foam insulation boards.

Commercially available Ductal[®] UHPC was used. This UHPC mix is reportedly capable of achieving 12 ksi compressive strength in 12 hours if cured at 120°F and 90% relative humidity. The strength evolution of the UHPC reported by Zmerta was only 4 ksi at 12 hours but 16 ksi at the time of girder testing (96 hours).

As reported in Table 7, The UHPC-repaired girder exhibited the first cracks in the UHPC at a bearing load of 35 kips. Shear cracks appeared at 69 kips and the girder exhibited evidence of web yielding (circled regions in Figures 7c and d) at an applied bearing load of 176 kips when the test was stopped. The observed cracking of the UHPC was relatively well distributed and minor (Figures 7c and d). The inclination of the cracks suggests a compressive strut developed in the UHPC resisting the bearing force. The UHPC prevented the web from buckling and/or crippling.



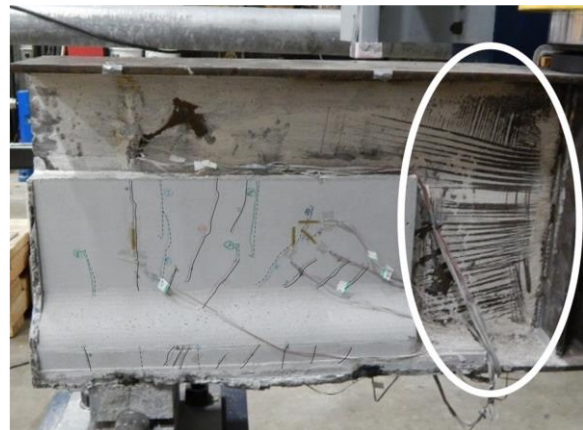
a) headed stud and UHPC layout



b) progression or repair (note that left image shows only damaged tee region prior to being rewelded into girder)



c) cracking of near side of UHPC panel
(end of girder at right)

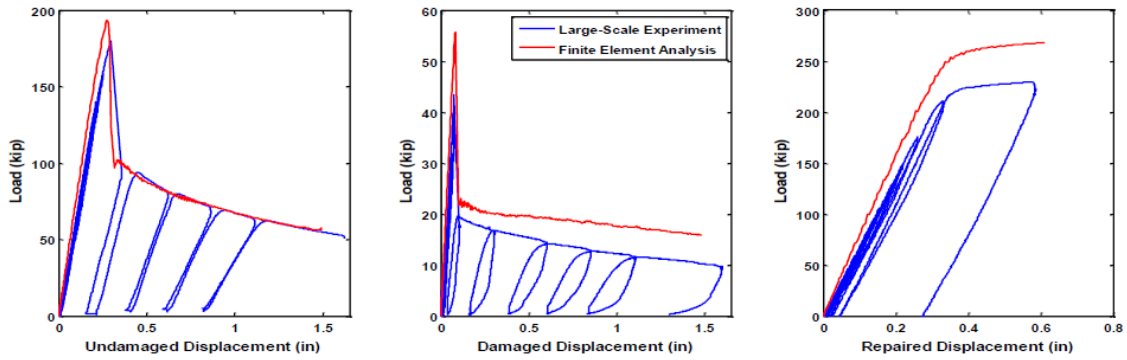


d) cracking of far side of UHPC panel
(end of girder at left)

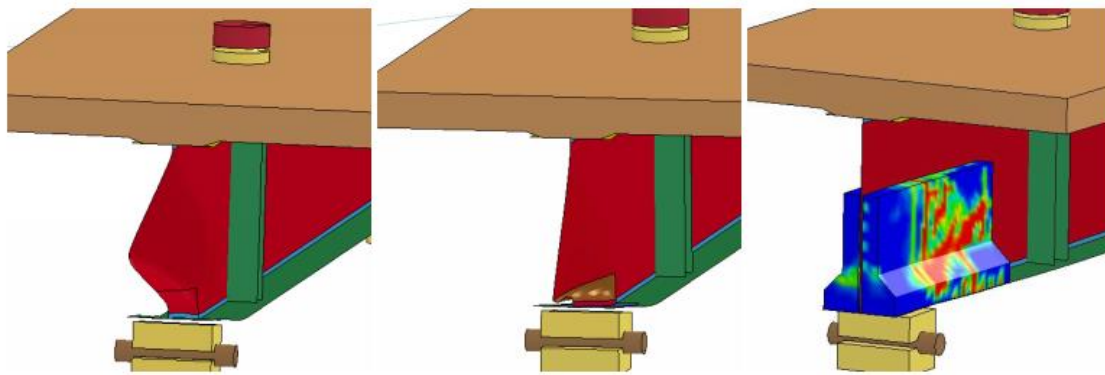
Figure 7 UHPC Repaired Girder Reported by Zmerta et al. (2017)

Zmerta (2015) also reports an analytical study. Finite element (FE) simulations of the test girders were developed using LS-Dyna. Four-node shell elements were used to model the steel

girders, solid elements to model the UHPC and beam elements were used to model the studs. The models were validated using the experimental results (Figure 8) prior to being extended to investigate other girder repair geometries. Figure 8b shows the test girder models with a composite concrete deck added. The addition of the deck has little effect on girder predictions since behavior was driven by web crippling in each case.



a) FE-predicted (red) and experimental (blue) bearing load versus displacement curves



b) FE-predicted failure modes in presence of composite deck

Figure 8 FE Models of Test Girders Reported by Zmerta (2015)

The computational program was extended to consider different girder geometries as summarized in Table 8. W36x160 rolled sections were considered with and without the presence of 0.5 in. bearing stiffeners. Additionally, a 54 in. deep plate girder having a 3/8 in. web was considered. The 54 in. plate girder had 1 in. bearing stiffeners and 5/16 in. ‘first interior stiffeners. Each prototype was subject to corrosion damaged in a W2 pattern (Table 1). Web and bearing stiffener thickness was reduced 75% and flange thickness was reduced 48% (W36 girder) and 38%

(plate girder). Based on the FE modeling, the residual girder capacities varied from 33% to 8% of the nominal section flexure capacity (Table 8).

Three variations of UHPC encasement repairs were modeled: full web height; partial web height and L-shaped; these are shown in Table 8. Each was predicted to fully restore the undamaged bearing capacity of the prototype. The W36 beams were restored to being flexure critical. Because the UHPC should constrain web instability, the tension field behavior of the 54 in. plate girder was enhanced by the presence of the UHPC.

The simulated UHPC encasement repairs contained fewer studs anchored to the web than the experiments (compare Figure 7a to those in Table 8). The models appear to suggest that anchoring the UHPC between the flanges (full height) is equally, if not more, efficient as providing a relatively dense array of studs on the web. The L-shaped (matching the damage pattern) repair was also adequate for the rolled shape that is flexure-critical without damage.

Table 8 FE Models of UHPC Repaired Girder End Regions (after Zmerta 2015)

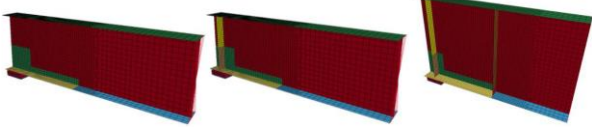
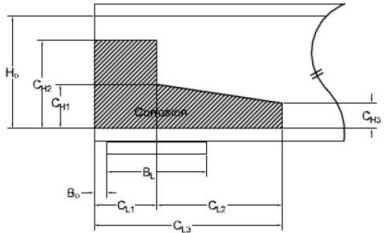
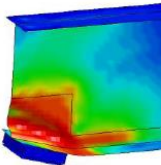
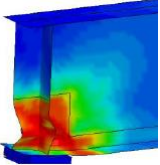
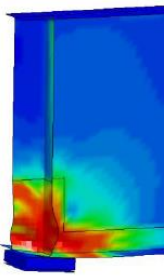
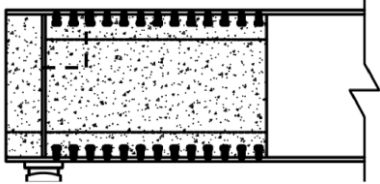
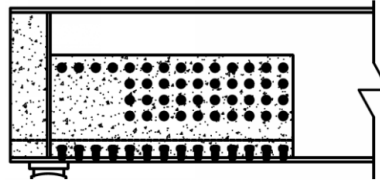
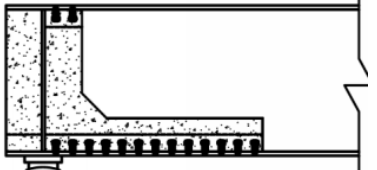
girder	W36x160	W36x160	54 in. plate	
bearing stiffener	none	0.5 in.	1.0 in.	
				
nominal capacity (kips)	234	243	475	
nominal limit state	flexure	flexure	tension field	
damage pattern (in)	W2 $C_{L1} = 16.25$ $C_{L3} = 51.25$ $C_{H2} = 14.57$ $C_{H1} = C_{H3} = 3.65$		W2 $C_{L1} = 12.53$ $C_{L3} = 51.50$ $C_{H2} = 17.18$ $C_{H1} = C_{H3} = 4.90$	
damaged capacity (kips)	18	80	98	
damaged limit state	web crippling	web/stiffener crippling	web/stiffener crippling	
				
full height repair capacity (kips)	277	278	649	
full height repair limit state	flexure	flexure	tension field	
partial height repair capacity (kips)	274	272	504	
partial height repair limit state	flexure	flexure	tension field; UHPC compression	
L-shaped repair capacity (kips)	271	269	not modeled	

Table 8 (continued)

L-shaped repair limit state	flexure	flexure		
-----------------------------	---------	---------	--	---

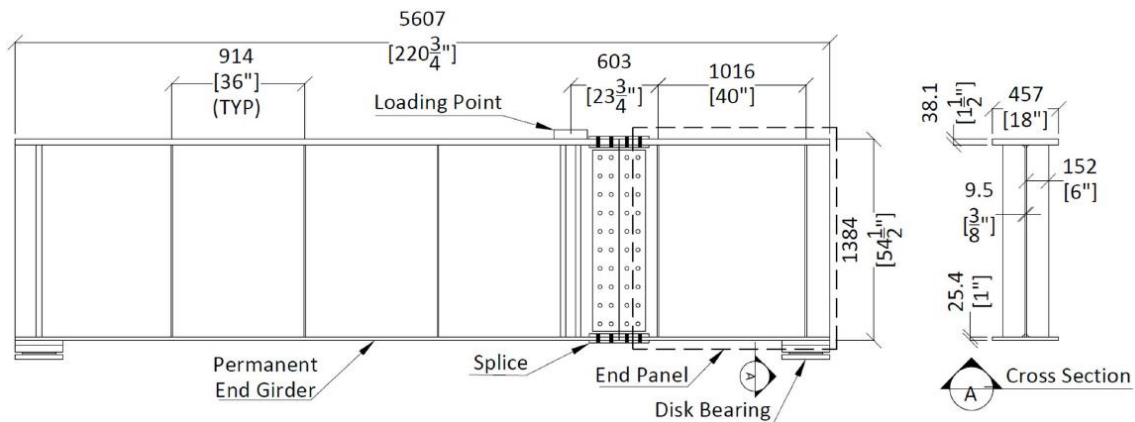
1.7.3.2 McMullen (2019)

McMullen (2019; summarized in McMullen and Zaghi 2020) extended Zmerta's proof of concept to full-scale tests having more realistic simulated corrosion damage. McMullen ultimately proposed design and construction recommendations as described below.

McMullen tested four (one control and three repaired) 54 in. deep plate girder sections loaded in three-point flexure such that the shear span was 64 in. ($a/d = 1.18$). The damaged end panel was spliced to a longer test beam which was reused in each test (Figure 9). In the test configuration used, the nominal bearing capacity of the end region is 212 kips, representing tension field failure. Due to the presence of a bearing stiffener, crippling and bearing limit states are significantly higher. Based on the bearing stiffener geometry, the nominal bearing capacity of the girder is 495 kips.

Corrosion was simulated by a combination of grinding and sandblasting resulting in the localized damage shown in Figure 9b. Simulated damage was targeted at 66% of web and stiffener plate loss and 50% of flange plate loss concentrated in a region at the end of the girder. The damage pattern was W1 with $C_L = 8$ in. and $C_H = 5$ in. As seen in Figure 9b, small regions of 100% section loss were simulated immediately above the bearing (Pattern M1: $a \approx 2$ in.; $b \approx 4$ in.). The bearing capacity of the damaged girder was 95.3 kips (Table 9) controlled by crippling of the reduced web and stiffener as seen in Figure 9c. Another important observation made by McMullen is that the failure of the specimen having more realistic, non-uniform damage exhibited more gradual

reduction of stiffness than observed for the very uniform artificial damage reported by Zmerta (2015) and Kim et al. (2013).



a) test arrangement showing test panel at right of slice and reused girder element to left



b) specimen with damaged end region



c) end region of damaged specimen following testing showing crippling of web and stiffeners

Figure 9 Test Set Up and Damage Reported by McMullen and Zaghi (2020)

UHPC encasement, shown in Figure 10, was limited to a ‘stub column’ immediately above the bearing, encasing the bearing stiffener region only. Two repairs extended the full height of the 52 in. web while the third extended half-height: 26 in. Two commercially available UHPC mixes having strengths exceeding 20 ksi were used (see Table 10). Ductal® JS1212 is a high early-strength mix (intended to achieve 12 ksi in 12 hours) whereas JS1000 has a higher ultimate strength but a retarded initial set (intended to achieve 14 ksi in 96 hours). During UHPC placement and the

initial 6 hours of cure of full height specimen 2, field-derived vibrations were applied to simulate traffic loads. The vibrations applied using a shaker on top of the specimen (located on top of the white box shown in Figure 10a). This in no way duplicates the cyclic strains associated with actual traffic loads. No deleterious effect of these vibrations, having maximum acceleration of 0.002g, were observed.

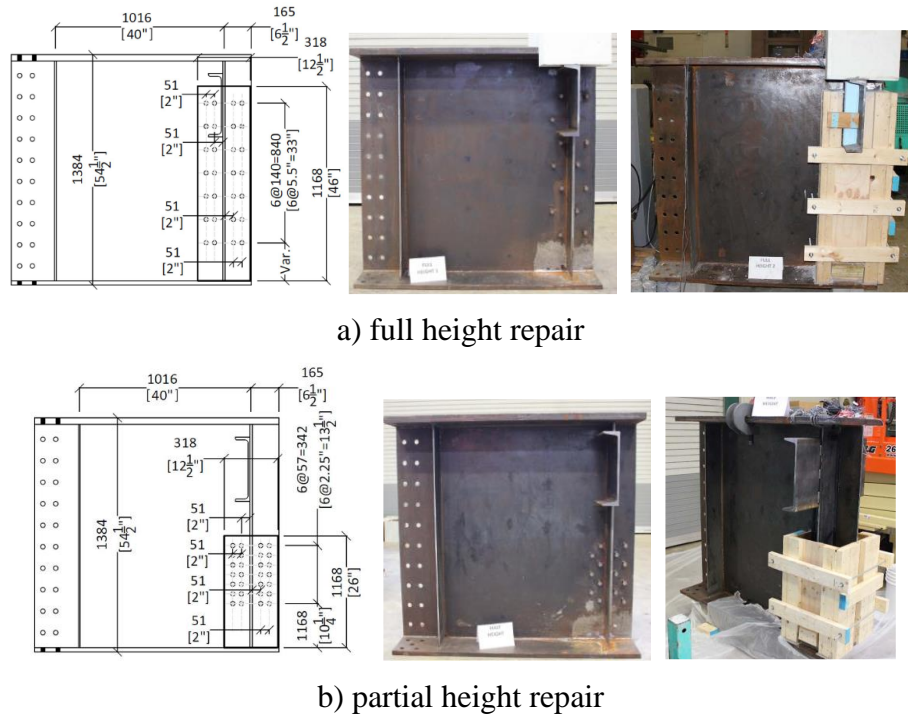


Figure 10 UHPC Repairs Reported by McMullen and Zaghi (2020)

Test results of the UHPC repaired girders are provided in Table 9. Both full-height repairs behaved similarly, achieving the nominal capacity of the undamaged girder (495 kip bearing capacity) and exhibiting a tension field buckling failure in the web panel immediate adjacent the repair. The failures are shown in Figure 11. The partial height repair exhibited some tension field behavior but ultimately, the web crippled immediately at the top of the UHPC (Figure 11c). Because tension field behavior was engaged, all repaired girders exhibited post-peak residual capacity exceeding 85% through displacements exceeding twice those at the ultimate capacity.

Table 9 Test Results Reported by McMullen (2019)

	damaged girder	full height repair 1	full height repair 2	partial height repair
UHPC	n.a.	JS1000	JS1212	JS1212
strength at 24h (ksi)		^a	≈ 8	≈ 8
strength at 48h (ksi)		≈ 11	≈ 16	≈ 16
strength at test (ksi)		29.3	25.3	23.3
bearing capacity (kips)	95.3	527	497	472
limit state	web/stiffener crippling	web buckling (tension field)	web buckling (tension field)	web crippling immediately above UHPC
residual capacity		85%	90%	85%
^a Ductal® JS1000 is a retarded set product not expected to have significant strength at 24h				

**Figure 11 Failure Modes of UHPC Encased Girders Reported by McMullen and Zaghi (2020)**

Like Zmerta (2015), McMullen (2019) presented finite element (FE) modeling based on the experimental results. The FE simulation modeled uniform section loss, rather than actual damage. The degree of uniform section loss simulated in the FE model was adjusted to calibrate the model with experimental results. The web, which had about 66% section loss and a small region of 100% loss was modelled as having 80% uniform loss. The stiffener, also having 66% section loss was modeled as having 60% section loss. Modeled flange section loss was not reported although considering the shear-critical behavior of the girder, the model is not likely sensitive to this. Once calibrated, unsurprisingly, the model replicated the experimental data well.

McMullen (2019) provided recommendations for such UHPC encasement repairs as follows:

1. Headed stud capacity in UHPC may be conservatively estimated using conventional stud capacity calculation. Given the high concrete strength, stud capacity will govern. This recommendation is limited to the use of 0.5 in. studs as investigated.
2. Studs should only be welded to undamaged portions of the girder. The recommended surface preparation is “power tool clean and free of loss material” (i.e., SSPC SP3). Studs placed on opposite sides of the web should be staggered.
3. Stud spacing, clear cover, edge distance, and distance to the deteriorated area should be four stud diameters ($4d_b$).
4. UHPC should have a 28-day strength exceeding 18 ksi.
5. Full-height encasement is preferable although half-height encasement is acceptable to improve constructability (place UHPC from below the deck, rather than through holes drilled through the deck).
6. Watertight forms are required for UHPC placement and forms should have a non-absorbing (hydrophobic) surface in contact with the UHPC.
7. UHPC may be placed with the bridge in operation (vibration is acceptable).
8. The capacity of the UHPC encased girder bearing may be taken as the nominal capacity of the repaired girder. Any increase in original capacity should be assessed on a case-by-case basis.

In summary, the University of Connecticut study of UHPC encased beam ends illustrates the efficacy of this method of repair but provides no comparison to alternatives. The guidance provided by McMullen reflects the experimental work conducted but is otherwise unsupported.

The suggestion that UHPC may be allowed to cure with the bridge in operation is unsupported by the experiments conducted.

1.7.4 Field Applications of UHPC Repair

Hain and Zaghi (2021) report a field implementation repairing 45 beam ends on a bridge carrying I-91 over a rail corridor in New Haven Connecticut. The UHPC repair method was reportedly selected due to the complexity of the site and logistics (Figure 12a): the skewed bridge had variable beam sizes and bearing and stiffener details. Additionally, the piers provided little lateral clearance to both electrified Amtrak and freight rail lines. UHPC was placed from above the deck through cored holes connected to a PVC-pipe distribution system below the deck (Figure 12b) and the girder end region was heated to promote curing (enclosure seen in Figure 12a). A view of the final repair is seen in Figure 12c.

Initial data reported at two months after placement indicated that the web shear in the end region was being shared with the UHPC in a ratio of about 2:1 (steel strain to UHPC strain). After four days and through at least 28 days, the incidence of low-probability, high-strain events was also reduced by the presence of the UHPC.



a) I-91 bridge over rail corridor b) PVC distribution of UHPC c) completed repair
Figure 12 Field Implementation of UHPC Repair Reported by Hain and Zaghi (2021)

Texas DOT (TxDOT 2021) reports a similar repair on the Sidney Sherman Bridge serving the Port of Houston (Figure 13a). A UHPC encasement was selected to provide a 20-year life

extension and to minimize unacceptable cost of traffic closures that may otherwise be required.

Figure 13b shows the UHPC encasement of a transverse steel diaphragm.



a) Sidney Sherman Bridge



b) completed repair of diaphragm

Figure 13 Field Implementation of UHPC Reported by TxDOT (2021)

FHWA (2021) reports other field implementations as follows:

- I-95 in Jacksonville, Florida (2017)
- Route 6/10 over I-95, Providence, Rhode Island (2018)
- Masters Road over Belle River, St. Clair County, Michigan (2018). This 55-foot-long bridge, erected in 1934, is listed on the National Register of Historic Places (Figure 14).



Figure 14 Masters Road Belle River Bridge

1.7.5 UHPC versus Conventional Concrete

In the entire University of Connecticut study, only Kruszewski (2018) makes a limited comparison of UHPC to conventional concrete. Kruszewski conducts a series of ‘push-out’ tests

intended to evaluate the behavior of studs welded to the beam web. The performance of four UHPC mixes (one without fiber) are compared to a HSC mix having 8 ksi 28-day compression strength. The HSC push-out specimens are shown in Figure 15a; one specimen is tested with internal reinforcement (shown) and one without. None of the UHPC specimens had internal reinforcement beyond the steel fibers in the mix; all have the same dimensions and stud details shown in Figure 15. The 0.5 in. diameter studs are 2 in. long and welded to a 0.375 in. web at a spacing (pitch) of 2 in. along the line of loading. The concrete and UHPC cast-in-place panels are 10 in. wide and 2.75 in. thick resulting in 5 in. side cover and 0.75 in. top cover over the studs. The benchmark single stud capacity, Q_n , for all tests is reported as 14.7 kips, governed by fracture of the stud. Provines et al. (2019) recommend reducing the stud capacity by a factor of 0.7, reducing the benchmark capacity to 10.3 kips.

It is important to note that the test arrangement does not comply with AASHTO LRFD §6.10.10.1 requirements for stud pitch (greater than 6 stud diameters = 3 in.) or top cover (greater than 2 in.). Provines et al. propose that the minimum pitch can be safely reduced to 4 stud diameters. The 2 in. top cover requirement, on the other hand, is presumed to address durability (corrosion) rather than stud capacity. For interior exposure, ANSI/AISC 360-16 requires only 0.5 in. top cover. Nonetheless, reduced cover with no additional reinforcement may be expected to split, especially when a cluster of studs is called upon to transfer large loads in a small area.

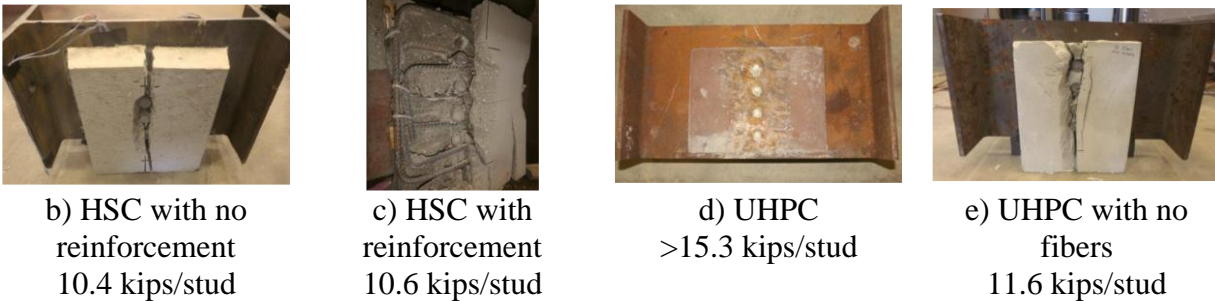
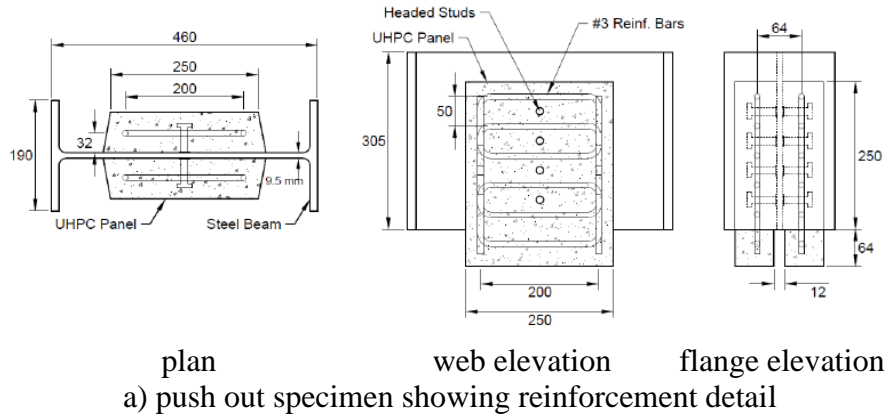


Figure 15 Push Out Tests of HSC and UHPC (Kruszewski 2018)

As should have been expected, the unreinforced HSC push-out test split along the line of studs in a brittle manner (Figure 15b). The ultimate capacity was reported to be 10.4 kips/stud although the slip before failure was only 0.04 in. The reinforced HSC specimen (Figure 15c) remained intact, exhibiting a ductile failure with 0.37 in. of slip although the capacity was only 10.6 kips/stud. The comparable UHPC specimens achieved capacities ranging from 15.3 to 17.0 kips/stud at slip values on the order of 0.17 in. and all exhibited stud shear failures (Figure 15d). Without fiber, however, the UHPC split longitudinally at a capacity of 11.6 kips/stud and a slip of only 0.1 in. (Figure 15e).

Kruszewski (2018) concludes that concrete failure governs behavior of studs in HSC and UHPC without fibers and does not recommend the use of either. However, taking into consideration the clustered stud tests and the recent work of Provines et al. (2019), this conclusion should be reconsidered. The reduced benchmark stud capacity (10.3 kips/stud) was barely

achieved in all cases. Furthermore, the reinforced HSC specimen achieved the recommended (EC4 2005) minimum slip to provide ductility (0.24 in.). Kruszewski, somewhat inexplicably, defines ductile failure of UHPC-embedded studs as “sustaining 90% of the capacity over a slip range of 0.16 in.”. This criterion appears to have been selected to satisfy the results of the testing conducted.

Without question, splitting must be mitigated. Internal reinforcement in HSC and fibers in UHPC were shown to accomplish this. It is hypothesized that greater top cover over the studs may also accomplish this objective. The 0.5 in. top cover provided is too small to provide adequate durability in a bridge application in any event.

1.8 Shear Stud Capacity

Using any encasement material requires force transfer to the existing steel. This is conventionally accomplished with shear studs. Single stud capacity, Q_n , is given by AASHTO LRFD as:

$$Q_n = 0.5A_{sc}\sqrt{f_c'E_c} \leq A_{sc}F_u \quad \text{Equation 1-15}$$

Where A_{sc} = area of stud

f_c' and E_c = strength and modulus of concrete

F_u = tensile strength of stud

Using the AASHTO-prescribed relationship between f_c' and E_c and assuming $F_u = 75$ ksi, it is easily shown that the right-hand term of Equation 1-12, the stud capacity, will govern capacity for concrete having f_c' greater than 5.3 ksi. For the sake of the foregoing discussion, it is assumed that $f_c' > 5.3$ ksi and the right-hand term of Equation 1-12 governs capacity.

The $A_{sc}F_u$ term implies that the full tensile capacity of the stud may be developed. If the stud were loaded in “pure” shear, its capacity would be $0.58A_{sc}F_u$. The reality lies between these extremes. Embedded in concrete, stud behavior is complex: the stud crushes into the concrete and the local stress transfer between stud and concrete results in a complex combination of shear, flexure and tension in the stud. To account for this, both Eurocode (EC4 2005) and Australian (AS 2004) standards reduce the right-hand term in Equation 1-12 to $0.8A_{sc}F_u$.

Additionally, Equation 1-12 is associated with stud dimension, spacing and detailing requirements. As is the case for other embedded anchors (see for example ACI 318-19 Chapter 17), clustering anchors close together in concrete reduces their individual capacity (i.e., capacity of the cluster is lower than the sum of the individual stud capacities). In a recent study focusing on AASHTO practice, Provines et al. (2019) address cases in which studs are ‘clustered’ and make a number of recommendations pertinent to AASHTO practice and relevant to the objectives of the present study:

1. Reduce minimum pitch of studs to four stud diameters from six in AASHTO LRFD §6.10.10.1.2.
2. Reduce minimum transverse spacing to three stud diameters from four in AASHTO LRFD §6.10.10.1.3.
3. Revise AASHTO LRFD Eq. 6.10.10.4.3-1 (Eq. 1-12 above) as follows:

$$Q_n = 0.5A_{sc}\sqrt{f_c'E_c} \leq 0.7A_{sc}F_u \quad \text{Equation 1-16}$$

4. Revise shear stud fatigue requirements to be expressed in terms of stress rather than force. Adopt a value of $(\Delta F)_{TH} = 7$ ksi for infinite fatigue life and the following for finite fatigue life:

$$(\Delta F)_n = (32,800 \times 10^6 / N)^{1/6.3} \quad \text{Equation 1-17}$$

Recommendations 1 and 2 will allow tighter clusters of studs on a beam web offsetting the loss of capacity associated with Recommendation 3. Since beam end repairs will primarily carry live load, Recommendation 4 will be critical to and likely ultimately control the stud design for such a repair.

1.8.1 Other Shear Connectors

Shear studs are simply mechanical connectors ‘rigidly’ attached to a steel substrate. Studs are welded to one side of a plate in a single-step process using a ‘stud gun’. One limitation of the stud welding process is that the substrate needs to have a uniform thickness and be relatively smooth. According to the American Welding Society Structural Welding Code - Steel (AWS D1.1), to avoid burn-through or distortion of the substrate, the substrate plate thickness must be at least one-third the stud diameter. Similarly, and more conservatively, AISC 360 states the stud diameter shall not be greater than 2.5 times the thickness of the base metal. Thus, according to AWS D1.1, a 0.5 in. stud should not be used on a plate less than 0.17 in. thick. Additionally, according to AWS D1.1, the surface of the plate needs to be SSPC SP2 – “hand tool cleaning at least 2 in. from the weld” in order to ensure uniform arcing of weld current. In new construction, these requirements are trivial, although in a beam end repair it may be necessary to weld a stud to a portion of web that has experienced section loss and/or is pitted due to corrosion. Welded shear studs may, therefore, may not be a practical option for beam end repairs.

When studs are required on both sides of a plate, such as in the proposed beam end repair application, alternative shear connectors may prove equally efficient (Figure 16). High strength threaded rods or bolts, inserted through the plate and nutted on both sides of the plate to maintain their ‘rigid’ attachment are preferable in repair scenarios. Such an approach avoids hot-work and

having to shoot shear studs onto a vertical surface (which requires special ferrules and more care to be taken in the welding process to ensure correct alignment of the ferrules and stud itself). Pavlovic et al. (2013) reported that 0.625 in. diameter high strength bolts achieve 95% of the capacity of 0.625 welded studs although the slip at service loads is greater. To mitigate these reductions, the bolted stud can be designed using a value of A_{sc} calculated based on the net area of the bolt. Additionally, since alignment is not a concern, oversized holes are not required: a stud may be placed into a hole of the same diameter. This minimizes slip and affects bearing at initial loading.

Kruszewski (2018) conducted push-off tests of conventional welded shear studs and bolted threaded rods in UHPC. The same diameter stud and rod were used, meaning the net area of the rod was about 70% that of the stud and its flexural stiffness was about 50% that of the stud. The tensile strength of the rods, however, was higher than that of the studs. Although the initial yield of the push-off tests having the threaded rods was lower, the ultimate capacities and slips of both rods and studs were comparable, a result confirmed by Pavlovic et al.

Bolted shear studs are commercially available from suppliers such as Tension Control Bolts, Ltd (TCB). The TCB bolted shear stud was evaluated at the University of Manchester (Tension Control Bolts 2022). The bolted shear studs were found to exceed the strength requirements for the European standard for high strength structural bolted assemblies (EN 14399-1). The study was silent on the issue of ductility.

In other applications, ‘concrete dowels’ are used to affect shear transfer. In this case larger holes are drilled through the steel web and concrete is allowed to flow through these producing a dowel. This approach is commonly used for steel embedments in composite construction where the concrete dowel typically includes a reinforcing bar through the web hole (e.g., El-Tawil et al.

2009). Kruszewski (2018) demonstrated this approach in push off tests using UHPC. 1.5 in. diameter holes through a 0.375 in. thick web developed 19.9 kips (shear stress on UHPC dowel = 11.2 ksi); 2 in. holes developed 25.4 kips (8.1 ksi).

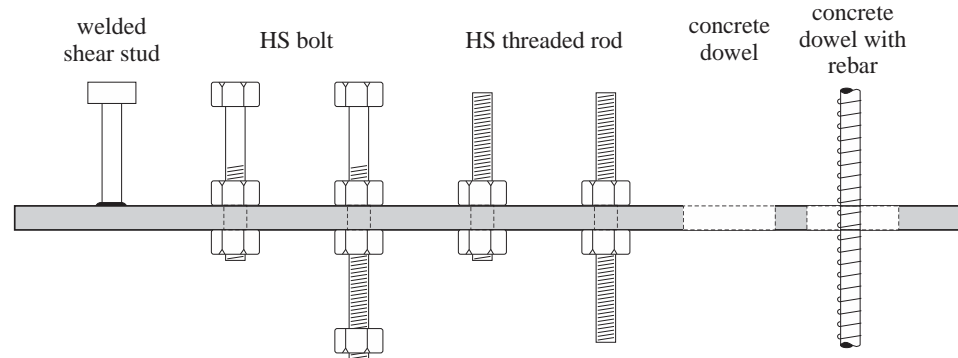


Figure 16 Alternatives to Welded Shear Stud Connectors

1.9 Fiber Reinforced Polymer (FRP) Based Repairs

Fiber reinforced polymer (FRP) composite materials combine high-modulus, high strength fibers in a low-modulus polymeric matrix which ensures load transfer between the fibers. The strength and stiffness of an FRP composite is largely determined by the fiber type and fiber architecture while the in-service performance is influenced both by the fiber and matrix material. Orientation of the fibers is controlled so that the resulting FRP system is anisotropic and may be tailored to suit the local structural demands in the component to which it is applied.

Carbon (CFRP) and glass (GFRP) FRP materials are ubiquitous in the field of structural repair. CFRP may be high strength (hsCFRP), high modulus (hmCFRP) or ultra-high modulus (uhmCFRP) (Table 10). GFRP (today, most typically based on ECR-glass fibers) have a much lower modulus than CFRP and are somewhat less expensive on a unit stiffness basis. To be effective in strengthening applications, the modulus of the FRP selected for a particular application

should be compatible with the substrate material. For this reason, CFRP materials are often used with a steel substrate.

A polymeric matrix binds and protects the fibers of an FRP, transferring force into, and between, fibers through interfacial shear. The matrix also provides stability and environmental protection to the embedded fibers. Epoxy resin systems are most used as the matrix in hand lay-up applications and as the adhesive in plate bonding techniques. Polyester resin systems are often used as the matrix material in procured (pultruded) composite materials such as those used for plate bonding applications.

In terms of ease of handling, installation, and quality control, precured CFRP plates or strips are rapidly becoming the preferred products for structural repair. The exception is that wet lay-up fabrics remain appropriate for applications involving irregular shapes or forming around corners. In either case the resulting system has a steel-adhesive-FRP interface region. Table 10 provides a summary of representative basic material properties for each layer in the system. The FRP properties are given for the composite product rather than for the raw fibers. Hand lay-up products will typically have lower strength and stiffness than those shown since the resulting fiber volume ratio is typically lower than in precured systems.

Table 10 Typical Properties of FRP Systems

	Mild Steel	Precured FRP Strips				Adhesive	
		hsCFRP	hmCFRP	uhmCFRP	GFRP	high modulus	low modulus
tensile modulus, ksi	29,000	24,100	30,000	44,100	6100	700	58
tensile strength, ksi	40-70	442	420	210	130	3.6	0.6
ultimate strain, %	18-25	1.8	1.4	0.5	2.2	1.0	>10
density, lb/ft ³	470	~100	~100	~100	~135	~75	~75
CTE, 10 ⁻⁶ /°F	12	~0	~0	~0	4.9	90	n.r.
T _g ^a , °F	-	300	300	300	resin	145	-
shear strength, ksi	-	-	-	-	-	3.6	1.3
bond strength, ksi	-	-	-	-	-	~3	~0.7
^a T _g = glass transition temperature							

A great deal of work has been conducted on the use of externally bonded FRP systems for structural strengthening of building and bridge systems and components. The overwhelming majority of this work has focused on the retrofit of concrete structures (ACI 440.2R-17). In virtually all existing applications, FRP materials are used to supplement steel reinforcement. Provided adequate quality control is executed, the behavior of externally bonded FRP is largely governed by the substrate concrete and the bond of the FRP thereto. This will not be the case for a stronger steel substrate, allowing more conventional bond mechanics to be used to describe debonding behavior (Harries and Dawood 2012).

In applications to steel, bond is critical. Harries and Dawood provide an extensive discussion of the chemistry and mechanics of FRP bond to steel substrates. A detailed discussion is beyond the scope of this literature review; in this study, best practices for bond are adopted.

1.9.1 Mitigating Crippling Induced by High Local Stresses

FRP ‘patches’ have been demonstrated to reinforce thin-walled steel structures against the crippling effects of concentrated transverse and axial loads (Zhao et al. 2006; Fernando et al. 2009). Zhao et al. investigated the use of CFRP wraps and plates to improve the web crippling behavior of cold-formed rectangular steel sections subject to end crushing (Figure 17a). The specimens had 4 in. tall webs having thicknesses of 0.08 in., 0.12 in. and 0.20 in. resulting in web slenderness ratios, d/t_w , ranging from 50 to 20. The CFRP plates used had a thickness of 0.05 in. and a modulus of 23,900 ksi. Thus, the effect of the bonded CFRP on the slenderness was equivalent to increasing the steel thickness 0.04 in. per CFRP plate. The presence of the CFRP plates increased the crippling loads, however not to the same extent as simply increasing the steel web thickness. Importantly, Zhao et al. concluded that the presence of CFRP sufficiently mitigated web buckling to permit web yield and, in some cases, strain hardening to develop. Based on the limited available research and the related research on inelastic buckling, it is felt that the effectiveness of such ‘in plane’ FRP patches is limited, most likely to cold-formed steel applications where the addition of the FRP represents a significant enhancement of local slenderness.

Okeil et al. (2009) proposed the use of adhesively bonded pultruded FRP sections as stiffeners for slender plate elements (Figure 17b). Okeil et al. focused on stiffeners for thin-webbed built-up steel sections and demonstrated that these may be designed in a manner similar to conventional steel stiffeners to control tension field action in such sections. Such adhesively-bonded FRP stiffeners are common in both new design and repair applications in aerospace and marine applications.

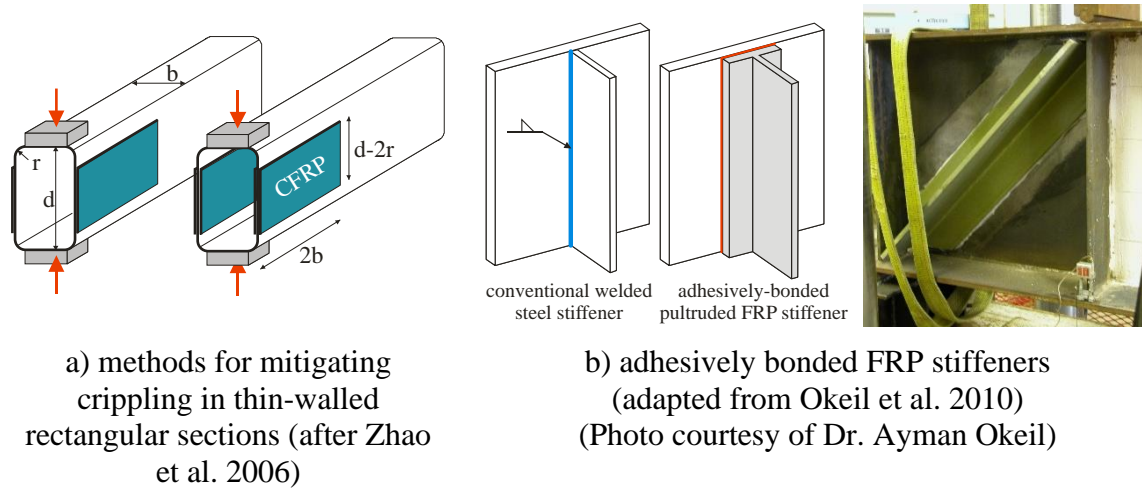


Figure 17 Use of FRP to Mitigate Crippling

1.9.2 FRP Repair of Corroded Beam Ends

In the only known study of its kind, Wakabayashi et al. (2013) proposed and demonstrated a CFRP repair of corroded beam ends. The proposed system is shown schematically in Figure 18.

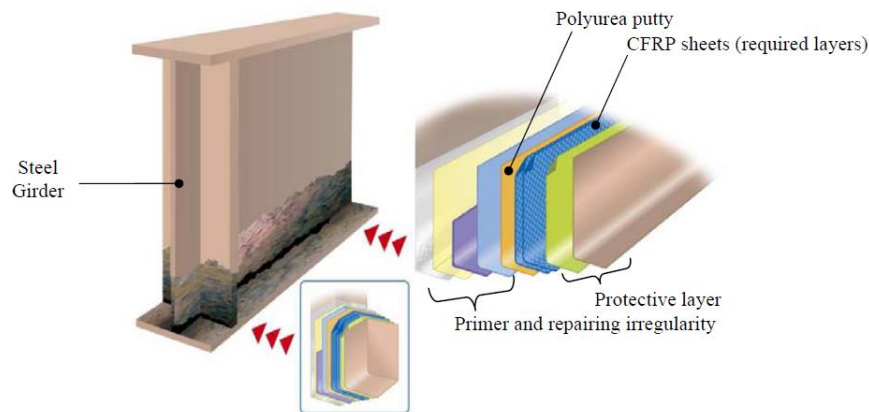


Figure 18 Schematic Representation of CFRP Repair of Corroded Beam End (Wakabayashi et al. 2013)

Two repair scenarios were demonstrated. The first, shown in Figure 18 involved restoring the bearing capacity of corroded bearing stiffeners. The design (uncorroded) capacity of the specimen was 431 kips. Artificially induced (machined) corrosion reduced this to 377 kips. The CFRP repair shown in Figure 19 restored the capacity to 448 kips.

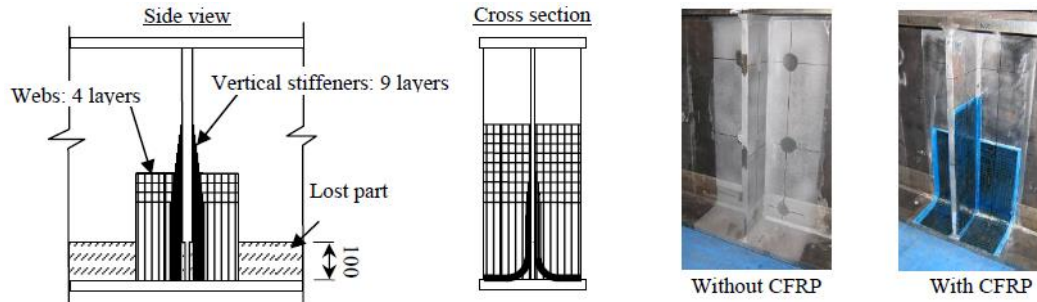
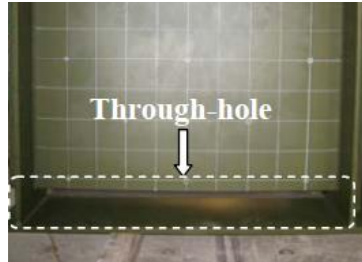


Figure 19 CFRP Repair of Corroded Bearing Stiffener (Wakabayashi et al. 2013)

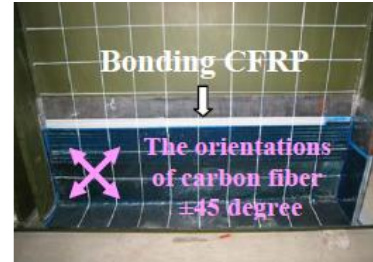
The second scenario demonstrated by Wakabayashi et al. was the loss of shear capacity resulting from a corroded hole at the web-bottom flange interface (Figures 20a and 20b). The repair is seen in Figure 20c, and the details shown in Figure 20d. The section is 51.2 in. deep having a 0.32 in. thick web. The beam was tested with a 51.2 in. shear span over a 25.6 ft simple span. The resulting load displacement curves of the uncorroded, deteriorated and repaired girders are shown in Figure 20e. The shear buckling capacity of the undamaged section was 312.2 kips. The damage shown in Figure 20b resulted in a reduced capacity of 262.1 kips. The repair restored the capacity to 332.5 kips.



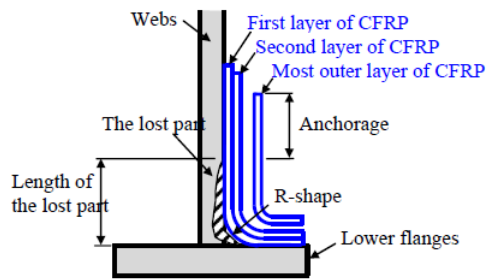
a) prototype corrosion damage



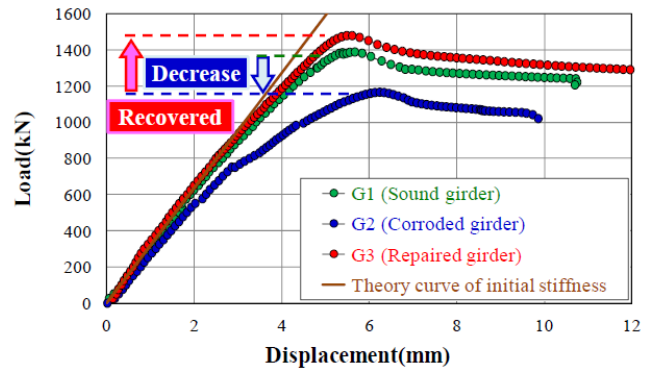
b) simulated test girder



c) CFRP repair



d) details of CFRP repair



e) load displacement relationships

Figure 20 Shear Repair of Corroded Beam End using CFRP (Wakabayashi et al. 2013)

2.0 Condition Review of Pennsylvania Bridges

In order to establish an overview of conditions in Pennsylvania, a review of bridge inspection reports was undertaken. Reports were provided by District Bridge Engineers based on a request for such information. Not all districts responded, and the reports provided were selected by the Engineers. Thus, this review is a snapshot rather than a representative picture of the state of Pennsylvania bridges affected by beam end corrosion. This Chapter provides a summary of this review. The complete review is reported in an Appendix to Harries et al. (2022).

Table 11 summarizes the 15 bridges (labeled A through O) reviewed. These were distributed geographically across the state as shown in Figure 21. The bridges range in size from short single lane bridges on rural roads (e.g., Bridges C, G and H) to bridges carrying interstate traffic (Bridges L, M and N). Eight bridges (B, D, I, J, K, L, M and N) were multiple span structures. The review included 145 beam ends over the 15 bridges. The focus of this study is end bearing regions which includes non-continuous beam supports at intermediate piers. Minor damage of continuous girders over pier supports was noted in Bridge L.

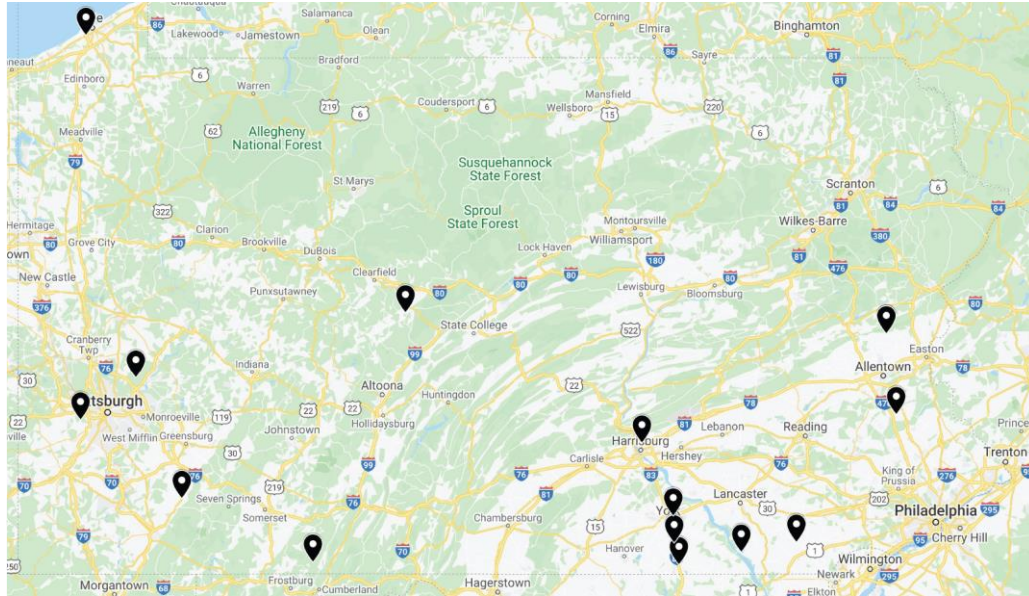


Figure 21 Geographic Distribution of 15 Bridges Reviewed

The degree of section loss (or remaining plate thickness) reported varies from very minor superficial corrosion to 100% section loss. Indeed, all but three bridges (C, E and L) exhibited some degree of complete web section loss. Many beams also exhibited notable bottom flange section loss. Where bearing stiffeners are present, these exhibited essentially the same damage as the web to which they are attached.

The observed corrosion damage follows the patterns described previously: beam end corrosion is associated with leaking expansion joints and is most prevalent at bottom-flange web interfaces where debris accumulates, trapping moisture. The presence of a bearing stiffener may make this problem worse, although the stiffener provides greater capacity to the bearing region.

Table 11 Condition Review Summary

Bridge	Girder	Span	Bearing type	NBI condition ¹	Load rating	End region damage ²
A	9-W18x60 at 4ft	23 ft	encased in concrete	3	15 ton	E-M3, E-W3, E-W1
B ³	4-W24 at 8ft	4 spans, noncomposite	steel plate	3	not posted	M1, W1
C	5-S12x31.8 at 4.25ft	12 ft	steel plate	4	not posted	W2, W3, W5
D	5-54 in. deep plate girders at 8ft	4 spans, composite	sliding plates, rocker bearings	4	not posted	M1, M3, W1, W4
E ³	5-W30 at 8ft	1 span, noncomposite	rocker bearings	4	not posted	W1
F ³	12-W14x38 at 4ft	1 span, noncomposite	encased in concrete	4	not posted	E-W1, E-W5, M1
G ³	8-W24 at 4ft	1 span, noncomposite	encased in concrete	2	closed	E-W1, M1
H ³	9-W24 at 4ft	1 span, noncomposite	encased in concrete	5	closed	M1,
I ³	7-18" I x 47# at 4ft	2 spans, noncomposite	none (bear on substructure)	5	not posted	E-W1, E-M3
J ³	5-48 in. deep plate girders at 10ft	13 spans, composite	sliding plates	5	not posted	M1, M3, W1, W2
K ³	5-60 in. deep plate girders at 10ft	3 spans, noncomposite	rocker bearings	5	not posted	M1
L ³	14-W30 at 8ft	3 spans, composite	rocker bearings	5	not posted	W1, W2, W3
M ³	14-W24x76 at 10ft	3 spans, composite	steel plates, rocker bearings	5	not posted	M1, M3
N ³	12-33 WF 130 at 10ft	4 spans, composite	sliding plates	5	not posted	M1, M3, W5
O ³	10-W24 at 8ft	1 span, noncomposite	encased in concrete	4	not posted	W3
¹ National Bridge Inventory Rating ² see Table 1 ³ girder section or spacing estimated from inspection report						

2.1 Girder Section Distortion

A few reports identified distortion of the corroded girders at the end bearings. Bridge B exhibits an extreme example of M1 damage: complete loss of the web section above the bearing extending approximately one bearing length into the span (Figure 22a). This bearing region also has what appears to be a cut through the entire flange just inboard of the bearing (Figure 22b). The combination of the loss of web section, the absence of a bearing stiffener, and the now nonsymmetric section resulted in a lateral displacement of the web as seen in Figure 22c. It should be clear from Figure 22 that without a bearing stiffener, this girder end is presently carrying no appreciable load. Bridge B has only four girders and therefore a considerable incremental load has been redistributed to the remaining three girders at this pier support. Although not noted and not seen in Figure 22, one expects a distortion of the flange to accompany this damage.



a) Pattern M1 damage
(b = 17 in.; a = 1.5 in.)



b) apparent cut through
bottom flange



c) lateral distortion of web

Figure 22 Lateral Distortion of Web Accompanying Significant Pattern M1 Damage (Bridge B)

The loss of web support at the bearing, particularly associated with Pattern M1 damage, leads to the lower flange being placed in flexure about its weak axis if some bearing resistance

remains. Bridge J, shown in Figure 23, has bearing stiffeners. In this case, the loss of web section has resulted in an obvious flexural distortion of the flange.



Figure 23 Flexural Distortion of Flange Accompanying Significant Pattern M1 Damage (Bridge J)

2.2 Previous repairs

Three of the bridges investigated show evidence of previous repairs. Bridge A, which exhibited relatively significant web section loss at the face of all embedded connections had been retrofitted with 2x4 timber frames (Figure 24a). These frames will maintain the support of the top and bottom flanges lost due to web deterioration but will not improve the shear capacity of the girders in the manner in which they are installed. This bridge is posted (15 tons) and it is likely that the slab is resisting most of the shear in this structure. Bridge D appears to show small regions of welded patches made to the web plates immediately above the bearings at Pier 3 (Figure 24b).

Finally, Bridge I has a steel-formed concrete encasement at the far abutment (Figure 24c). It is unclear why this encasement was provided. The embedded girder ends at the near abutment show significant deterioration including instances of complete web loss and near total flange plate loss. However, an inspection report made prior to the encasement being built does not identify a similar level of damage at the far abutment. The encasement itself is constructed of stay-in-place

vertical and horizontal steel plate forms spanning between girder webs. It is assumed that the abutment wall provides the back form. Concrete is then placed into this region from above.



a) timber retrofit to replace continuity provided by web (Bridge A)



b) Welded patch web plates above bearings at spans 3 and 4 over pier 3 (Bridge D)



c) steel-formed concrete encasement at abutment of bridge having embedded beams (Bridge I)



Figure 24 Previous Repairs Identified in Review of Bridge Inspection Reports

2.3 Selection of Archetypal Damage

Archetypal damage cases were selected from the review of Pennsylvania data. At the direction of the project sponsor, concrete-embedded connections (Bridges A, F, G, H, O) were excluded from consideration. Cases were selected to capture the range of girder dimension and end region details present in the data. Two conventional bearing regions, one stiffened plate girder (case I, based on Bridge D) and one unstiffened rolled section (case II, based on Bridge M), were selected. Each of these had 25% loss of section damage over the bearing and extending about 36

in. from the girder end. For simplicity, the assumed loss of section is best described as Pattern W3. Additionally, a region of 100% web loss above the bearing (Pattern M1) is also provided.

The damage is intended to be representative of severe, although potentially repairable, damage. Additionally, consideration is given to the ability to physically scale the archetypes for laboratory investigation. Table 12 summarizes the as-built (i.e., uncorroded) and as-is (i.e., residual corroded) capacity of the girder ends. Bearing stiffeners mitigate web yield and crippling but may, themselves be damaged. In such cases, web yield and crippling may become relevant limit states.

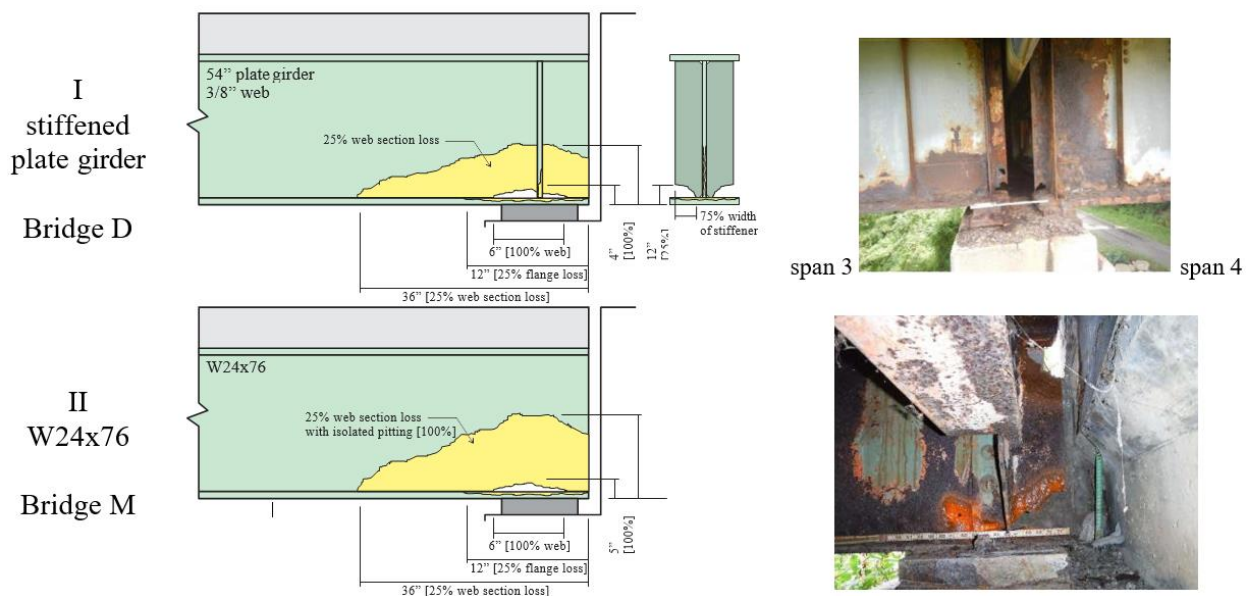


Figure 25 Archetypal Damaged Cases

Table 12 Bearing Region Capacities of Archetypal Damage Cases

(values in parenthesis indicate normalized residual capacity)

			I (54" plate girder)		II (W24x76)	
			as-built	as-is	as-built	as-is
web shear	F_y	ksi	36 ^a		50 ^a	
	D	in.	54	50	23.9	19
	tw	in.	0.375	0.28	0.44	0.33
	k		5		5	
	C		0.49	0.36	1.00	0.83
	V_{cr}	kips	208	108 (0.52)	305	182 (0.60)
web yield	N	in.	8		8	
	K	in.	1.25 ^a		1.18	
	twc	in.	0.375	0.21	0.44	0.22
	$R_{n,yield}$	kips	150 ^b	84 (0.56)	241	120 (0.50)
web crippling	d	in.	56		23.9	
	tf	in.	1.0 ^a	0.75	0.68	0.51
	N/d		0.14		0.33	
	$R_{n,crip}$	kips	103 ^b	36 (0.35)	185	47 (0.25)
bearing stiffeners	$width$	in.	7	1.75	-	
	tb	in.	0.625	0.47	-	
	R_{sb}	kips	394	47 (0.12)	-	
	P_{sb}	kips	315	59 (0.19)	-	
retrofit capacity required assuming NO load sharing		kips	208		185	
retrofit capacity required assuming load sharing		kips	V_{cr} : +100 R_{sb} : +161		V_{cr} : +3 $R_{n,yield}$: +65 $R_{n,crip}$: +138	
^a assumed value						
^b bearing stiffeners mitigate this limit state						

3.0 Repair Strategies

Several potential strategies were identified in Chapter 1. In this section, these are introduced in relation to the archetypal damage cases. Not all strategies will be applicable to each case. The following assumptions are made in this Chapter:

Assumption 1: The proposed structural repairs presuppose mitigation of the primary source of damage: leaking joints. All repairs have ‘boundaries’ with the existing steel. Regardless of material or detail, these are regions of potential crevice corrosion. The source of water and debris must be mitigated for any repair to have a reliable performance and lifespan. It is understood that the ‘microclimate’ occurring near the bearing regions of some bridges cannot typically be mitigated.

Assumption 2: Physical distortion of the beam end web should be corrected prior to strengthening. Distortion is especially expected if web crippling is dominating behaviour (see Figure 22). Flexural distortion (see Figure 23) must be considered as to its effect on the repaired beam end and corrected as required.

Assumption 3: Prior to repair installation, all corrosion product is removed. This is typically specified as “power tool clean and free of loss material” (SSPC-SP3). If adhesives are to be used, “white metal blast cleaning (SSPC-SP5) is typically required (NACE 2006).

Assumption 4: Typically, it is assumed that beam end repair will accompany bearing replacement. This being the case, it is assumed that the girder may be lifted to permit transfer of some self-weight to the repair material upon lowering the girder back into place.

3.1 Sample Designs

It is not possible to assess the demand on the bearing region without *in situ* bridge context. Where bearing stiffeners have been provided, it is reasonable to assume that the demand is close to the as-built capacity of the beam. In any case, assuming correct original design, it is conservative to take the controlling as-built capacity as the demand on the bearing region. This is done in this study. In many cases, this may be remarkably conservative since the selection of the beam is likely driven by flexural demand at midspan and the as-built shear capacities shown in Table 12 are not required to restore the capacity of the bridge structure itself. Thus, the calculation presented are worst-case scenarios.

Some repair approaches will permit some degree of load sharing between the as-is structure and the retrofit provided. In such a case, the demand on the retrofit is the difference between the residual as-is capacity and as-built capacity. Retrofit demand can become unclear when different limit states control capacity in the as-built and as-is condition. Once again, conservatively, the retrofit can be designed to carrying 100% of the as-built capacity. In this instance, all actions are considered.

The efficacy of the retrofit and its degree of load sharing are also functions of the *in situ* loading during the retrofit installation. For the example calculations presented in this Chapter, it is assumed that the beam end is entirely relieved during retrofit. Thus 100% of the combined residual and retrofit capacity of the beam is available post-retrofit. Furthermore, the calculations provided consider only the ultimate limit state (typically the AASHTO STRENGTH I load combination).

In the following Sections, illustrative examples of repairs of the damage cases are presented. The calculations presented are incomplete and simplified and are not intended to

provide definitive designs but to assess the viability and limitations of each repair scenario while highlighting some key issues.

3.2 Conventional Steel Repair

A ‘conventional’ repair of beam end corrosion damage involves welding or bolting steel plates or sections (typically angles) to the existing section (Figure 26). Considering the capacities shown in Table 12, it is clear that providing a new bearing stiffener, or restoring the capacity of an existing bearing stiffener, will restore considerable capacity to the beam end primarily by mitigating the web yield and crippling limit states. Considering Case II, the residual shear capacity (182 kips) is very close to the as-built limiting capacity (web crippling = 185 kips). This suggests that the addition of an effective bearing stiffener may be sufficient to restore the capacity of this girder.

Conventional steel repair is well suited for small, localized damage as the attached plates can span the damage. Larger regions of deterioration, however, require consideration as to whether the remaining sound steel substrate is suitable for bolting or welding.

3.2.1 Pros of Conventional Steel Repair

In most cases, new member thicknesses are matched to existing member thicknesses and conventional grades of structural steel (36 ksi and 50 ksi) are adequate, greatly simplifying the design process. Plate bending and hole drilling are common fabrication processes which require no specialized tooling and can be done in a fabrication shop, reducing field work. Contractors are

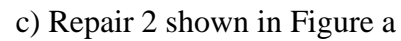
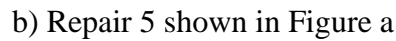
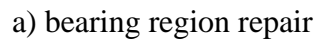
familiar with this type of repair method and no specialized tooling or labor are required. Design bases for steel are well established permitting quantitative designs to be executed.

3.2.2 Cons of Conventional Steel Repair

Field drilling or welding existing members *in situ* is required and may be affected by limited access. Bolting or welding to existing reduced sections needs to be considered and, particularly, the amplitude of the steel surface may affect the efficacy of connections. Optimally, connections should be made to sound steel and the repair designed to span the damaged region. This may lead to the need for heavier plates or stiffened repair elements.

Steel-to-steel joints must be properly sealed to avoid future issues with crevice corrosion (pack rust). Once again, if the cleaned steel does not have a typically 'smooth' surface, sealing this joint becomes more critical and more difficult.

Handling and inserting larger steel elements in the confined space of a beam end region may pose a challenge in some instances.



3.2.3 Sample Design: Conventional Steel Retrofit

Upon removal of the existing damaged bearing stiffeners, new angle stiffeners may be bolted to the section. Using the selection tables in the AISC Steel Construction Manual, a pair of L6x4x7/8 will resist 216 kips and provide ample room to bolt to the web. The new stiffeners must bear on the flange above the bearing and may therefore require an end plate. This detail is shown

in Figure 26c which shows a pair of L5x5x3/4 stiffeners having a capacity of 206 kips. Similarly, the damaged web and bottom flange can be ‘patched’ using a single ½-in. plate bent into an angle as shown in Figure 26b. If damage to the flange is deemed a concern, this patch could be double-sided 3/8-in. plate.

3.3 UHPC Encasement

UHPC encasement has been demonstrated by McMullen and Zaghi (2020), and Zmerta et al. (2017) and is described at length in the literature review. This method simultaneously provides a compressive strut to resist shear at the beam end and provides stability to the web. The method, shown in Figure 7 applied to a W21x55 section, involves partially or fully encasing the girder web in ultra-high-performance concrete (UHPC). Composite behavior is assured by the use of shear studs located in sound regions of the web. McMullen and Zaghi (2020) report that partial depth repairs may be susceptible to web crippling at the edge of the repaired region.

3.3.1 Pros of UHPC Encasement

The durability of UHPC is greater than conventional concrete and realistically no cracking of the fiber reinforced UHPC should be expected. Although not demonstrated, it is easy to envision how such UHPC encasement can address both girder and bearing deficiencies in a single operation. McMullen (2019) provides design recommendations for UHPC encasement repairs; these are reported in Section 1.7.3.2.

3.3.2 Cons of UHPC Encasement

Hot work is required to weld the shear studs to the existing girders. UPHC is a proprietary product. It is expensive and requires special handling during mixing and placement. Potentially complex formwork (see shaping of UHPC in Figure 7b) is required and all but partial encasement of deep webs will likely require top-down access through the bridge deck to place UHPC. Design recommendations are prescriptive, providing no means of calculating the effect(s) of strengthening.

3.4 Concrete Encasement

While UHPC may work well for deteriorated beam end repair, it is cost-prohibitive and may prove difficult to implement without specialized equipment and contractors. Other variations of high-performance concrete (HPC), however may be viable alternatives. Encasement in concrete materials other than UHPC differs only in that a reinforcing bar cage is likely required to provide adequate crack control (Kruszewski 2018). For this reason, full depth encasement is likely necessary.

It is reasonable to assume that encasement with a good quality concrete (say a mix having specified strength equal to 5 ksi) will be adequate to restore strength and stability to damaged beam ends. Durability can be enhanced using modified mix designs and adding fiber.

3.4.1 Pros of Concrete Encasement

High-performance (non UHPC) materials, such as fiber-reinforced, latex-modified, or hybrid concrete materials are often better established in industry and represent only a marginal cost premium over conventional concrete and a considerable savings compared to UHPC.

3.4.2 Cons of Concrete Encasement

Providing shear studs, reinforcing bar cages, and potentially complex formwork is required. Full depth encasement will likely require top-down access through the bridge deck to place. Design will be largely prescriptive in nature.

3.5 Shear Studs for Encasement Repairs

Encasement repairs, regardless of concrete type, require shear studs. For a beam end repair, this requires ‘hot’ work on a vertical surface in a confined space. Additionally, studs need to be installed on sound steel and their capacity will be significantly affected if applied to uneven surfaces such as are likely in corroded end regions.

Bolted shear studs (Figure 16) mitigate the need for hot work and are equally effective provided net section through the root of the thread is used as the stud area, A_{sc} (Kruszewski 2018; Pavlovic et al. 2013). Since web plates are typically relatively thin, installation can be made with a magnetic-base drill.

Although concrete-dowel connections have been demonstrated, their efficacy for thin webs is uncertain. However, a concrete dowel is naturally formed in regions of full section loss. Placing a small diameter reinforcing bar through larger web holes should enhance continuity over larger areas of section loss (Figure 16, right side).

3.6 Sample Design: Concrete Encasement

Since the bearing stiffener requires replacement, a full-depth encasement is proposed. The concrete must be sufficiently strong to replace the stiffener and should be similarly stiff. It will be easiest to form the encasement against the beam flanges making a ‘stub column’ over the bearing. Thus encasement will be assumed to be 16-in. wide and the length of the bearing (8-in.) long, making 128 in² of concrete. This replaces a pair of 7 x 5/8 stiffeners.

The existing stiffeners have a capacity of 315 kips although only 208 kips is required (Table 12). To achieve the former with the concrete stub column acting in bearing, a working concrete strength of only 2.4 ksi is needed. Furthermore, the concrete area is 14 times that of the steel it is replacing and thus will be axially stiffer. The typical ratio of $E_{\text{steel}}/E_{\text{concrete}}$ is 7 to 8 and falls for higher strength mixes.

Assuming a full depth concrete encasement, the shear stress resisted by the concrete is $208/(16 \times 54) = 0.24$ ksi. Neglecting the presence of confining reinforcement, and assuming the shear strength of concrete to be $0.06\sqrt{f'_c}$ [ksi], a very high strength concrete, having $f'_c = 16$ ksi is required. This suggests the need for UHPC encasement.

However, the large flange width should easily accommodate the inclusion of internal shear reinforcement and permit more refined design calculations. For instance, including #3 closed

hoops on each side of the beam web spaced at 6 in. provides a reinforcing steel component to the shear resistance, $V_s = (4 \times 0.11 \times 60 \times 50/6) = 220$ kips. In this case, conventional concrete encasement is easily used.

Finally, the concrete encasement and steel beam must be made composite. The shear carried by the beam web must be redistributed to the encasing concrete. This will be partially accomplished through concrete strut action anchored by the flanges but will also require studs be located along the web.

Assuming the use of 5/8-in. bolts having a net section area of 0.22 in² and using a rupture strength of 75 ksi, the capacity of a single stud is 11.5 kips (using the reduced AASHTO capacity recommended by Provines et al. 2019 described in Section 1.8) requiring only 20 studs to develop the required shear force.

Schematic examples of the resulting encasement details are shown in Figure 27. Because complete encasement is needed, top-down concrete placement is not possible. Figure 27 shows one approach that may be used to place concrete with a pump. In this arrangement, vibration of the concrete can be made through the formwork, using a form vibrator. The use of self-consolidating concrete (UHPC is self-consolidating) is also a promising approach for such applications.

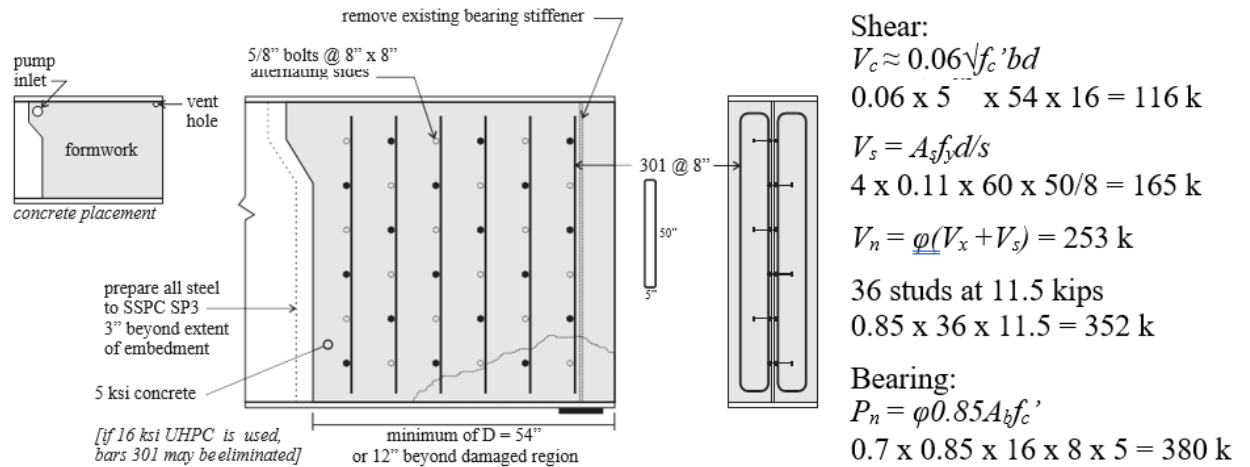


Figure 27 Conceptual Representation of Concrete Encasement Repairs

3.7 Repair Using Adhesively Bonded FRP Plate or Sections

For beam end repairs to be effective, the repair must restore both strength and stiffness of the beam end region. The most commonly available and least expensive FRP materials are glass-fiber based (GFRP). GFRP has a lower modulus than steel and therefore proportionally more material is required to provide the stiffness required for load sharing. Nonetheless, pultruded FRP plate ‘patches’ have been demonstrated to improve crippling resistance of slender steel sections (Zhao et al. 2006; Fernando et al. 2009; see Section 1.9.1). For larger loads or for use as bearing stiffeners, pultruded FRP sections (typically similar in form to rolled steel sections) may be preferable (Okeil et al. 2009). Figure 17 shows examples of each application.

3.7.1 Pros of Adhesively Bonded FRP Repairs

FRP materials are light weight and corrosion resistant. They are easily handled and can be cut and shaped on site with hand tools. Structural adhesive preparation and application is well known to contractors. Quantitative design is possible.

3.7.2 Cons of Adhesively Bonded FRP Repairs

Bonded repairs are susceptible to effects of poor surface preparation or adhesive application.

3.7.3 Sample Design: Bonded FRP Repair – Case 1

Bonded GFRP repairs take a similar design approach to conventional steel repairs. It is necessary to replace the functionality of the damaged steel with bonded GFRP. Since the repair is replacing steel, the expected behavior of the beam should remain essentially unchanged; thus, the repair must consider strength and stiffness. For this example, ‘off-the-shelf’ pultruded GFRP components are used. All material and geometric data has been obtained from a Pennsylvania-based manufacturer’s current catalog and design guide.

For a bearing stiffener, a WT section is proposed; this provides a large area for bonding to the existing web (flange width b) and reasonable axial compression capacity. The bearing stiffener will be fully supported over its length and therefore only local buckling of the outstanding web is a concern. BRP Design Guide (2012) provides allowable bearing stress based on slenderness: for a W shape having $b/t = 6/0.5 = 12$, the permitted bearing stress is 3.3 ksi. The area of the WT is

8.75 in² making the permitted axial capacity $8.75 \times 3.3 = 29$ kips (58 kips for both stiffeners), well below the required 208 kips.

Pultruded GFRP is easily built-up using adhesive bonding techniques. Fabricating a WT having similar dimensions from a pair of back-to-back 6x6x½ angles increases the area of the stiffener to $2 \times 5.75 = 11.5$ in² and reduces the slenderness of the stem to $b/t = 6$ permitting a bearing stress of 6 ksi to be used (BRB 2012). The axial capacity becomes $11.5 \times 6 = 69$ kips (138 kips for two stiffeners). The addition of a web plate underlying the angles will also contribute to the bearing capacity.

To reinforce the web, GFRP flat sheet is used. Because the pultrusion process varies, GFRP sheet material properties are marginally lower than pultruded shapes and are a function of plate thickness. The approach for the shear design is to assume the web to be entirely GFRP and calculate the capacity based on the total thickness of GFRP provided. Thus, the plate is designed to span regions of 100% section loss.

The critical shear buckling stress for an unstiffened pultruded GFRP plate is (ASCE FCAPS):

$$F_{LT}^{cr} = \left(2.67 + 1.59 \frac{G_{LT}}{\sqrt{E_L E_T}} \right) \frac{\sqrt[4]{E_L E_T^3}}{\left(\frac{d}{t} \right)^2} \quad \text{Equation 3-1}$$

Therefore, the required thickness of GFRP can be found by solving for t such that the required shear capacity, $V_{cr} = 0.8 \times F_{LT}^{cr} \times d \times t$ (the 0.8 factor is the recommended value for the material reduction factor, ϕ).

For the plate assumed, $E_L = 1800$ ksi, $E_T = 1400$ ksi, and $G_{LT} = 425$ ksi. Providing two 54-in. deep, ¾-in. flat sheets ($t = 1.5$ in.) gives a shear capacity of 231 kips. Adhesive bond stress is

$0.5 \times 231/54 = 2.2$ kips/vertical inch which is easily developed using a conventional structural adhesive.

The $\frac{3}{4}$ -in. plates will be bonded beneath the bearing stiffeners (see Figure 28) allowing them to contribute to the capacity of the stiffener. Using a permitted bearing stress of 8 ksi for the flat sheet (BRP 2012), the additional bearing capacity is $12 \times \frac{3}{4} \times 8 = 72$ kips, increasing a single bearing stiffener capacity to 141 kips. Assuming the flange is fully bonded, the shear that must be transferred by adhesive bond is: $141/(12 \times 54) = 0.22$ ksi.

The repair calculations shown are for general replacement of steel with GFRP. These were conducted to illustrate the viability of the method. In this case, it appears that the 54-in. deep section considered may be close to an upper limit on the utility of bonded GFRP sections.

Refining this approach for the archetypal damage assumed in Case I could result in a thinner web plate being used over the damaged region having partial section loss. The region of total web loss would be reinforced with an additional angle as shown in Figure 28, resulting in more than the full $\frac{3}{4}$ - in. GFRP thickness at this location. The entire GFRP assembly would be fabricated in the shop and adhesive bonded only to the steel on site. Care needs to be taken with the fillet detail; a reverse taper fillet should be used at all joints if possible

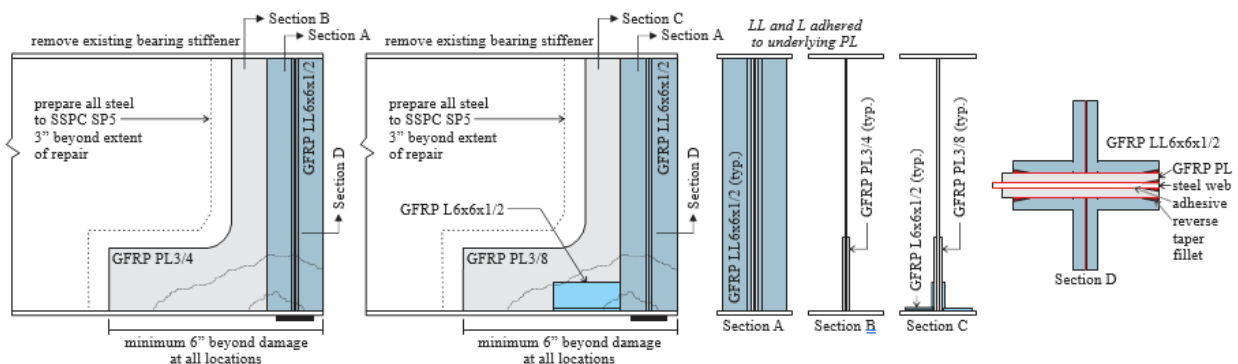


Figure 28 Adhesive Bonded FRP Repairs for Plate Girders

3.7.4 Sample Design: Bonded FRP Repair – Case 2

Case II requires the repair to establish web yield and crippling capacity with web yield capacity being 98% of that required. In such a case, providing a bearing stiffener that effectively mitigates these limit states is likely most efficient. The stiffener design would be very similar to that described in the previous section although the available flange width in this case is $b = 9$ in.

The allowable stress limits given by BRB (2012) can be shown to be conservative (Cardoso et al. 2014), especially for the cases in which one flange is fully supported as it is adhered to the web of the girder. BRB (2012) permits allowable bearing stress up to 10 ksi for all sections except angles. The lower 6 ksi limit for angles is understood to be based on the complex interaction of local, global, and torsional buckling behavior exhibited by angles. Since the angles are fully adhered to the girder web, these behaviors are mitigated in the present application and increasing the allowable bearing stress to 10 ksi is believed to be acceptable. In such a case, the capacity of the LL4x4x½ bearing stiffener is 75 kips (150 kips total). Like the repair shown previously, an additional web plate may be used to increase the capacity of the stiffener.

Another method of increasing the bearing capacity of the back-to-back angles is to bond an additional GFRP plate between the back-to-back legs of the angles (analogous to a gusset plate). This also reduces the slenderness (b/t) of the stem of the double angle assembly which increases the local buckling capacity and may permit a greater stress to be used. For the case shown, adding a 1-in. plate between angles increases the bearing capacity to 190 kips (Figure 29).

If additional web shear capacity is required, an inclined bearing stiffener arrangement could be adopted (see Figure 29b). As shown schematically, such an approach would include a ‘drag strut’ angle along the bottom flange to better anchor the diagonal shear strut. An additional flat plate is installed beneath the double angle to provide a uniform bonding plane.

Although the assembly shown in Figure 29b appears cumbersome, this would be fabricated in the shop. In most cases the tolerance available through the adhesive glue line will be adequate to assure full bearing. If bearing is needed at the top and bottom flanges, the assembly would be made slightly long in the shop and trimmed to fit in the field.

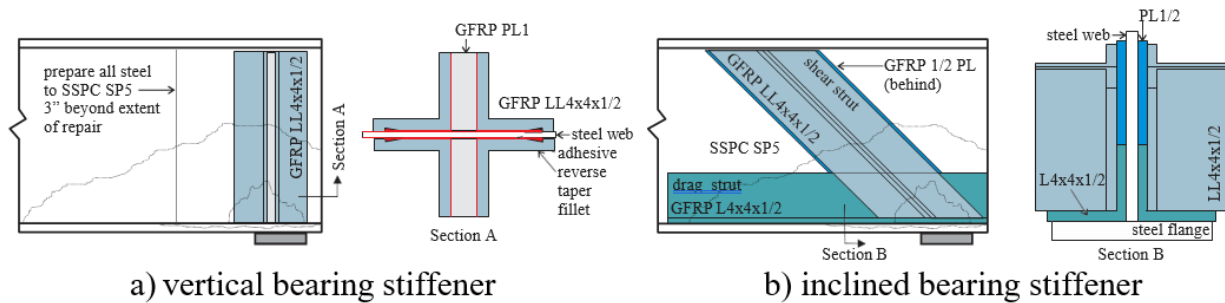


Figure 29 Adhesive Bonded FRP Repairs for Rolled Girders

3.8 Wet Lay Up FRP Repairs

Wakabayashi et al. (2013) demonstrated the efficacy of wet lay-up carbon fiber reinforced polymer repairs (CFRP) as shown in Figure 19. CFRP has stiffness approaching that of steel and therefore relatively thin repairs are possible. However, wet lay-up FRP materials are suited only to resisting membrane forces. Additionally, these materials rely on their substrate to provide stability. As a result, they are well suited to concrete repair but often ill-suited to steel repair where the restoration of stability may be a key requirement. Although Wakabayashi et al. illustrated a repair in which CFRP spanned a region of 100% section loss, the design was executed based on providing an amount of CFRP equivalent to the steel lost. This results in a large number of plies. Furthermore, the need to anchor the plies introduces a re-entrant corner at the web-flange interface

which will lead to adhesive peeling. It is assumed that this repair would perform very poorly under repeated loads.

Thus, it is believed that wet lay-up CFRP is only suited to restoring shear capacity to webs exhibiting partial section loss. Wet lay-up is unlikely to be effective in significantly improving web yield or crippling capacity. Out-of-plane anchorage (as would be required near a web-flange interface) will result in debonding of the CFRP especially under the effects of repeated loads.

3.8.1 Pros of Wet Lay-up

Wet lay-up CFRP repairs will be durable and have been demonstrated in countless bridge applications on concrete substrates. Wet lay-up applications are well suited for complex or variable geometry (although re-entrant corners lead to debonding) and are relatively easily executed even in confined spaces as they require no machinery or clamping.

3.8.2 Cons of Wet Lay-up

Wet lay-up repairs are susceptible to effects of poor surface preparation or adhesive application. Wet lay-up application of CFRP requires trained and certified contractors.

3.8.3 Sample Design: Bonded FRP Repair – Case 1

Wet lay-up FRP is a very thin application (design thickness on the order of 0.04 in. per FRP ply) suited for developing membrane forces. Such a thin application is not well suited to

spanning large regions of 100% section loss or for restoring section loss in compression elements (e.g., bearing stiffeners).

Wet lay-up CFRP can be used for restoring web capacity. If a web exhibits section loss α , it has a remaining steel thickness $(1-\alpha)t_w$. To restore the web capacity, CFRP equivalent of αt_w must be provided. The resulting design thickness of CFRP is:

$$t_{FRP} = \alpha t_w (G_s / E_{FRP, \pm 45}) \quad \text{Equation 3-2}$$

Typically, “high modulus” carbon fiber reinforced polymer product will be used for wet layup. These are described by their dry-fiber areal weight. For large strengthening applications, typically fabrics weighing about 18 oz/yd² are selected. These will minimize the number of plies required while still being sufficiently pliable to form to complex geometries and not sag upon application. The uniaxial design tensile strength and modulus of such products are $f_{fu} \approx 160$ ksi and $E_f \approx 10,000$ ksi with a design thickness of $t_f \approx 0.04$ in/ply.

For shear, the unidirectional fabric will be oriented at ± 45 degrees to the longitudinal axis of the beam (Figure 30). The resulting modulus of the CFRP in a ± 45 -degree orientation is approximately equal to the shear modulus of steel ($G_s \approx 11,400$ ksi), thus the CFRP replaces the steel in an essentially 1:1 ratio. Considering the design thickness of a single ply of CFRP is on the order of 0.04 in., multiple plies are required to restore even relatively minor material loss. The use of heavier CFRP sheets is possible although issues of sag of the material upon application may be an issue. This design approach is the same as proposed by Wakabayashi et al. (2013).

The ultimate strength of the CFRP patch is considerably greater than the steel it is replacing; nonetheless, this strength must be developed through adhesive bond. Typically, the CFRP patch will be ‘developed’ as shown in Figure 30. The anchorage length, L_a , should be based on the established capacity of the adhesive bond to steel and include some allowance for

positioning error/variability. Cadei et al. (2004) recommends a minimum anchorage length of $72t_{FRP}$. Typical values of adhesive shear strength are in the range of $\tau_a = 3.6$ ksi. Thus:

$$L_a > f_{utFRP}/\tau_a \geq 72t_{FRP} \quad \text{Equation 3-3}$$

In wet lay-up applications, a design FRP thickness, t_f , is provided and $t_{FRP} = t_f \times \text{number of plies}$. The actual *in situ* thickness will be different and should not be used as a basis for inspection

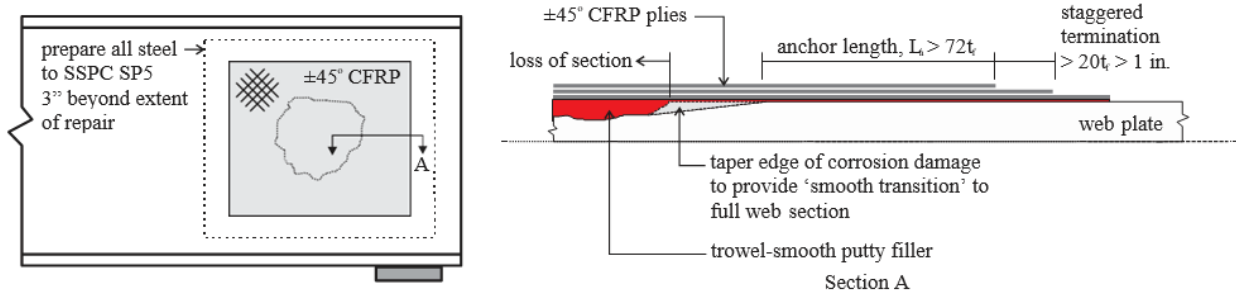


Figure 30 Details of Wet Lay Up CFRP Web Patch

or acceptance. The terminations of multiple plies should be staggered at least $20t_f \geq 1$ in. (Figure 30). Finally, a compatible putty filler is used to fill the existing region of section loss so that the surface to which the CFRP is applied has an amplitude variation less than 1/16 in.

3.9 Selection of Adhesive, Surface Preparation, and Details for Adhesive Bonding

Adhesive bonding to non-uniform steel substrates, as will be the case for cleaned, previously corroded surfaces, has one very distinct advantage: the adhesive is able to fill in the amplitude variations of the steel surface without meaningful loss of capacity. Indeed, a sound adhesive bond requires a roughened surface. Additionally, the adhesive will fill existing holes (100% section loss) resulting in a more homogeneous final product.

Nonetheless, there are several considerations in terms of steel surface preparation and adhesive selection and detailing that require attention. Sound adhesion to previously corroded steel likely requires SSPC-SP5 surface preparation: blasting to white steel (NACE 2006). This is the same degree of preparation required for repainting corroded steel. Additional care needs to be taken to protect the blasted surface from the reformation of oxides in the time between cleaning and adhesive application. A conventional organosilane primer has been shown to be effective in this regard (Harries and Dawood 2012).

There are several commercially available structural adhesives intended for steel substrates. The selection of an appropriate adhesive must include consideration of the viscosity or the addition of fillers to increase viscosity. An appropriate adhesive should self-support the adherends without the need for external support.

Edge conditions and the shape of any fillet can significantly impact performance of adhesively bonded patches. Assuming precured patches can be used, providing an edge chamfer in order to permit a reverse taper fillet to be used is desirable (Stratford and Chen 2005). Providing an additional fillet to ensure that water cannot accumulate along the adhesive edge is also good practice and provides environmental protection to the edge of the bond line (the fillet is sacrificial). FRP sections can be pultruded with UV inhibitors and do not need additional environmental protection, although cut edges do need to be sealed.

3.10 Section Replacement

Significant end region damage, particularly that resulting in significant section distortion, will typically require end region replacement such as shown in Figure 4. A variation of compete

beam end replacement that might permit a simpler construction process is to provide a dapped girder in lieu of a full depth girder replacement. In some cases, such a repair might be feasibly made with the girder in place and only jacked and lifted to transfer load from the deteriorated bearing region to the newly built dapped end. Figure 31 shows a schematic representation of dapped steel girders. Dapped steel plate girders were studied by the Texas DOT (Fry et al. 2005). Due to their reduced depth, tension fields can be better developed, in many cases improving the shear capacity of the dapped end.

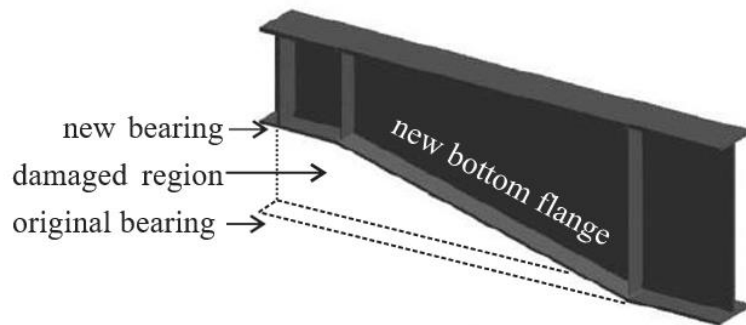


Figure 31 Dapped Plate Girders (based on Fry et al. 2005)

4.0 Test Specimens

4.1 Constraints on Test Specimen Selection

In order to optimize available resources, double-ended specimens were used. These were tested in the simple span arrangement shown in Figure 32. End A was tested as shown with End B cantilevered beyond the back span support. The beam was then rotated end-to-end, and End B tested in the same manner. In this case, the back span support for End A becomes the loading location for End B. In order to ensure constructability and that budget constraints were met, a steel fabricator (High Steel Structures) was engaged prior to testing to assist with specimen realization. The following constraints were considered in selecting the specimen design:

1. Achieve end region behavior similar to 54 in. plate girder archetype Case I described in Section 2.3.
2. Provide a “shear critical” test span-to-depth ratio, $a/d = 1.5$.
3. To mitigate damage at load point, a bearing stiffener is provided at this location.
4. In order to minimize damage at back span bearing, provide back span $a/d > 5$.
5. Static test capacity < 108 kips (two 60 kip rams operating at 75%).
6. Fatigue test capacity < 33 kips (50 kip actuator operating at 66%).
7. Based on fabricator recommendation and constraints for rotating specimens in lab, the overall specimen length was limited to 20 feet.

Since flexural behavior of the back span is not of interest in this study, behavior must remain elastic in flexure, specifically ensuring:

8. Top flange stability (flange local buckling).

9. Lateral stability (lateral torsional buckling).

Typically, such behavior is ensured by the presence of a deck. To clearly investigate steel behavior, the specimens were tested without a deck.

Following multiple discussions with the fabricator, a reduced scale plate girder having varying web plate thickness was initially proposed but rejected: the fabricator had a concern that it would not be possible to produce such a thin-webbed member and maintain web straightness/flatness tolerances. Such deviations would significantly impact the behavior being studied. As a result, trial designs focused on available rolled shapes. An advantage of using rolled shapes is that these are compact for flexure, therefore addressing constraint 8.

4.2 Test Specimen Design

It was desired to have the largest test specimen possible within the constraints provided. Multiple trial designs were considered. Ultimately a W24x55 was selected. This section, as rolled, is one of few with a non-compact web (web slenderness, $(d - 2t_f)/t_w = 57$). As a result, the experimental specimen is approximately a one-half scale replication of the Case I archetype.

Despite having a non-compact web, to better model the behavior of the 54 in. deep plate girder archetype, the web in the test region was further reduced from as-rolled $t_w = 0.395$ in. to $t_w = 0.20$ in. Although not achieving the very slender $D/t_w = 144$ of the plate girder archetype, a web slenderness of 113 is achieved (104 if the fillet region is taken into account). An advantage of using such a reduced-section rolled specimen is that gross section can be maintained at the loading

point and over the back span helping to address constraints 8 and 9 and ensuring elastic behavior outside the test span.

A summary of the test specimen design is presented in Figure 32. Details transmitted to the fabricator are provided in Appendix A. Both end regions are identical. A summary of all capacities for various test contingencies is provided in Table 13. Based on the spans shown, the shear in the test span, and moment applied to the specimen are:

$$V = 162P/200 = 0.81P \text{ [kips]} \quad \text{Equation 4-1}$$

$$M = (162 \times 36)P/200 = 29.2P \text{ [k-in]} \quad \text{Equation 4-2}$$

Where P is the applied load limited by constraints 5 and 6.

The shear capacity of the reduced section is $V_{cr} = 64$ kips (Table 13). This is the target capacity for retrofitting the damaged section. An expected capacity of $1.1V_{cr} = 70$ kips corresponds to an applied load $P = 87$ kips and peak moment of 2,540 k-in. The test frame static capacity is $P = 120$ kips, corresponding to $V = 97$ kips and $M = 3,504$ k-in. As shown in Table 13, the moment capacity of the W24x55 comfortably exceeds that which can be applied, ensuring the back span remains elastic and End B unaffected by the testing of End A to failure. Additionally, the test frame is able to apply 150% of the objective shear capacity if required.

The girders are braced laterally at their bearings and at the load point. This is sufficient to permit the full plastic flexural capacity of the girders to be developed prior to lateral buckling (M_n in Table 13), thus satisfying constraint 9.

Full width steel bearing pads 5 in. long were provided for all bearing locations and at the application of load. This results in a bearing length $N = 5$ in. The bearing was centered 3 in. from the test span end as shown in Figure 32.

Table 13 Summary of Specimen Design Checks for W24x55

capacity	note		54 in. archetype		W24x55 test specimen			
			as built	as is	gross section	as-designed reduced section	as-received reduced section	damaged section
F_y		ksi	36	36	50	50	57	50
					test span ($a/d = 1.5$)			
t_w		in.	0.375	0.28	0.395	0.20	0.326	0.167
t_{wc}	Eq. 1-7	in.	0.375	0.21	0.395	0.20	0.326	≈ 0.030
t_f		in.	1.0	0.75	0.505	0.505	0.505	0.375
V_{cr}	Eq. 1-1	kips	186	80	270	64	237	37
N		in.	10	10	5	5	5	5
R_{nyield}	Eq. 1-7	kips	177	99	149	75	140	11
R_{ncrip}	Eq. 1-8 & 1-9	kips	106	37	123	36	91	1.6
bearing stiffeners ($F_y = 36$ ksi)		in.	7 x 0.625	1.75 x 0.47	not required	3 x 0.5	3 x 0.5	-
R_{sb}	Eq. 1-12	kips	394	47		126	175	-
P_{sb}	Eq. 1-13	kips	315	59		108	150	-
R_{yield} at applied load		kips	-	-	226	226	258	226
					back span ($a/d = 6.75$)			
$M_y = SF_y$	gross section	k-in	-	-	5700	shear critical test region	potential for flexural inelasticity	shear critical test region
M_y	flanges only ^a	k-in	-	-	4180			
$M_p = ZF_y$	gross section	k-in	-	-	6700			
M_p	flanges only ^a	k-in	-	-	4267			
M_n	$L_b = 13.5$ ft $C_b = 1.67$	k-in	-	-	M_p			
^a neglecting contribution of web results in conservative capacity suitable for ensuring elastic behaviour								

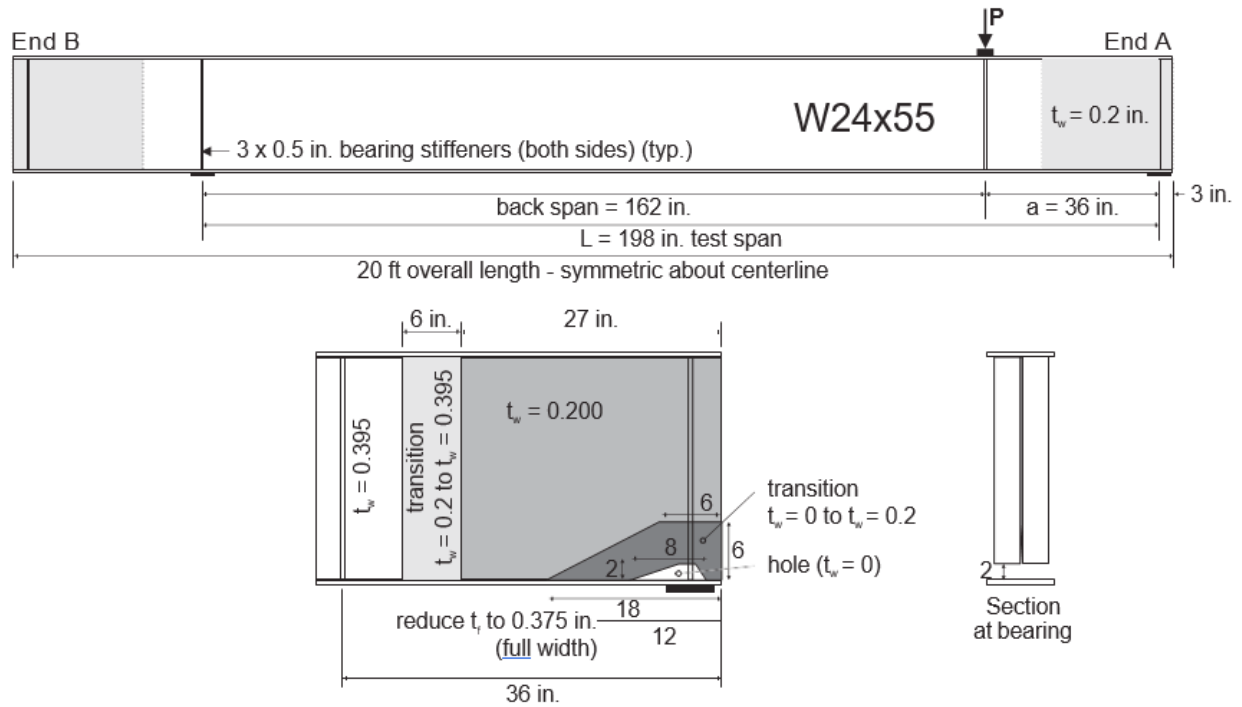














Figure 32 Proposed W24x55 Specimen

4.3 As-Received Test Specimens

Artificial ‘corrosion damage’ was machined into each girder end using a plasma torch to remove web and flange thickness. The fabricator was unable to meet the 0.2 in. thick web thickness requested in the specimen design. Each beam was marginally different and measured web thickness and section loss dimensions are summarized in Table 14. Web and flange thickness was determined using an ultrasonic thickness gage (Seesii model S-WT100A) across the reduced area shear span. Average thicknesses reported are determined over this region excluding the ‘corroded’ hole and are adopted as web thickness, t_w , for subsequent calculations. Table 14 also shows images of the region of 100% section loss at the bearing locations. The area of this region, A_{hole} , obtained

from image analysis, is also reported. Complete thickness reading matrices are provided in Appendix B.

Table 14 “Corrosion Damage” and Web Thickness (inches, COV in parentheses)

Girder	End A		End B	
1		$t_w = 0.326$ in. (0.030) $A_{hole} = \text{n.a.}$ $a_{max} = \text{stiffened}$	$t_w = 0.340$ in. (0.022) $A_{hole} = \text{n.a.}$ $a_{max} = \text{stiffened}$	
2		$t_w = 0.324$ in. (0.032) $A_{hole} = 10.38$ in ² $a_{max} = 0.11$ in.	$t_w = 0.312$ in. (0.031) $A_{hole} = 11.90$ in ² $a_{max} \approx 0$ in..	
3 ^a		$t_w = 0.305$ in. (0.029) $A_{hole} = 11.58$ in ² $a_{max} = 0.06$ in.	$t_w = 0.298$ in. (0.034) $A_{hole} = 13.57$ in ² $a_{max} = 0.07$ in.	
4		$t_w = 0.317$ in. (0.028) $A_{hole} = 12.61$ in ² $a_{max} = 0.03$ in.	$t_w = 0.265$ in. (0.055) $A_{hole} = 16.19$ in ² $a_{max} \approx 0$ in.	
5		$t_w = 0.281$ in. (0.031) $A_{hole} = 16.02$ in ² $a_{max} = 0.90$ in.	$t_w = 0.287$ in. (0.033) $A_{hole} = 18.44$ in ² $a_{max} = 0.19$ in.	
6		$t_w = 0.298$ in. (0.037) $A_{hole} = 14.39$ in ² $a_{max} \approx 0$ in.	$t_w = 0.315$ in. (0.052) $A_{hole} = 10.82$ in ² $a_{max} \approx 0$ in.	
^a The image of Girder End 3B was taken following testing. Girder labelling was revised following delivery; disregard small paper labels in images.				

A second issue associated with the method of reducing the web thickness used was that by ‘thinning’ the web on only one side, residual stresses were relieved resulting in the web distorting

into a ‘buckled’ shape. Temporary stiffeners were used to mitigate this effect although some specimens still exhibited web distortion prior to repair. Figure 44 shows an example of four beams during fabrication. In Figure 33, girder (b) is a W24 x 55 prior to web machining. Girder 8 (a) was fabricated without a temporary stiffener and the web distortion is readily apparent. While the girder geometry was partially restored using heat-straightening techniques, this girder was not used in this study. Nonetheless the degree of unrestrained distortion associated with machining is evident. Although the web of Girder 1 (d) is machined, the full depth, intact bearing stiffeners controlled section distortion. Girder 2 (c) shows the limited distortion that resulted when partial height stiffeners were provided. Once again, this issue with fabrication will require a more robust response from the repair techniques considered.

The web distortion was measured as the deviation of the web from straight at the mid-height of each girder end at the location of the bearing (i.e., 3 in. from the girder end). The values are reported as a_{max} in Table 14.



a) Girder 8; fabricated without a stiffener (not tested in this study) b) W24 x 55 prior to machining c) Girder 2 d) Girder 1

Figure 33 Section Distortion of Girder Specimens (photo: High Steel Structures)

4.3.1 Impact of As-Received Details

As shown in Table 14, the as-received test specimen capacity exceeded that anticipated.

This had two effects:

1. An increase in the test frame capacity (constraints 5 and 6) was required. In order to test the as-received beams, the static test capacity was increased to 280 kips (4 – 70-kip capacity hydraulic rams).
2. The fatigue actuator was run at 90% capacity, providing a maximum capacity of 45 kips.

Details of the test set-up and protocol are provided in Chapter 5.

4.3.2 Test Specimen Material Properties

All girders came from the same heat and mill certifications indicated yield and tensile strengths of 55 ksi and 73 ksi, respectively. Ten tension coupons were obtained from the web of Girder 1 following testing, five specimens in each of the longitudinal and vertical directions. There was no statistical difference in results for each coupon orientation. The measured yield strength of the girders was 57.5 ksi (COV = 0.06); the tensile strength was 77.5 ksi (COV = 0.01) and elongation at ultimate was 0.34 (COV = 0.06).

4.4 Repair Designs

Six girders were tested as shown in Table 15. In each girder, End A was tested under static load conditions to failure (i.e., a slow monotonically increasing load to failure). If an acceptable result was achieved after testing End A, End B was then fatigue conditioned and tested in a similar manner to End A. Details of the test protocols are provided in Chapter 5.

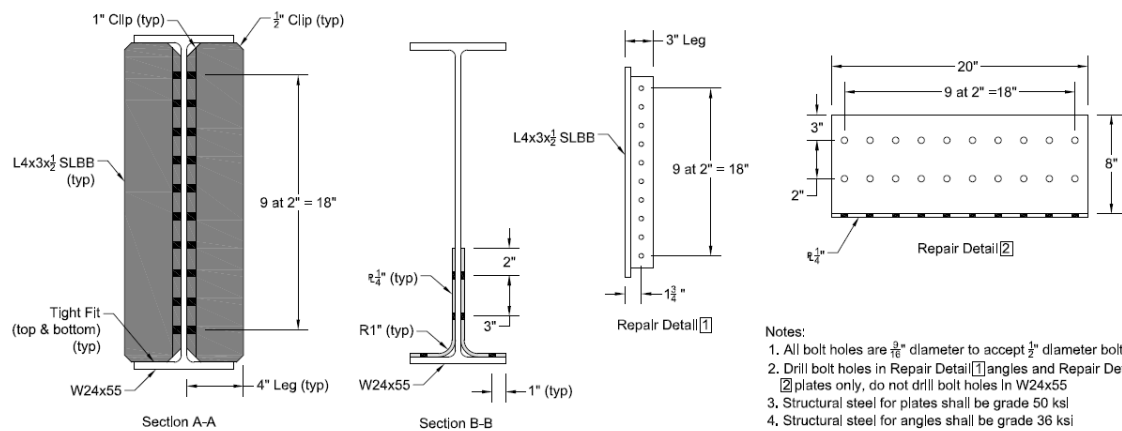
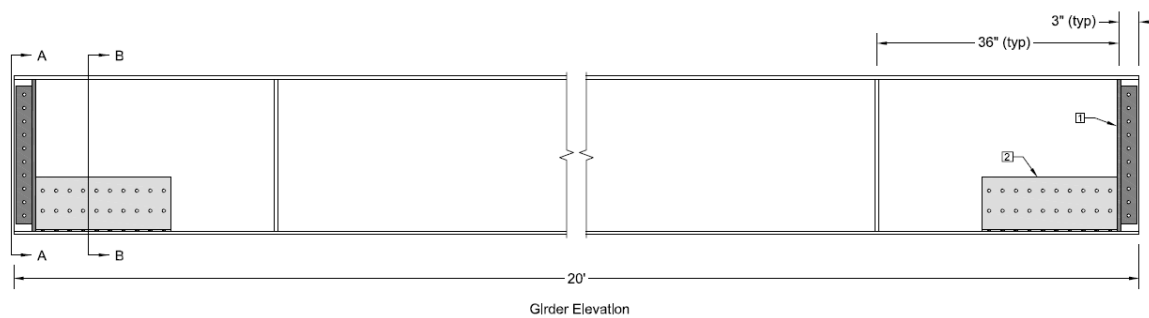
Table 15 Test Matrix

Girder	Repair Technique	End A	End B	Fabrication Detail
1	no damage control	static	not tested	Figure 32 without ‘corrosion damage’; includes undamaged bearing stiffeners
2	no repair control	static	not tested	as shown in Figure 32
3	conventional bolted steel ^a	static	fatigue	
4	UHPC	static	fatigue	
5	conventional RC	static	fatigue	
6	adhesive bonded pGFRP	static	not tested	
^a repair components were also be fabricated by High Steel Structures				

Girders 1 and 2 are tested in their as-received conditions. Girder 1 is the undamaged control used to benchmark the as-designed performance of the girders. Girder 2 is the damaged control, tested without repair. The following sections describe the designs of each repaired girder.

4.4.1 Girder 3 - Conventional Bolted Steel Repair

Girder 3 was a ‘control’ specimen. The bolted steel repair was intended to match as closely as possible to current practice. The bolted steel repair of Girder 3 (Figure 34) is essentially the same as that used to repair the archetypical damaged girder from Bridge D (see Section 2.3). The bolted steel repair design was based on industry standards for steel retrofits. The repair consists of replacing the damaged 3 x 0.5 in. bearing stiffeners with 3 x 3 x 1/2 SLBB angles. An additional bent 0.25 in. plate was used along both sides of the lower web-to-flange interface. 9/16 in. diameter holes were drilled into the web and flanges to accommodate the 0.5 in. diameter Grade 8 bolts that were used. All bolts were torqued to 110 ft-lbs which provides a pretension of 13.2 kips. The repair components were fabricated by the same fabricator who provided the beams. The material properties of the repair components was not determined.



- Notes:
1. All bolt holes are $\frac{9}{16}$ " diameter to accept $\frac{1}{2}$ " diameter bolts
 2. Drill bolt holes in Repair Detail 1 angles and Repair Detail 2 plates only, do not drill bolt holes in W24x55
 3. Structural steel for plates shall be grade 50 ksi
 4. Structural steel for angles shall be grade 36 ksi
 5. A higher grade steel may be substituted at no additional cost to the client

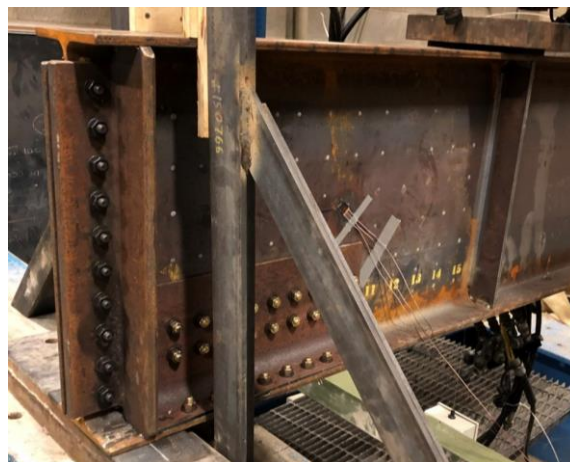


Figure 34 Bolted Steel Repair Detail for Girder 3

4.4.2 Girder 4 - UHPC Repair

Girder 4 was repaired using a full-girder depth UHPC repair located over the bearing and corrosion damaged region as shown in Figure 35. A total of 30 – 0.5 in. Grade 8 bolts were used as shear studs at each girder end. These were installed as shown in Figure 35 in an alternating arrangement. Given the thin and irregular web surface, it would not have been practical to weld studs to the test girder. No shear connectors were provided on the beam flanges.

The full-depth UHPC was placed into closed forms through a 6 in. PVC elbow (Figure 35) as has been demonstrated in the field (Hain and Zaghi 2021). Because of the toughness of the UHPC, the filled PVC was not easily removed and was left in place during testing.

LaFarge Ductal® 130 UHPC was used. This proprietary mix consists of a premix, liquid admixture and 2% steel fibers. The UHPC used for both beam ends was prepared in a single 4.1 ft³ batch using a 12 ft³ capacity mortar mixer. The mix proportions and mixing protocol used are given in Table 16. The mix protocol was prescribed by LaFarge and the temperature and flow at placement were within specifications. The manufacture-reported compression strength for this material is reported to be 14 ksi and 21 ksi at 4 and 28 days, respectively. As seen in Table 16, these specifications were achieved.

Girder 4A was tested at an age of 28 days. The fatigue conditioning of Girder 4B took place between days 62 and 72 and the final monotonic test of 4B took place at an age of 90 days.

PennDOT indicated that due to the high forces involved, 2 in. cube tests are sometimes used for UHPC. Although the data is limited, the cube compressive strength obtained in this study was markedly lower than the Lafarge-specified 3 in. cylinder tests. Further research is required to determine an appropriate relationship between cylinder and cube tests. Nonetheless, it is noted that

in order to adequately test 3 in. UHPC cylinders, a test machine having a capacity of at least 150 kips is necessary whereas cube tests may require only 100 kips.

Table 16 UHPC Mix Protocol and Measured Material Properties

	Girders 4A and 4B	mix procedure
date UHPC placed	4 August 2021	
batch size	4.1 ft ³	
UFTEC L premix	550 lbs	dry mixed for 2m
Ductal F4 admixture	5.5 lbs	added and mixed for 6m 15s
water	24 lbs	
ice	15 lbs	
steel fiber	40.7 lbs	added over 1m 35s and mixed for 2m
ambient temperature	74.3 °F	
mix temperature at removal from mixer	79.7 °F	
flow table (2 min.)	9 in.	
3 in. cylinder compressive strength at 53h	14.3 and 14.1 ksi	
3 in. cylinder compressive strength at 168 h	19.4 and 17.5 ksi	
3 in. cylinder compressive strength at 28 days	21.8 and 20.9 ksi	
3 in. cylinder compressive strength at 90 days	17.1 ^a and 22.7 ksi	
2 in. cube compressive strength at 28 days	16.9 and 13.1 ksi	
2 in. cube compressive strength at 90 days	18.9 and 20.6 ksi	
^a nonsymmetric failure attributed to poor end-grinding		

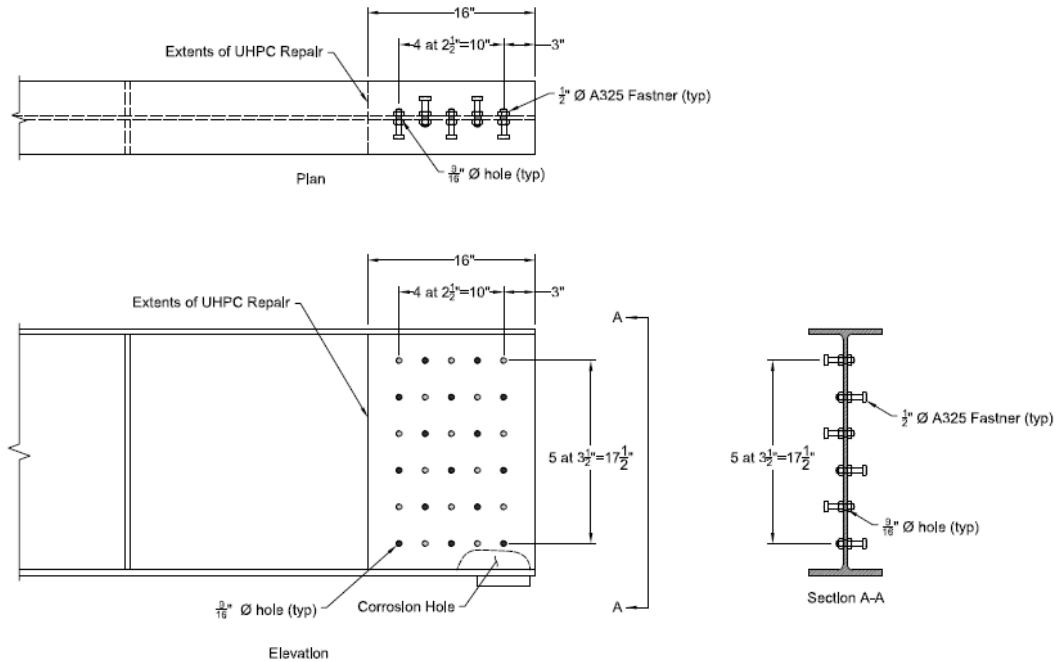


Figure 35 UHPC Repair Detail for Girder 4

4.4.3 Girder 5 - Reinforced Concrete (RC) Repair

Girder 5 was repaired using a full-girder depth conventional RC repair located over the bearing, corrosion-damaged region, and extending the length of the shear span to the point of load application (Figure 36). To provide confinement, vertically oriented #3 hairpins were placed through 1 in. diameter holes in the web to effectively create closed tie reinforcement. Three horizontally oriented ties were located above the bearing region to better confine this highly

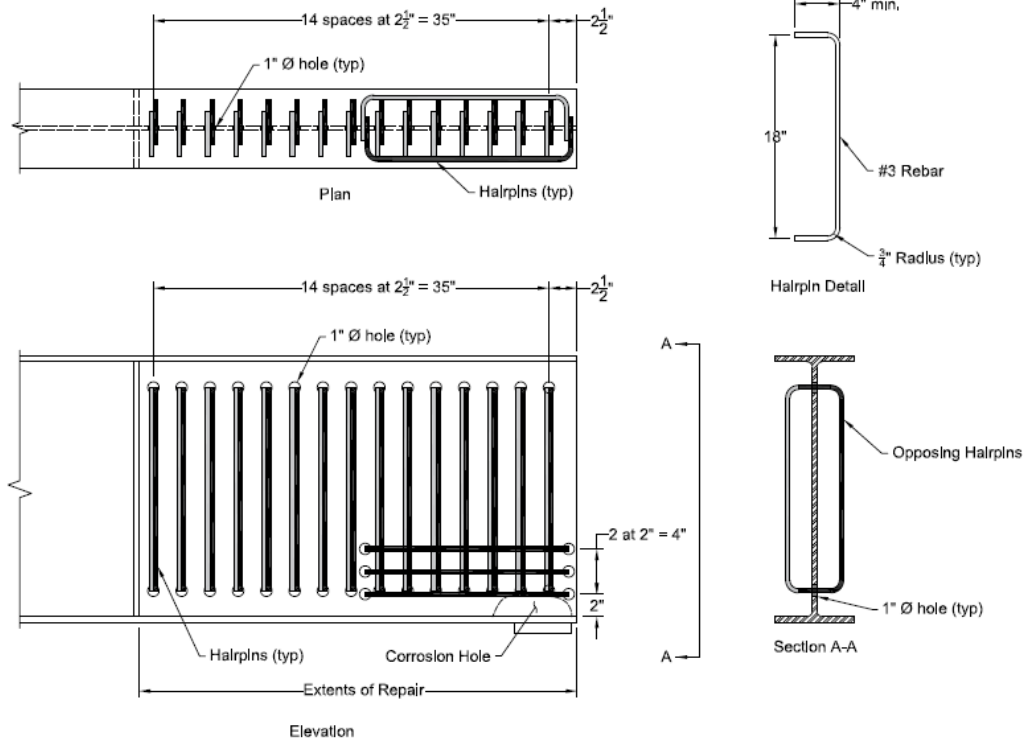
stressed region and to help react the expected diagonal concrete compression strut anchored at the bearing. The measured yield and tensile strengths of the #3 bars used were 74.1 ksi and 111.7 ksi, respectively. The reinforcing ties provide the only shear connection between the concrete and web; no studs were used.

At the request of PennDOT, a relatively low strength concrete was used with the target strength being 4,000 psi. Sakrete 5000 premixed concrete was used. This mix reports a cement (Type I/II) content of 10-30%. For the purposes of calculation, 20% cement content was assumed. The concrete was mixed and placed in the same manner as the UHPC: mixed in a 12 ft³ mortar mixer and placed into closed forms through a 6 in. PVC elbow. The concrete was internally vibrated using a conventional wand vibrator. Girder end 5B was placed first and the mix was barely workable for the application. Additional water was added for 5A, resulting in a lower strength. The mix proportion and material properties of the concrete used are given in Table 17.

Girder 5A was tested at an age of 28 days. The fatigue conditioning of Girder 5B took place between days 77 and 87 and the final monotonic test of 5B took place at an age of 91 days.

Table 17 RC Mix and Measured Material Properties

	Girder 5A	Girder 5B
date of concrete placement	3 August 2021	3 August 2021
batch size	4 ft ³	4 ft ³
Sakrete 5000 premix	660 lbs	660 lbs
water	10 gal	8.3 gal
assumed w/c	0.63	0.52
28-day compression strength (ASTM C39)	3161 psi (0.034)	4560 psi (0.072)
28-day split cylinder strength (ASTM C496)	291 psi (0.060); $5.2\sqrt{f_c}$	393 psi (0.032); $5.8\sqrt{f_c}$
91-day compression strength (ASTM C39)	-	4920 psi (0.014)



a) holes for steel hairpins



b) steel hairpins in place



c) completed concrete encasement

Figure 36 Reinforced Concrete Repair Detail for Girder 5

4.4.4 Girder 6 - Glass Fiber Reinforced Polymer (GFRP) Repair

Girder 6 was repaired using adhesively bonded GFRP plates and pultruded I-sections. Surface and bond preparation follows best practices (Harries and Dawood 2012). The steel surface to which the GFRP was bonded was first cleaned to an SSPC SP5 specification, blasting to white

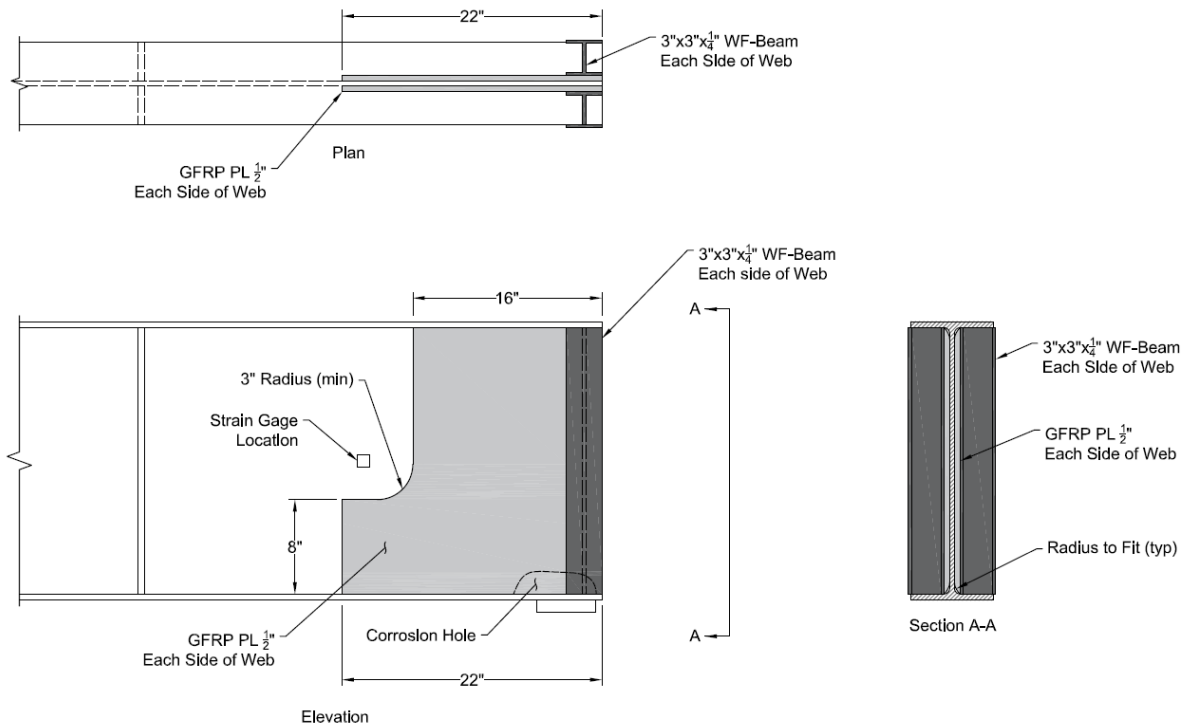
steel (Figure 37). A portable sand blasting unit was used. The GFRP surface to be bonded was lightly sand blasted to scar the resin-rich surface in order to enhance bond. Prior to adhesive installation, the steel and GFRP bonding surfaces were cleaned using compressed air and a primer consisting of 0.5% γ -GPS silane in aqueous solution (Sigma Aldrich 440167) was applied and allowed to dry for about 1.5 hours. SikaDur[®] 32 epoxy adhesive was used and was applied in a thin layer to both sides of the bonding interface. Due to the relatively short pot life of SikaDur 32 (under 30 minutes), only one end of the beam was repaired at a time.

First, 0.5 in. GFRP plates were adhered to the entire web depth. The plates were installed such that their 'longitudinal' or strong direction was oriented vertically. Following installation of the plate, WF 3 x 3 x ¼ bearing stiffener sections were immediately applied on top of the 0.5 in. plate. Once installed, a clamping force was applied sufficient to bring all surfaces of the GFRP and steel web into contact. The entire clamped assembly was left in place overnight. Although the outermost flange of the WF extends beyond the flange width, the presence of the WF flange provides support to the GFRP web resulting in a greater bearing capacity than if a WT were used.

Material properties of the GFRP and adhesive are given in Table 18. The GFRP used in this study was stock left over from previous studies. Measured material properties are those reported in these earlier studies.

Table 18 Material Properties of Pultruded GFRP and Adhesive

shape	0.5 in. plate		WF 3 x 3 x ¼		SikaDur 32
source of measured properties	manufacturer-reported (Bedford Plastics 2012)	measured (Cunningham et al. 2015)	manufacturer-reported (Bedford Plastics 2012)	measured (Cardoso 2014)	manufacturer-reported (Sika 2020)
resin type	polyester		vinyl ester		100% epoxy
d	-		3 in.	3.02 in.	-
b	-		3 in.	2.94 in.	-
t	0.5 in.		0.25 in.	0.25 in.	-
E_{Lt}	2000 ksi	3160 ksi	2500 ksi	3180 ksi	540 ksi (14d)
F_{Lt}	24 ksi	54.2 ksi	30 ksi	-	6.9 ksi (7d)
E_{Tt}	1400 ksi	1000 ksi	800 ksi	1770 ksi	-
F_{Tt}	10.0 ksi	11.4 ksi	7 ksi	-	-
E_{Lc}	-	-	2500 ksi	3710 ksi	210 ksi (7d)
F_{Lc}	-	-	30 ksi	62.4 ksi	12.2 ksi (14d)
G_{LT}	-	-	450 ksi	685 ksi	-
shear strength	-	-	-	-	6.2 ksi (14d)
bond strength to steel	-	-	-	-	2.0 ksi (14d)
elongation	$F_{Lt}/E_{Lt} = 1.2\%$	$F_{Lt}/E_{Lt} = 1.7\%$	$F_{Lt}/E_{Lt} = 1.2\%$	-	1.9% (7d)
viscosity	-	-	-	-	4500 cps
pot life	-	-	-	-	30 min
E_{Lt} and F_{Lt} = modulus and strength in longitudinal direction determined from tension tests E_{Tt} and F_{Tt} = modulus and strength in transverse direction determined from tension tests E_{Lc} and F_{Lc} = modulus and strength in longitudinal direction determined from compression tests G_{LT} = in-plane shear modulus					



a) SSPC SP5 surface preparation



b) installation of FRP



c) completed FRP repair

Figure 37 GFRP Repair Detail for Girder 6

5.0 Experimental Testing Program

5.1 Test Set Up

All tests are conducted in simple span flexure over a test span of 198 inches and a shear span of 36 inches (Figures 38 and 39). Tests are conducted in a 400-kip capacity self-reacting steel frame.



a) Monotonic Tests of Girder Ends A



b) Fatigue Conditioning of Girder Ends B



Figure 38 Overall Views of Test Set Ups

5.1.1 Monotonic Tests to Failure

Monotonic (or ‘static’) tests to failure were conducted using four – 70-kip capacity hydraulic cylinders (Figure 38a). The cylinders have a compression area of 7.22 in² and are driven with a 10,000-psi electric pump. Load is applied gradually using a regulator valve and pressure is recorded using a precision transducer. The transducer precision is 0.001 over full scale, resulting in a precision of the reported applied load being 288 lbs.

Test are conducted monotonically to failure. Considering the need to record data and monitor the specimens for damage, each test takes approximately one hour, a load rate on the order of 4 to 5 kips/minute.

5.1.2 Fatigue Conditioning

End B of each girder was tested using the following fatigue conditioning protocol. The intent was not to affect a fatigue failure, but to replicate years of service – fatigue conditioning – after which the girder end was tested monotonically to failure. The static capacity of Ends A and B were then compared, and differences attributed to the effects of fatigue conditioning. Because of the poor brittle performance of 6A, fatigue conditioning of 6B was not undertaken (Table 19).

Fatigue loads were applied using a 50-kip capacity servo-controlled hydraulic actuator. Load and displacement were obtained from the integrated actuator load cell and LVDT. The reported load precision was 0.01 kips and displacement was 0.001 in.

The fatigue conditioning protocol involved 1 million cycles of applied load, $P_{fatigue}$, cycling between 4 kips and 44 kips. Thus, the average or baseline applied load was 24 kips and the full cycle amplitude was 40 kips: that is the fatigue loading was 24 ± 20 kips. Fatigue load was applied at a frequency of 1.2 Hz, resulting in a test rate of approximately 100,000 cycles per day allowing for instrumented cycles.

The ratio of fatigue load to design load is a function of bridge geometry and loading and will vary to some extent. Two well-established ‘design examples’, 1 and 2A from the Steel Bridge Design Handbook (Barth 2015; Grubb and Schmidt 2015, respectively) were used as the basis for establishing the fatigue load for shear as a proportion of the design load. In Example 1, the ratio

of shear demand under FATIGUE I load condition to that under STRENGTH I, $V_{\text{FATIGUE}}/V_{\text{STRENGTH I}} = 0.167$; the same ratio is 0.165 for Example 2A.

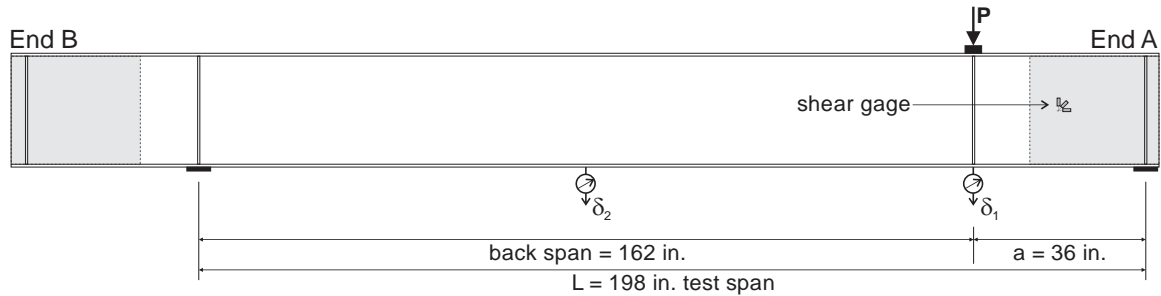
For Girder 1A, the experimentally observed shear capacity was $V = 213$ kips. In consideration of the variation of as-received girder capacities and the limitations of the fatigue actuator, the amplitude of the fatigue load was selected to be 40 kips, resulting in a shear of 32.8 kips and ratio of $V_{\text{FATIGUE}}/V_{\text{STRENGTH I}} = 0.154$ based on Girder 1A. This ratio will be marginally greater for the other girders which all have thinner webs.

It is not practical to provide continuous instrumentation for fatigue conditioning. Applied load, deflections and strain gage-measured strains were monitored during ‘instrumented cycles’ as follows. Fatigue loading was paused. Data was reported at the baseline load of $P = 24$ kips and at a single load cycle to $P = 44$ kips. Instrumented cycles were conducted on a logarithmic schedule at cycles 1, 2, 5, 10, 20, 50, 100, 200, 500, 1000, 2000, 5000, 10,000, 20,000, 50,000, 100,000 and every 100,000 cycles thereafter.

5.1.3 Instrumentation

Figure 39 summarizes the instrumentation layout, described as follows. Vertical girder displacements (δ_1 and δ_2) were obtained in the monotonic tests using draw-wire transducers having a precision of 0.004 in. Displacement δ_1 during fatigue tests was obtained directly from the actuator transducer with a precision of 0.001 in.

A triaxial electrical resistance strain gage (i.e., shear gage) was installed in the middle of the 36 in. shear span at the girder mid-depth (neutral axis). Using a triaxial gage, the oriented shears, maximum shear strain and orientation of the maximum strain were obtained as shown in Figure 39c. All strains were recorded with a precision of 1 microstrain.



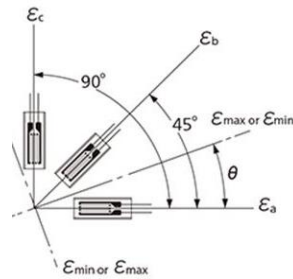
a) overall span instrumentation



b) draw wire transducers



c) shear gage



maximum and minimum principal strains:

$$\epsilon_{max} = 0.5 \left[\epsilon_a + \epsilon_c + \sqrt{2[(\epsilon_a - \epsilon_b)^2 + (\epsilon_b - \epsilon_c)^2]} \right]$$

$$\epsilon_{min} = 0.5 \left[\epsilon_a + \epsilon_c - \sqrt{2[(\epsilon_a - \epsilon_b)^2 + (\epsilon_b - \epsilon_c)^2]} \right]$$

maximum shear strain:

$$\gamma_{max} = \sqrt{2[(\epsilon_a - \epsilon_b)^2 + (\epsilon_b - \epsilon_c)^2]}$$

direction of principal strain

$$\theta = 0.5 \tan^{-1} \left[\frac{2\epsilon_b - \epsilon_a - \epsilon_c}{\epsilon_a - \epsilon_c} \right]$$

d) shear gage calculations

Figure 39 Instrumentation

5.2 Girder End A Monotonic Test Results

In the discussion of test results, girder shear, V , is reported. That is the value of the reaction force at the bearing nearest the applied load, P . In all cases, $P = 1.22V$. The applied moment, $M = 3V$ (kip-ft). Additionally, due the variation in web thickness, it is convenient to report shear in terms of shear stress, $\nu = V/dt_w$; where $d = 23.6$ in. is the depth of the section and t_w is the average measured web thickness in the reduced-thickness portion of the shear span given in Table 14 and repeated in Table 19.

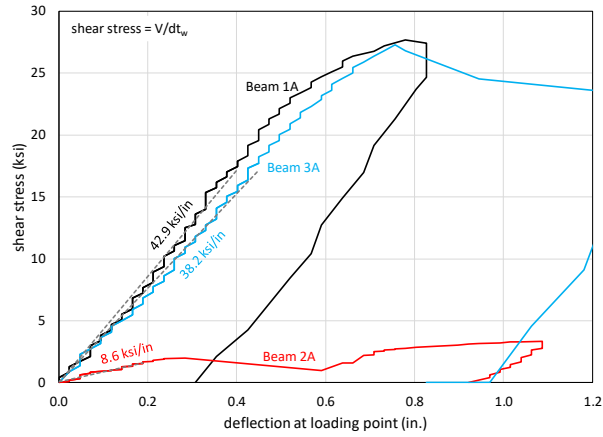
A summary of key parameters of all End A tests is provided in Table 19. The initial stiffness of the beam, K is determined from a straight line fit of the demonstrably linear portion of the shear-deflection curves. The deflection used is that under the load point (δ_I). This value is also reported

in terms of shear stress as k . The values of V_{max} and v_{max} are determined at the maximum shear force observed in the test. The shear stress at theoretical shear yield strain, “ v at $\gamma = 1900 \mu\epsilon$ ” is also reported as a basis of comparison between girders. Finally, because the beams were much stronger than initially intended, observation of girder yield at the point of application of load is also made. This latter phenomenon was fully supported by full depth bearing stiffeners and is not believed to have significantly affected the shear span or bearing behavior of interest in this study.

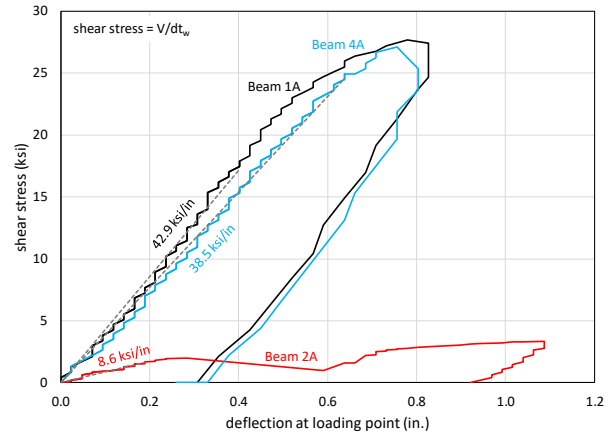
Figure 40 shows the applied shear stress (V/dt_w) versus deflection (δ_l) curves obtained for all specimens. Control Girders 1A and 2A are repeated on all plots and each plot shows one of 3A to 6A. The initial stiffness of all repaired girders is similar to that of the undamaged control girder. With the exception of 6A, the load resisting behavior and ultimate capacities were also similar. Without repair, all girders would exhibit a behavior similar to that shown for 2A. Repairs demonstrated in Girders 3, 4 and 5 effectively restored the capacity of the corrosion-damaged girder end regions.

Table 19 Summary of Key Parameters of Monotonic End A Tests

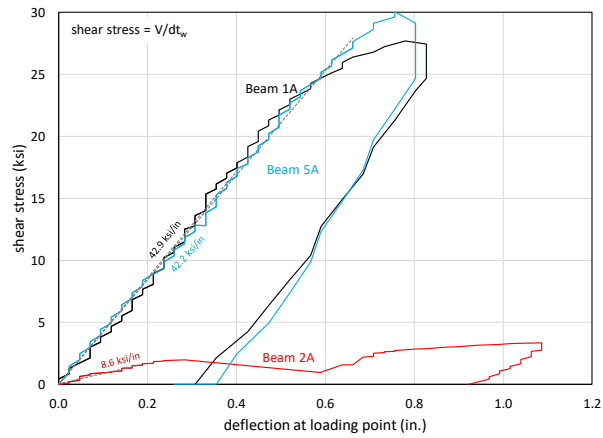
Girder		1A	2A	3A	4A	5A	6A
		undamaged control	corroded control	steel repair	UHPC repair	RC repair	GFRP repair
t_w	in	0.326	0.324	0.305	0.317	0.281	0.288
$K = V/\delta_I$	k/in	332	65	280	285	280	292
$k = v/\delta_I$	ksi/in	42.9	8.6	38.2	38.5	42.2	41.5
V_{max}	kips	213.1	15.1	196.6	202.9	199.3	81.8
$v_{max} = V_{max}/dt_w$	ksi	27.7	2.0	27.3	27.1	30.1	11.6
δ_I at V_{max}	in.	0.78	0.28	0.71	0.76	0.76	0.28
failure at V_{max}		web buckling	bearing	web buckling	web buckling	concrete crushing at bearing	catastrophic GFRP debonding
γ_{max} at V_{max}	$\mu\epsilon$	2730	256	3946	4852	2158	1174
v at $\epsilon = \epsilon_y = 1900 \mu\epsilon$	ksi	27.7	no yield	18.2	26.2	no yield	no yield
v at $\gamma = 1900 \mu\epsilon$	ksi	20.0	-	18.2	21.9	27.6	-
V at initial yield at load point	kips	164 theoretical	no yield	147	not clearly observed	no yield; concrete contributes to bearing	no yield



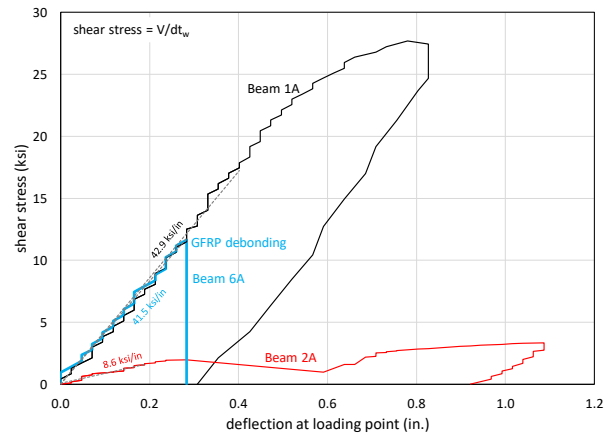
a) Girders 1A, 2A and 3A (bolted steel)



b) Girders 1A, 2A and 4A (UHPC)



c) Girders 1A, 2A and 5A (RC)



d) Girders 1A, 2A and 6A (GFRP)

Figure 40 Shear Stress versus Displacement Curves from Monotonic Tests

Maximum principal shear strains, γ_{max} and the angle of maximum shear, θ , are shown in Figure 41. Initiation of buckling was observed in Girders 1A, 3A and 4A. These girders had repair measures over only part of the shear span. The web region beyond the repair region was observed to buckle. The web of Girder 5A, on the other hand, was entirely encased in well confined concrete and no evidence of web buckling, despite an initial out of straightness, was observed. The concrete effectively braced the web against buckling. This is shown dramatically in Figure 46d, in which the initial distortion of the embedded web of 5A is shown at the end of testing (concrete was forcibly removed following testing to obtain this image). This significant degree of distortion did not affect the ultimate capacity of this girder end.

The orientation of maximum shear (Figure 41b) for all specimens (except 2A) is in the vicinity of 45° to 50° as assumed by Bernoulli beam theory. 2A exhibited a very steep angle since the stress trajectories had to redistribute to accommodate the loss of bearing capacity. In 2A, bearing capacity of the beam end was provided mostly by flexure of the bottom flange.

The steel web of Girder 5A resisted a smaller portion of the shear since it was entirely encased in concrete which was therefore able to resist most of the shear stress. Thus, the shear stress shown in Figure 46a is not that carried by the web but that which would be carried by the web in the absence of the surrounding concrete. A discussion of the composite behavior of Girder 5 is provided in Section 5.5.

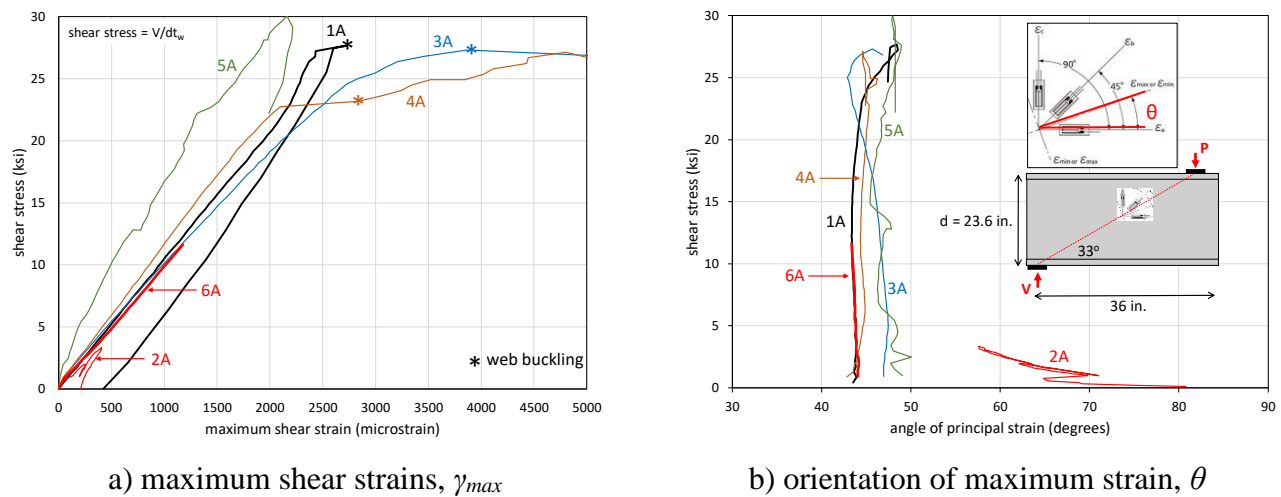
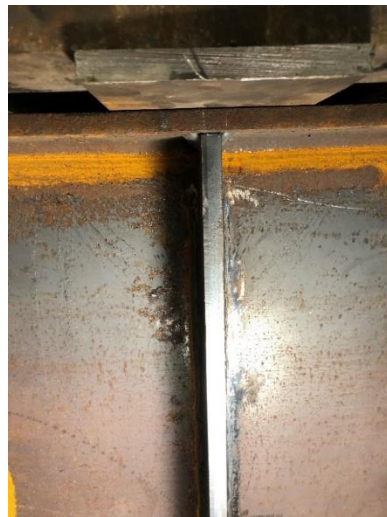


Figure 41 Principal Shear Strains and Orientation of Maximum Shear for Monotonic End A Tests

5.2.1 Girder End 1A

Undamaged control Girder 1A behaved essentially as predicted, achieving a maximum shear capacity $V = 213$ kips ($v = 27.7$ ksi). This capacity corresponded to web yield beneath the applied load (260 kips applied over a 5 in. length of flange); this is shown in Figure 42. The predicted capacity based on this limit state was an applied load of 256 kips or shear of 210 kips.

Nonetheless, strain data (Figure 41) indicated that web buckling had also just initiated at this capacity.



a) yield lines expressed in mill scale under point of application of load



b) distortion of top flange associated with web yield under point of application of load

Figure 42 Girder 1A Following Testing

5.2.2 Girder End 2A

Unrepaired corroded Girder 2A exhibited little capacity, achieving a shear resistance of barely 7% of 1A, $V = 15.1$ kips ($v = 2.0$ ksi). In this girder, shown in Figure 43, the bearing capacity was provided almost entirely by the bottom flange bending about its horizontal axis. The web collapsed and some residual capacity was observed at displacements exceeding 0.75 in. as the hole in the web physically closed and began to bear again on the flange (Figures 43b and c).



a) bearing region during testing



b) residual distortion of bearing region after testing



c) complete collapse of the web

Figure 43 Girder 2A During and After Testing

5.2.3 Girder End 3A

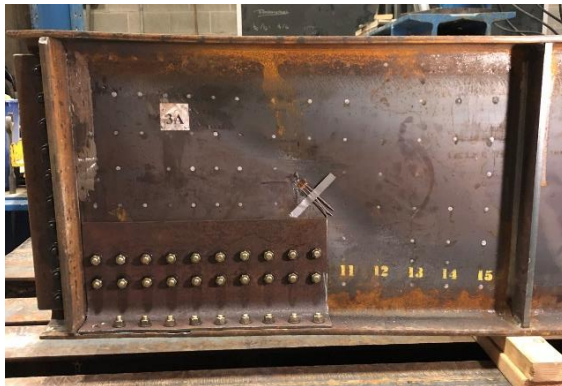
Girder 3A demonstrated a conventional bolted steel repair. The girder capacity was effectively restored to approximately that of 1A: $V = 197$ kips ($v = 27.3$ ksi). 3A exhibited very clear web buckling in the unstrengthened region of shear span as shown in Figure 44. Following testing, the bolted stiffeners were removed (Figure 44d); no web distortion or collapse was observed although a few of the bolt holes appear to show evidence of bolt-bearing distortion (“ploughing”).



a) bearing region following testing



b) web distortion following testing and removal of stiffeners



c) web buckling



d) bearing region following testing and removal of stiffeners

Figure 44 Girder 3A Following Testing

5.2.4 Girder End 4A

UHPC-encased repair 4A achieved a capacity of $V = 203$ kips ($v = 27.1$ ksi), effectively restoring the capacity of 1A. Failure was predicated by buckling of the unencased portion of the web. As seen in Figure 45 there was essentially no discernible damage to the UHPC itself. Separation between the top and bottom flanges of the girder and the UHPC was noted at a shear of 42.5 kips, approximately 21% of the ultimate capacity (Figure 45b). This crack once formed

did not appear to vary through the remainder of the test. The presence of the crack at relatively low (service) load levels indicates the potential for crevice corrosion at these interfaces. The assumed strains at which this crack appeared suggests that it would not be mitigated by providing shear connectors along the flange.

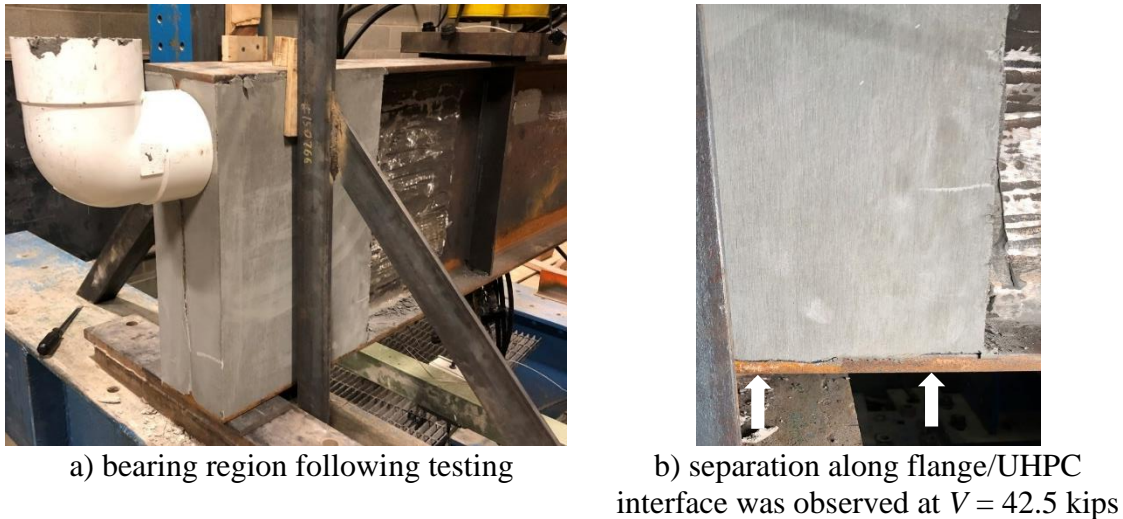


Figure 45 Girder 4A Following Testing

5.2.5 Girder 5A

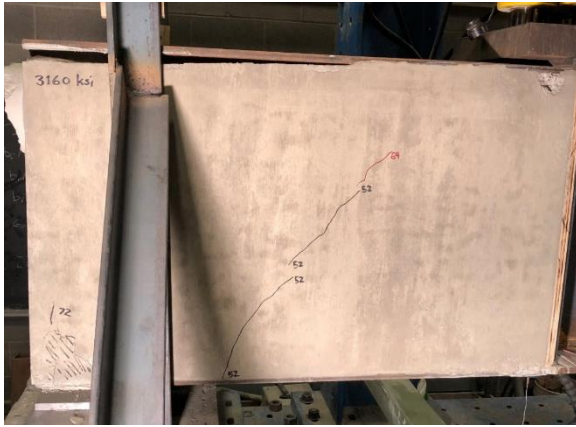
The reinforced concrete encased repair 5A extended along the entire shear span and effectively mitigated web instability. Despite the quite low concrete strength (3.2 ksi) the girder capacity, $V = 199$ kips ($v = 30.1$ ksi), marginally exceeded that of 1A. The web thickness of 5A was only 86% of that of 1A while the maximum shear stress was 109% that of 1A.

The concrete encasement was well confined and appeared to behave as a concrete beam in shear. Concrete cracking initiated at a shear of $V = 42.6$ kips (Figure 46a). The concrete crack pattern developed as the test progressed (Figure 46b) although all crack widths remained well controlled and the concrete remained sound.

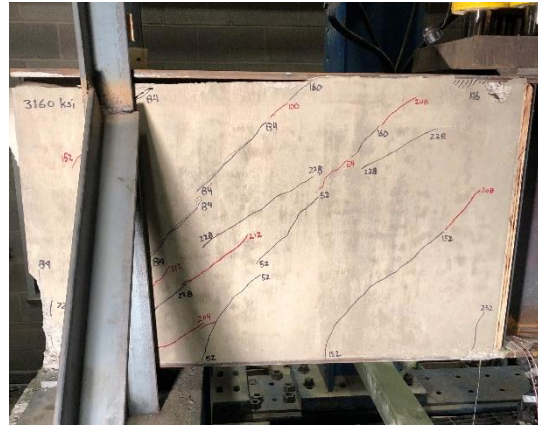
Cracking and minor spalling was observed at the back of the bearing region from a shear of $V = 59$ kips. Concrete crushing at the bearing represented the ultimate failure of this Girder end (Figure 46c). The low concrete strength clearly contributed to this behavior. The horizontal reinforcement provided above the bearing appeared to control spalling to some extent although due to the corrosion damage, this reinforcement is difficult to anchor in the bearing region, right where it is needed most.

As the bearing began to crush, the cracking along the shear span became flatter. Initial cracking was observed at an angle of about 45° (Figure 46a) while later cracks transitioned to an angle of about 30° from horizontal (Figure 46b).

Figure 46d shows the web distortion inside the concrete. This distortion is that around which the concrete was placed; the distortion was unaffected during testing. Thus, the confined concrete effectively restrained the damaged web. Shear strain data (Figure 41) indicates that this web did not resist as great a proportion of the load as in other specimens with load sharing between the concrete and steel web. This observation is supported by the nature of the concrete cracking and is discussed further in Section 5.5.



a) initial cracking at $V = 42.6$ kips;
crack angle $\approx 45^\circ$



b) final crack pattern after completion of
tests; late-forming crack angle $\approx 30^\circ$



c) concrete bearing failure



d) encased concrete mitigated further
distortion of web (distortion seen was
present at concrete placement); concrete
intentionally removed to show web

Figure 46 Girder 5A During and Following Testing

5.2.6 Girder End 6A

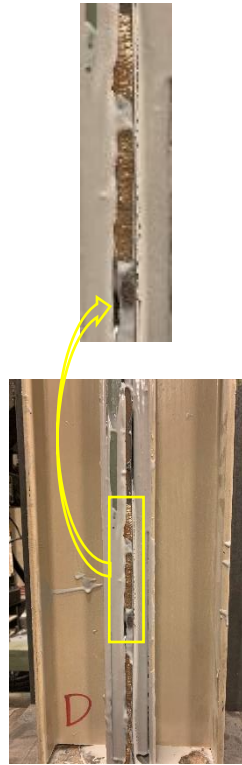
Girder 6A initially behaved quite well, matching the stiffness of Girder 1 and the other repaired girders. At $V = 81.8$ kips ($v = 11.6$ ksi), about 40% of the capacity of Girder 1, Girder 6A exhibited catastrophic debonding of the GFRP plate. Immediately upon debonding, the now-overloaded web collapsed at the bearing as seen in Figure 47c. Although the final failure was quite

brittle, debonding was progressive. Some evidence (popping sounds) occurred at $V = 42.5$ kips and progressed until the test ended. A delamination crack was evident above the bearing region at $V = 68.7$ kips (Figure 47b).

Bond between the steel and GFRP plate was quite good on the smooth web surface (Figure 52f) while evidence of voids in the adhesive line are evident on the ‘corroded’ side which had greater amplitude of small flaws. In both cases, debonding occurred primarily as an adhesive failure at the GFRP plate interface (Figures 47e and f) although some evidence of cohesive failure penetrating the plate was observed (Figure 47d). The bond of the GFRP W3 stiffener to the GFRP plate was excellent. Because of the poor brittle performance of 6A, fatigue conditioning and testing of 6B was not undertaken.



a) bearing at beginning of test



b) initial debonding at $V = 68.7$ kips



after removal of GFRP



c) catastrophic debonding at $V = 81.8$ kips



d) debonded surface of W3 and GFRP plate



e) debonding of West side GFRP plate (affixed to 'corroded' steel)



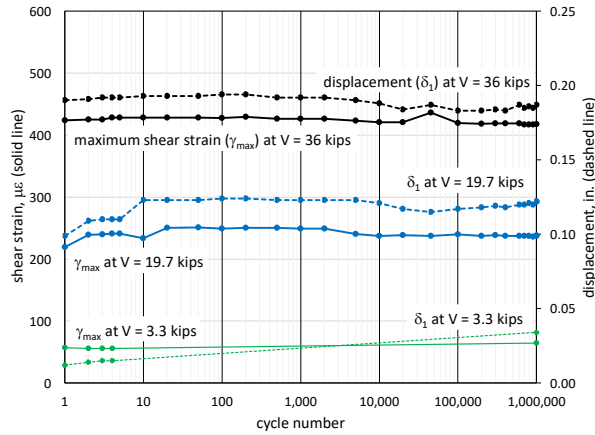
f) debonding of East side GFRP plate (affixed to smooth steel)

Figure 47 Girder 6A Following Testing

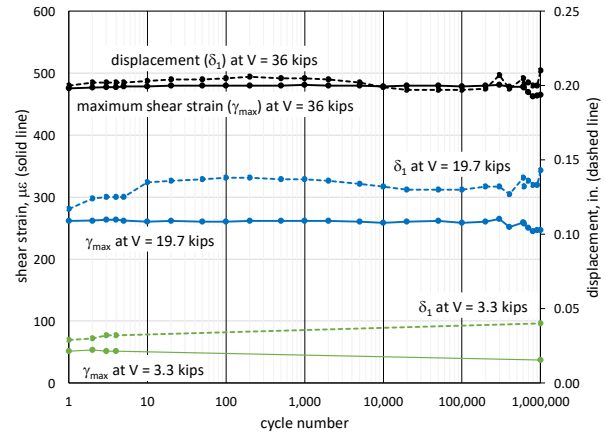
5.3 Fatigue Conditioning (Girder End B)

Fatigue conditioning was undertaken for Girders 3, 4 and 5. Because of the poor brittle performance of 6A, fatigue conditioning of 6B was not undertaken. Girder 1 has no damage and should not be expected to exhibit any deterioration under the fatigue conditioning protocol and was therefore not tested. Girder 2 exhibited a static capacity below the fatigue loads and was therefore also not tested. Fatigue conditioning to 1 million cycles was not expected to result in any significant deterioration of the specimens and very little was observed.

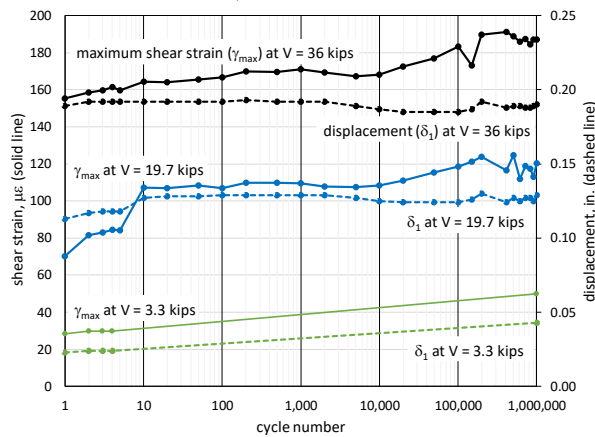
In order to quantify deterioration, the history of the maximum shear strain, γ_{max} and displacement of the load point, δ_l with cycling for all specimens is reported in Figure 48. Data is reported at the peak shear force, $V = 36$ kips ($P = 44$ kips) and mean shear, $V = 19.7$ kips ($P = 24$ kips). Only initial and final cycle data is reported at the minimum shear, $V = 3.3$ kips ($P = 4$ kips). Any deterioration would result in an increase in these values as the apparent stiffness of the girder fell. Although displacement data is shown in Figure 48, this is not directly comparable with that reported in the monotonic tests. Displacement during fatigue conditioning is determined from the actuator LVDT and therefore includes compliance of the actuator and test frame.



a) Girder 3B



b) Girder 4B



c) Girder 5B (note different scale for strain axis)

Figure 48 Shear Strain and Displacement Histories during Fatigue Conditioning

5.3.1 Girder End 3B

The source of the 0.013 in. increase at $V = 19.7$ kips between the fifth and tenth cycle (Figure 48a) is unknown although may be related to the test protocol. The first five individual cycles were conducted “manually” at a rate on the order of 0.1 Hz whereas, beginning with cycle 6 cycling at 1.2 Hz was initiated. The increase was evident in other specimens as well. Since the step is not seen at $V = 36$ kips or in the strain data, this is not interpreted as any damage to the girder. Peak shear strains at $V = 36$ kips remained in the range $417 \mu\epsilon$ to $436 \mu\epsilon$ whereas $\gamma_{max} = 457$

$\mu\epsilon$ at $V = 36$ kips in End A. No distress in Girder 3B was evident following one million cycles of fatigue conditioning.

5.3.2 Girder End 4B

Separation of the UHPC and bottom and top flanges, similar to what was observed in the static testing, was evident from the initial cycle although this was not observed to progress through one million cycles of fatigue conditioning. Small variations in measured displacements (variation less than 0.02 in.) and strains (variation less than $20 \mu\epsilon$) for $N > 200,000$ was observed. These are not interpreted as representing any significant damage initiation or progression. Peak shear strains at $V = 36$ kips remained in the range $462 \mu\epsilon$ to $481 \mu\epsilon$ whereas $\gamma_{max} = 397 \mu\epsilon$ at $V = 36$ kips in End A. Recognizing that the steel web thickness of 4B was only 84% of that of 4A, these strains are essentially equivalent.

5.3.3 Girder End 5B

No cracking of the reinforced concrete was observed in initial cycles. Distress in the form of concrete cracks (see Figure 49) was first observed at $N \approx 49,000$ cycles. The cracking propagated somewhat through $N = 200,000$ cycles. After $N = 200,000$ cycles, apart from a short crack extension observed in one crack at $N \approx 340,000$ cycles, no additional distress was observed through $N = 1,000,000$ cycles. Such fatigue damage progression in reinforced concrete is relatively typical (ACI 215R-22). All cracks were ‘hairline’ and only observable when the beam was subject to the maximum shear, $V = 36$ kips.

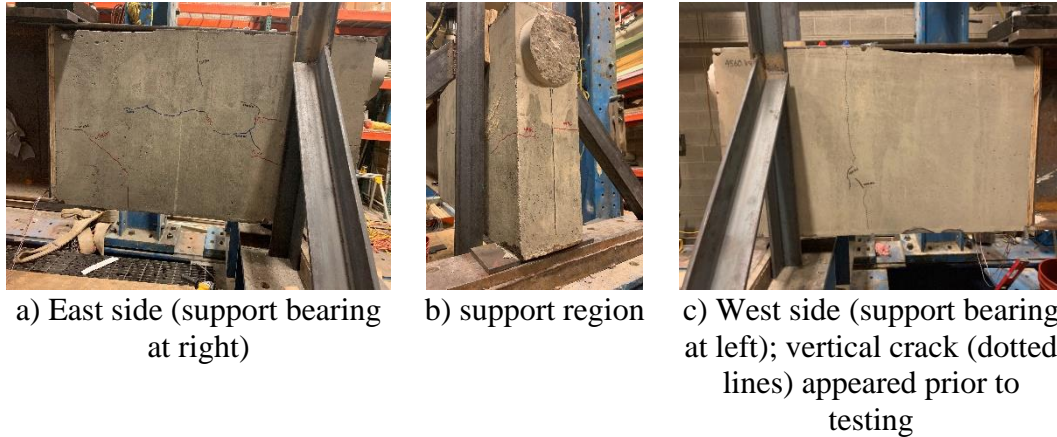


Figure 49 Cracking Observed during Fatigue Conditioning of Girder 5B

Unlike Girders 3B and 4B, a steady increase in web strain was observed with fatigue conditioning (Figure 49c). Due to the concrete encasing the entire shear span, and sharing in the shear resistance, the steel web strains in Girder 5 are lower than those in the other girders. The peak shear strain at $V = 36$ kips in End A was $206 \mu\epsilon$. The peak shear strain during fatigue conditioning progressed from $155 \mu\epsilon$ at $N = 1$ to $191 \mu\epsilon$ at $N \approx 400,000$, falling marginally to $187 \mu\epsilon$ at $N = 1,000,000$. A similar progression is seen at $V = 19.7$ kips and $V = 3.3$ kips. This progression was not accompanied by a meaningful change in displacement and therefore can be attributed to a minor degradation of the composite behavior of the reinforced concrete encasement resulting in shear being redistributed back into the steel web.

5.4 Girder End B Post Fatigue Conditioning Monotonic Test Results

These tests are the same as the End A tests except that they are conducted following one million cycles of fatigue conditioning. A summary of key parameters of all End B tests is provided in Table 20; the End A data is repeated from Table 19 for clarity. Figure 55 shows the applied shear stress (V/dt_w) versus deflection (δ_l) curves obtained for all specimens. Control Girder 1A is

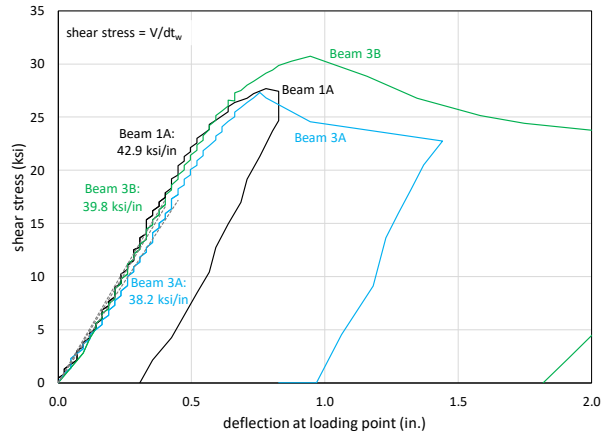
repeated on all plots and each plot shows one set of comparable girder ends. Figure 51 shows a comparison of the maximum shear strains for each fatigue conditioned girder.

Each of the End B tests performed essentially the same as the End A tests. Because the End B tests were the last conducted with each specimen, these could be ‘pushed’ to larger deformations than the End A tests. Each of the End B tests exhibited an initially stiffer response and resisted greater capacity than the comparable End A. This may have resulted from the ‘shakedown’ effect from the fatigue conditioning. This result confirms that the fatigue conditioning protocol used had no deleterious effect on the girders’ performance.

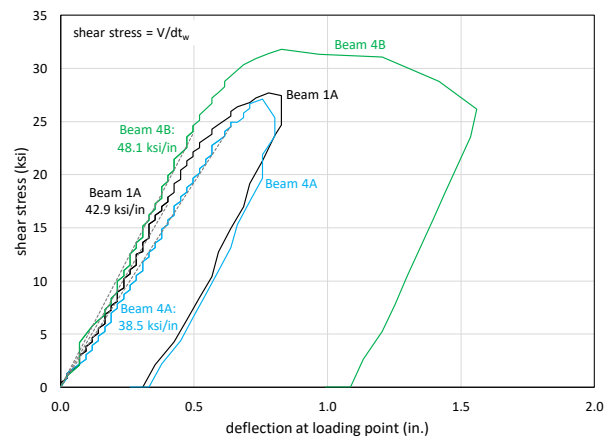
When interpreting results, it should be noted that strain data is generally unreliable at gage readings exceeding 10,000 $\mu\epsilon$ (0.1%) and that the gage (embedded in concrete) of Girder 5B failed during testing at essentially the peak load attained.

Table 20 Summary of Key Parameters of Monotonic End B Tests

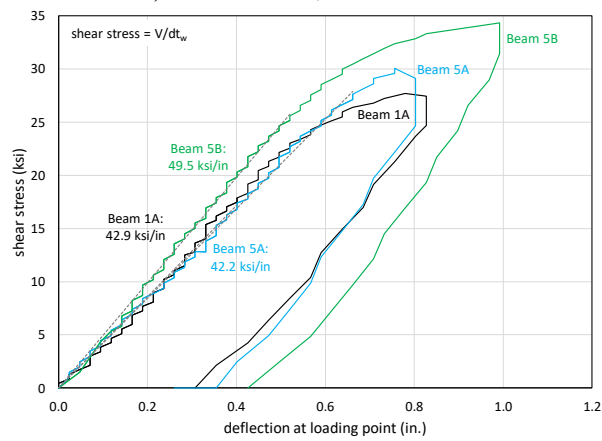
Girder		3A	3B	4A	4B	5A	5B
		steel repair		UHPC repair		RC repair	
t_w	in	0.305	0.298	0.317	0.265	0.281	0.287
f_c at time of test	psi	-	-	21,400	22,700	3160	4920
$K = V/\delta_I$	k/in	280	297	285	301	280	335
$k = v/\delta_I$	ksi/in	38.2	41.3	38.5	48.1	42.2	49.5
V_{max}	kips	196.6	216.0	202.9	199.0	199.3	232.7
$v_{max} = V_{max}/dt_w$	ksi	27.3	30.7	27.1	31.8	30.1	34.4
δ_I at V_{max}	in.	0.71	0.87	0.76	0.83	0.76	0.99
failure at V_{max}		web buckling	stiffener bearing and web buckling	web buckling	web buckling	concrete crushing at bearing	web yield
γ_{max} at V_{max}	$\mu\epsilon$	3946	>10,000	4852	>10,000	2158	4008
v at $\epsilon = \epsilon_y = 1900 \mu\epsilon$	ksi	18.2	28.0	26.2	27.7	no yield	34.4
v at $\gamma = 1900 \mu\epsilon$	ksi	18.2	21.9	21.9	17.8	27.6	27.5
V at initial yield at load point	kips	147	not clearly observed	not clearly observed	not clearly observed	no yield	no yield



a) Girders 1A, 3A and 3B

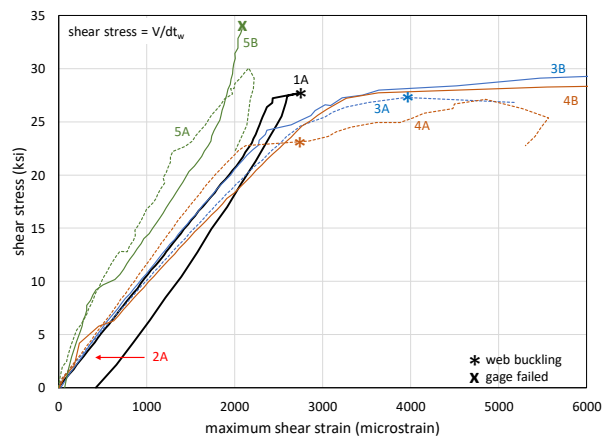


b) Girders 1A, 4A and 4B

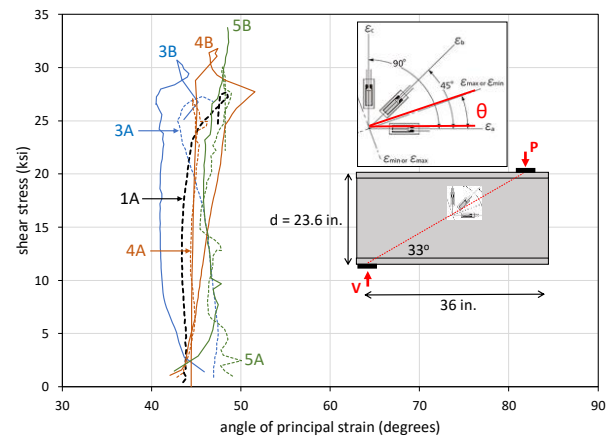


c) Girders 1A, 5A and 5B

Figure 50 Shear Stress versus Displacement Curves from Monotonic Tests



a) maximum shear strains, γ_{max}



b) orientation of maximum strain, θ

Figure 51 Principal Shear Strains and Orientation of Maximum Shear for Monotonic Tests

5.4.1 Girder 3B

Girder End 3B behaved in a manner comparable to End 3A, achieving a marginally greater ultimate capacity of $V = 216$ kips. Web buckling dominated ultimate behavior (Figure 52a) although it was also noted that the bearing stiffener exhibited yield (Figure 52b). The AASHTO-prescribed (Equation 1-12) design capacity of the fitted end of the bearing corresponds to $V = 1.4A_{pn}F_y = 140$ kips whereas the nominal capacity is best estimated to be $V = 1.8A_{pn}F_y = 180$ kips (ANSI/AISC 360 2016 §J.7(a)).

During testing of End 3B, some instances of ‘bolt banging’ were heard beginning at $V = 147$ kips. Like Girder End 3A, upon removal of the repair plates, a few holes along the bearing stiffener showed evidence of bearing induced distortion (“ploughing”). No evidence of fatigue-induced damage (fretting, fraying, etc.) at bolted interfaces was apparent and the faying surfaces had clearly remained in full frictional contact throughout fatigue conditioning ($V < 36$ kips).

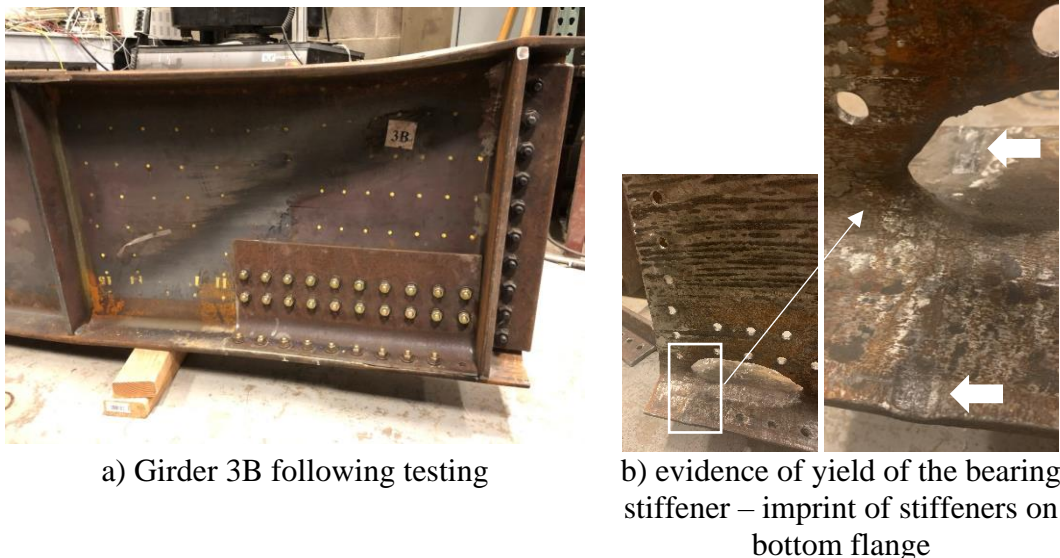


Figure 52 Girder 5B Following Testing

5.4.2 Girder End 4B

Girder End 4B achieved a capacity of $V = 199$ kips, comparable to that of End A and the ultimate behavior was controlled by buckling of the unencased portion of the web (Figure 53). Flange distortion at the ultimate load indicates that the UHPC effectively created a 23 in. shear panel between the load point and the edge of the UHPC. There was no apparent distress in the UHPC apart from minor separation along the flanges as also observed for End A.



Figure 53 Girder 4B Following Testing Showing Well Controlled Panel Buckling

5.4.3 Girder End 5B

The capacity achieved by Girder End 5B was $V = 233$ kips, exceeding that of 5A (199 kips) despite the web thickness being essentially the same. The concrete strength in End 5B was greater resulting in an improved overall response. New cracks appeared at a $V = 72$ kips and the cracks that formed during fatigue conditioning opened with increased loading. Like End 5A, the angle of the cracks was approximately 45° at lower loads and flattened to about 30° as the applied shear increased (see Figure 54).

The concrete remained in good shape and effectively resisted buckling throughout the test. Following testing, concrete was removed, and the web was found to have remained entirely plane, as expected.

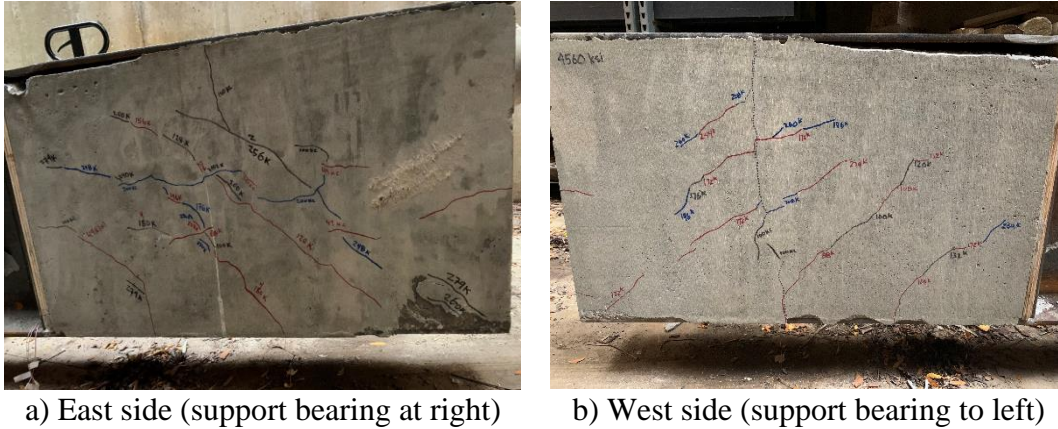


Figure 54 Girder 5B Following Testing

5.5 Composite Behavior of Reinforced Concrete Encased Girder 5

The analysis described in this section is approximate, requiring a fitting curve for the section shear stress ($v = V/dt_w$) versus measured steel web shear strain (τ_{max}) to be established. A cubic relationship having excellent fit characteristics ($R^2 > 0.99$ in all cases) was used, although this ‘forces’ the proportion shown to also be cubic. The fitting curves determined from experimental data are as follows, with τ_{max} expressed in microstrain.

Girder 1A:	$\tau_{max} = -0.047v^3 + 1.404v^2 + 86.48v$	Equation 5-1
------------	--	---------------------

Girder 5A:	$\tau_{max} = -0.106v^3 + 1.469v^2 + 36.99v$	Equation 5-2
------------	--	---------------------

Girder 5B:	$\tau_{max} = -0.102v^3 + 4.483v^2 + 24.73v$	Equation 5-3
------------	--	---------------------

In all girders except Girder 5, the strain recorded from the web captures 100% of the shear resisted at the location of the strain gage located at the center of the shear span. In Girder 5, the web is encased by reinforced concrete at this location and therefore shear is expected to be resisted in a composite manner. Using the web stress strain behavior of Girder 1A as a benchmark, the proportion of total shear resisted by the steel girder web can be estimated as the ratio of steel web shear strain in Girder 5 to that observed in Girder 1 (i.e, the ratios of Eq. 5-2/Eq. 5-1 and Eq. 5-3/Eq. 5-1 for 5A and 5B, respectively).

Based on a simple transformed sections analysis, the steel webs are expected to resist 35% and 31% of the total applied shear for Ends 5A and 5B, respectively. As seen in Figure 60, the initial proportion of shear resisted by the web of End 5A is 44% and that for 5B is 33%. During fatigue conditioning of End 5B, the proportion began at 30% and progressed to 38% over 1 million cycles. In both Ends 5A and 5B, as the load increases, a greater proportion of shear is resisted by the steel web. This indicates that there is a deterioration of the composite behavior of the embedded steel web.

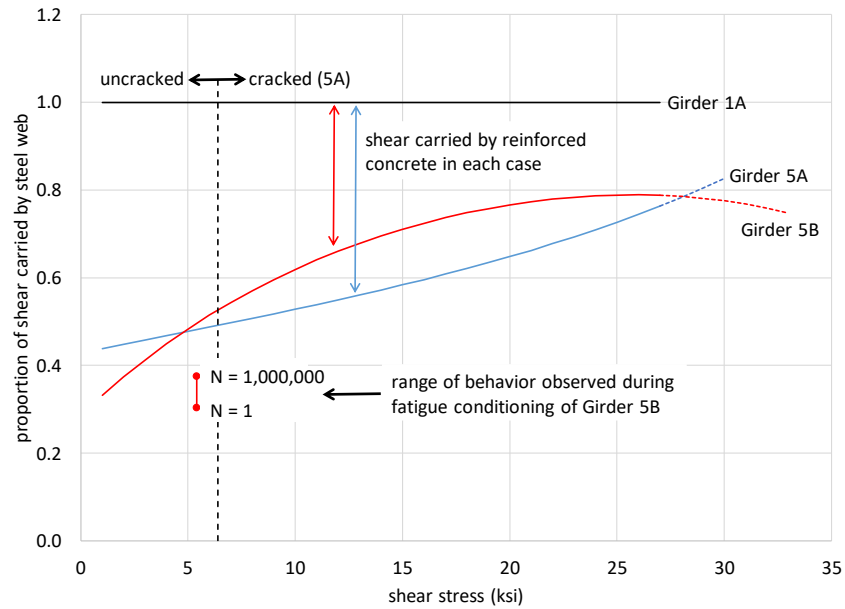


Figure 55 Proportion of Shear Resisted by Steel Web in Girder 5

5.6 Interpretation of Test Results and Correlation with *In Situ* Conditions

All of the experimental results must be interpreted in the context of their load history. None of the beams were subject to load during the repair process. This situation is similar to that in the field in which a member being repaired is entirely relieved of load through jacking (or similar). This is the condition necessary during a bearing replacement, for instance. Thus all tests begin at a true ‘zero load’ condition in which the repair and substrate girder are behaving in composite manner immediately upon application of load. All strain data presented are also ‘zeroed’: residual strains in the member are not captured. In the field, even if the load is entirely relieved, residual deformations/strains may be present.

6.0 Finite Element Modeling

As described in Chapter 1, a number of studies have reported finite element (FE) simulations of the behavior of girders subject to beam end corrosion. All studies report quasi-static nonlinear analyses and focus on web buckling behavior. In general, the models reported in the literature provide details (or restraints/constraints) that will mitigate local bearing effects. The latter, however, are critical to corroded end region behavior, resulting in most extant studies having little relevance to the present study. Gerasimidis and Brena (2019), however, report an extensive validation and parametric study focused on local effects, neglecting buckling. The development and details of this model are most relevant to the present study. The modeling reported here leverages the extensive validation provided by Gerasimidis and Brena with the following adopted for this study:

- Quasi-static analysis using ABAQUS. ABAQUS is well suited to modeling repair materials. In this study, ABAQUS 2020 (version 6.22) is used.
- General purpose shell elements (S4R) having thickness based on corrosion mapping and 100% section loss modeled by removing elements, not setting the thickness = 0. Most previous studies take this approach.
- Mesh size in bearing region equal to 0.5 in. transitioning to 2 in. in the span. Gerasimidis and Brena report a convergence study having these recommendations for similar beam dimensions and corrosion damage.
- ‘Hard contact’ interaction in normal direction permitting holes/gaps to close and transmit load upon doing so.

- ‘Softened contact’ in the normal direction at bearings. Gerasimidis and Brena calibrate a stiffness of 20 kips/in for this contact stiffness.
- Friction coefficient in the transverse direction at bearings equal to 0.74. Gerasimidis and Brena recommend this value based on experimental validation and note that model results are not sensitive to this parameter.

6.1 Finite Element Model Parameters

6.1.1 Modeling Steel Girders

All steel elements are ABAQUS S4R elements. S4R elements are 4-node general-purpose quadrilateral shell elements having reduced integration (one point) with hourglass control. These elements are conventional stress/displacement elements and are commonly used for steel sections. Uniform 0.5 in. mesh size is applied to the web and flanges at the bearing end of the girder. Mesh size is increased to 2 in. away from the end region as seen in Figure 56a. This mesh generation allows detailed modeling in the damaged region in order to capture local response while reducing computational time.

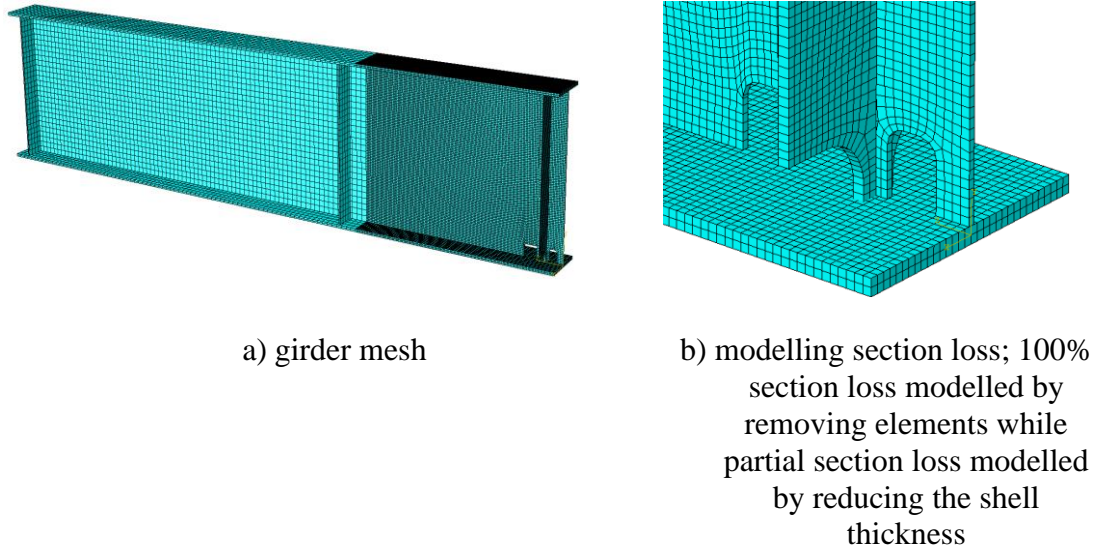


Figure 56 Mesh Geometry

6.1.2 Modeling Section Loss

Section loss was modeled as shown in Figure 56b. Partial section loss is achieved by reducing the S4R shell thickness. In regions of 100% section loss the shell elements were removed altogether.

6.1.3 Steel Material Properties

For the test specimens, measured yield strength of the girders was $F_y = 57.5$ ksi, and tensile strength was $F_u = 77.5$ ksi (see Section 4.3.2). For the 54" deep archetypal girders, existing plans for Bridge D indicate that ASTM A36 steel was used. For benchmark modeling, yield and tensile strength are assumed to be $F_y = 36$ ksi and $F_u = 58$ ksi, respectively. The modulus of elasticity is taken as $E = 29,000$ ksi.

For an isotropic material exhibiting ductile behavior, ABAQUS requires the true stress-strain relationship (rather than engineering stress-strain) as input. This is a monotonically

increasing function, given by Equations 6-1 and 6-2, over the entire strain range and is valid only to the ultimate tensile stress.

$$\text{for } \sigma_{engineering} \leq \sigma_u \quad \sigma_{true} = \sigma_{engineering} (1 + \epsilon_{engineering}) \quad \text{Equation 6-1}$$

$$\epsilon_{true} = \ln (1 + \epsilon_{engineering}) \quad \text{Equation 6-2}$$

To model plasticity in ABAQUS, the true stress (Eq. 6-1) versus true plastic strain Equation 6-3 is required:

$$\epsilon_{true}^{plastic} = \ln (1 + \epsilon_{engineering}) - \sigma_{true}/E \quad \text{Equation 6-3}$$

With Equations 6-1 through 6-3, any experimentally determined steel stress strain relationship can be used. This will be required for model benchmarking with the experimental study. For modeling the 54” deep girders, a generic A36 Grade 36 stress-strain relationship is adopted as shown in Figure 57. A similar relationship using measured properties is adopted for modeling the test specimens. The same material model is also used for other steel components including concrete reinforcing bars.

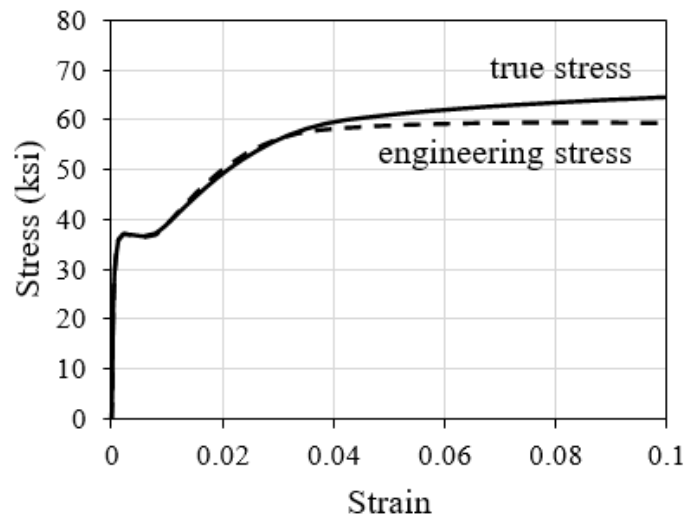


Figure 57 Engineering (experimental) and True (ABAQUS) Stress Strain Relationship for ASTM A36 Steel

6.1.4 Concrete Material Properties

Concrete encasement, whether ultra-high-performance concrete (UHPC) or normal-strength concrete (NSC), is modelled using ABAQUS C3D8 elements. C3D8 elements are 8-node general purpose solid (brick) elements. These elements are conventional continuum stress/displacement elements and are commonly used for concrete.

6.1.5 Concrete Material Model

The ABAQUS ‘smeared crack’ concrete model is adopted.

"The smeared crack concrete model in ABAQUS provides a general capability for modeling concrete in all types of structures. As a ‘smeared’ model, it does not track individual ‘macro’ cracks. Constitutive calculations are performed independently at each integration point of the finite element model. The presence of cracks enters into these calculations by the way in which the cracks affect the stress and material stiffness associated with the integration point. Cracking is assumed to occur when the stress of the element reaches the ‘crack detection surface’ which is a linear relationship between the equivalent pressure stress and the von Mises equivalent deviatoric stress. As soon as the crack detection surface has been activated, the crack direction is taken to be the direction of that part of the maximum principal plastic strain. Following the crack detection, the crack affects the response of the model because a damage elasticity model is used" (ABAQUS 2011).

To implement a smeared crack model, nonlinear compression and tension constitutive models and a failure surface interaction are defined in the following sections.

6.1.5.1 Concrete Compression

The complete stress-strain curve for concrete under compression is derived using the experimentally verified numerical model proposed by Hsu and Hsu (1994). Shown in Figure 58a, this model can be used to develop the stress-strain relationship under uni-axial compression through $0.3\sigma_{cu}$ in the descending portion using only the maximum compressive strength, σ_{cu} . The model assumes linear behavior having stiffness E_c through $0.5\sigma_{cu}$ beyond which, the stress-strain relationship through $0.3\sigma_{cu}$ (at ε_d) is defined as:

$$\sigma_c = \left(\frac{\bar{\beta} \left(\frac{\varepsilon_c}{\varepsilon_o} \right)}{\bar{\beta} - 1 + \left(\frac{\varepsilon_c}{\varepsilon_o} \right)^{\bar{\beta}}} \right) \sigma_{cu} \quad \text{Equation 6-4}$$

Where, the parameter $\bar{\beta}$ which depends on the shape of the stress-strain diagram, is calculated as:

$$\bar{\beta} = \frac{1}{1 - \left[\frac{\sigma_{cu}}{\varepsilon_o E_0} \right]} \quad \text{Equation 6-5}$$

For the generic model, Hsu and Hsu prescribe the strain at peak stress as:

$$\varepsilon_o = 8.9 \times 10^{-5} \sigma_{cu} + 0.00211 \quad \text{Equation 6-6}$$

6.1.5.2 Concrete Tension

Tension stiffening is the ability of concrete to carry tension between cracks in reinforced concrete members and is known to control the deformation calculation particularly at serviceability stress levels (Bischoff 2003). The concrete tensile stress-strain model proposed by Nayal and Rasheed (2006), shown in Figure 58b, is integrated into ABAQUS. Like compression, this is essentially a two-parameter model, requiring cracking stress, σ_{to} and concrete elastic modulus. All

other control parameters for the tension stiffening stress-strain model are shown in Figure 58. The values reported previously in Table 6 are adopted; these are repeated here in Table 21 for clarity.

Table 21 Typical Properties of UHPC, HPC, and NSC

	UHPC	NSC
primary citation	Russell and Graybeal (2013)	AASHTO LRFD
density, ρ_c	150 to 156 pcf	≈ 145 pcf
compressive strength, σ_{cu}	20 to 30 ksi	4 to 8 ksi
direct tensile strength	$\sigma_{ct} \approx 0.25(\sigma_{cu})^{0.5}$	$\sigma_{ct} \approx 0.23(\sigma_{cu})^{0.5}$
elastic modulus	$E_c = 1460(\sigma_{cu})^{0.5}$	$E_c = 1820(\sigma_{cu})^{0.5}$

6.1.5.3 Failure Surface

The plane stress smeared crack concrete failure surface adopted in ABAQUS is that described by Kupfer and Gerstle (1973) and is shown in Figure 58c. Four failure ratios are required:

- The ratio of the ultimate biaxial compressive stress to the ultimate uniaxial compressive stress, σ_2/σ_{cu} ; the ABAQUS default value is $\sigma_2/\sigma_{cu} = 1.16$.
- The absolute value of the ratio of the uniaxial tensile stress at failure to the ultimate uniaxial compressive stress, σ_{ct}/σ_{cu} (see Table 21).
- The ratio of the magnitude of a principal component of plastic strain at ultimate stress in biaxial compression to the plastic strain at ultimate stress in uniaxial compression; the ABAQUS default value is 1.28.
- The ratio of the tensile principal stress at cracking in plane stress when the other principal stress is at the ultimate compressive value to the tensile cracking stress under uniaxial tension; the ABAQUS default value is 0.33.

6.1.5.4 Shear Retention

The ABAQUS smeared crack model also permits shear retention. That is the degree of shear capacity retained in the cracked concrete model. The ABAQUS default is full shear retention. This assumption typically has little impact on results and did not affect the behavior of the repairs modeled in this study.

The smeared crack model is well established for normal (NSC) and high-strength concretes (HSC). Less validation is available for UHPC. However, with the higher cracking stresses inherent in UHPC, no cracking was observed during testing, and the material will remain essentially elastic.

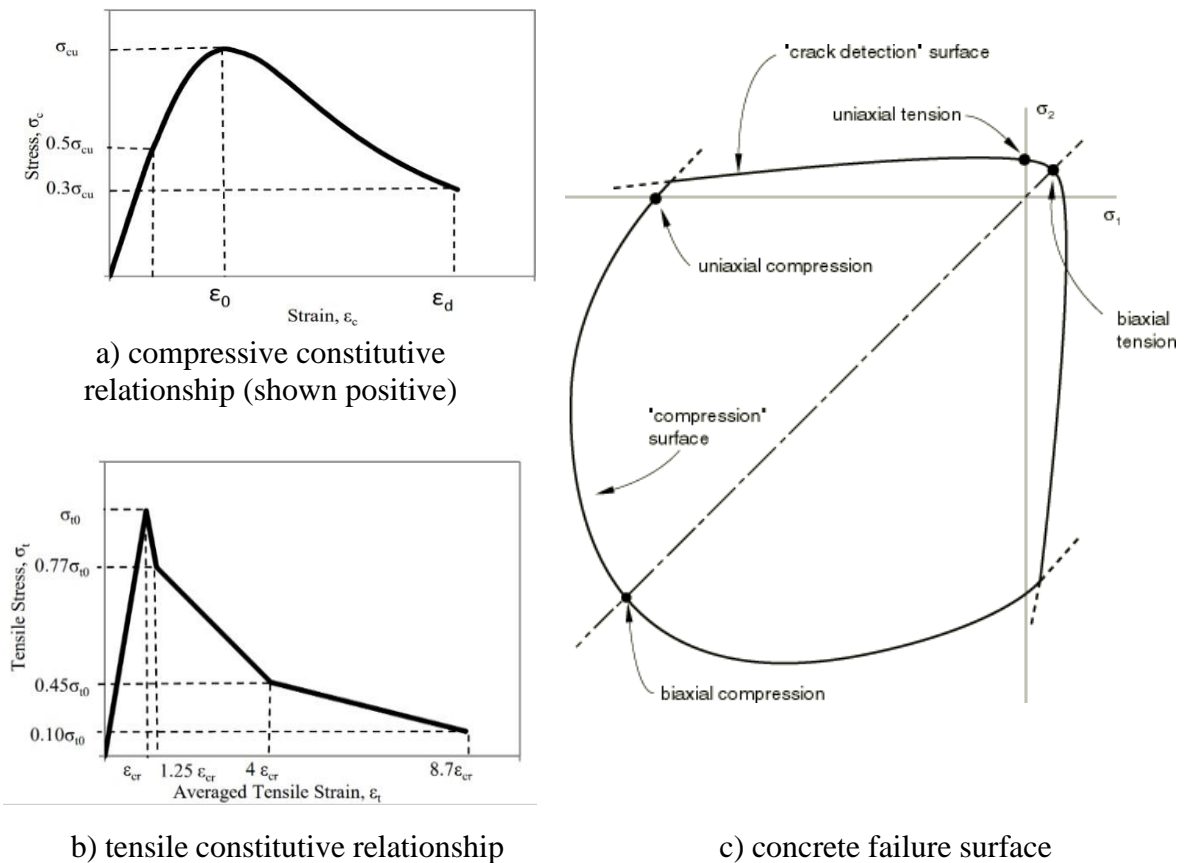


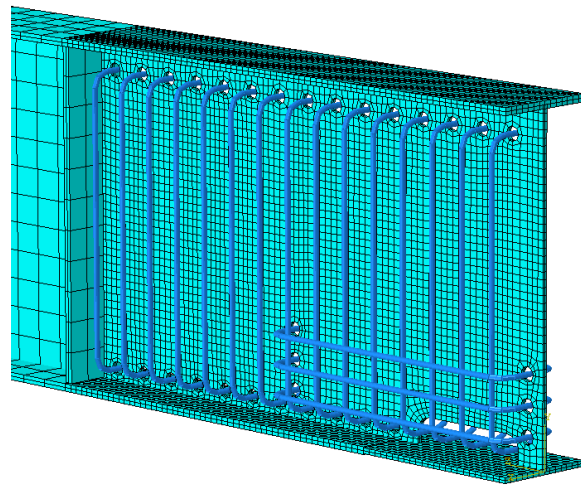
Figure 58 ABAQUS Smeared Crack Concrete Model

6.1.6 Internal Reinforcing Steel

ABAQUS supports the discrete modeling of internal reinforcing steel. T3D2, two node linear displacement truss, elements are used to model conventional 60 ksi steel reinforcement (Figure 59b). The reinforcement is embedded in the concrete using an embedment constraint. Initially this constraint is rigid, implying ‘perfect bond’ although it can be calibrated for experimentally determined reinforcing bar bond-slip relationships. Typically, perfect bond is a suitable assumption for uncracked concrete and remains reasonable for reinforcing bars stresses below yield.



a) Girder 5A



b) ABAQUS model with concrete hidden

Figure 59 Modeling Internal Reinforcing Steel of Girder 5A

6.1.7 Boundary Conditions

Boundary conditions, shown in Figure 60, are modeled to match the laboratory testing. The top flange is braced against lateral displacement, mimicking the lateral support of a composite deck slab.

6.1.7.1 Interaction with Bearing Plate

At each end of the simple span, the girder bearing is a 1 in. thick steel plate 5 in. long and wide enough to support the entire width of the bottom flange. Based on the recommendation of Gerasimidis and Brena (2019), the interaction between the bottom flange and bearing plate was defined using a linear ‘softened contact’ having $k = 20$ kip/in. in the normal direction. This factor was calibrated using experimental data and defines the contact pressure-over closure relationship at the contact interface. In the directions orthogonal to the interface surface, a contact friction coefficient equal to 0.74 was defined. Once again, Gerasimidis and Brena recommend this value based on experimental validation and note that model results are not sensitive to this parameter. The bottom surface of the bearing plate is fixed.

6.1.7.2 Applied Load

Static analysis is affected by applying a monotonic load ramp to a region of the top flange. Load is applied gradually until equilibrium cannot be found. The reaction at the girder end represents the shear capacity of the girder. The load is applied across the full width of the flange over a length of 5 in. centered on the bearing stiffener; i.e., the same condition as the bearing plates (Figure 60).

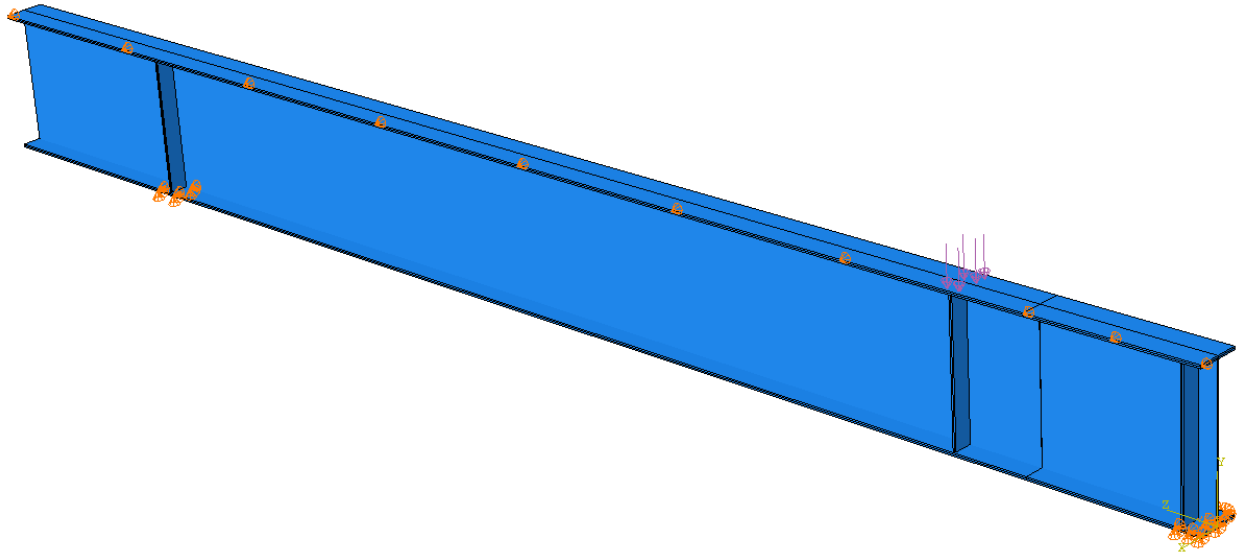


Figure 60 Numerical Model Boundary Conditions

6.1.8 Contact Interfaces around 100% Section Loss

‘Hard contact’ is defined at the edges of all holes. In this way, as the girder deforms and edges of holes come into contact, no over closure is permitted in the model.

6.1.9 Geometric Imperfections

ABAQUS can be used to determine the critical buckling (bifurcation) load using an Eigenvalue buckling analysis. This process is a linear perturbation procedure. An Eigenvalue buckling analysis is well established as a means of providing geometric imperfections or to investigate sensitivity to imperfections (Ellobody 2014). This approach is preferred over arbitrarily assigning imperfections based on design guides such as the American Welding Society (2015) or various recommendations found in literature (e.g., Latif and White 2021).

Buckling loads are calculated based on the original state of the structure, therefore, the girders were first modeled having no geometric imperfections when performing the Eigenvalue buckling analysis. Further, the same boundary conditions and loading was applied to the structure although the magnitude of the load is not relevant since it is scaled by the load multipliers that are predicted during the Eigenvalue buckling analysis. The lowest mode (mode 1) was used since this is the most likely failure mode of the girder. Following buckling analysis, the imperfections (Figure 61) were incorporated into the model and the monotonic load was applied.

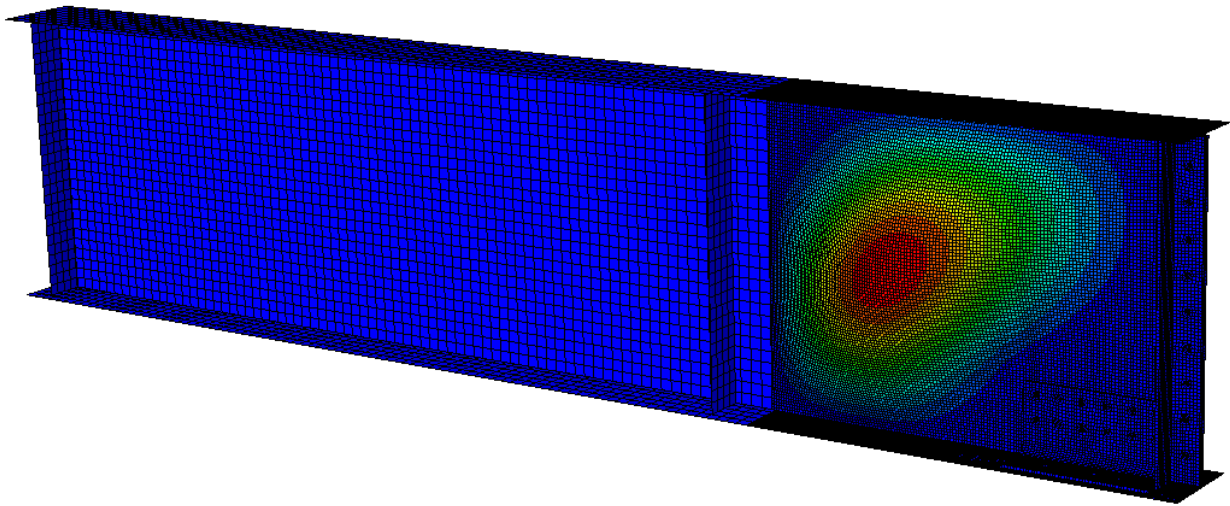


Figure 61 Girder Imperfections Based on Eigenvalue Buckling Analysis (deflection amplified)

6.2 Modeling Test Specimens

Test girders were modeled as they were tested. Measured material properties were used. Each model is summarized in the following sections and a summary of model results is provided in Table 22. The models are shown to be relatively robust, capturing limit states and experimental capacities well.

Table 22 Summary of Predicted Capacities for Test Specimen Modeling

model	FE-predicted		Laboratory testing	
	capacity (kips)	limit state	capacity (kips)	limit state
Girder 1A (undamaged steel)	215	web shear	213	web shear
Girder 2A (damaged steel without bearing stiffener)	16	web crippling	15.1	web crippling
Girder 3A (conventional steel repair)	200	tension field	197	tension field
Girder 4A (UHPC repair)	200	tension field	203	tension field
Girder 5A (reinforced concrete repair)	200	concrete crushing	199	concrete crushing

6.2.1 Girder 1A

Girder 1A was modeled as tested. The FE-predicted shear capacity was 215 kips in shear (determined as reaction at bearing) with failure by web shear and the testing resulted in 213 kips. As seen in Figure 62, tension field behavior was observed at maximum loading beyond 215 kips.

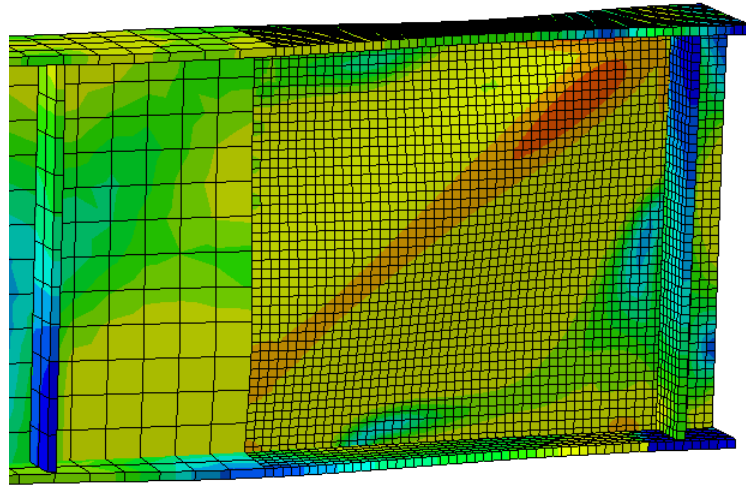
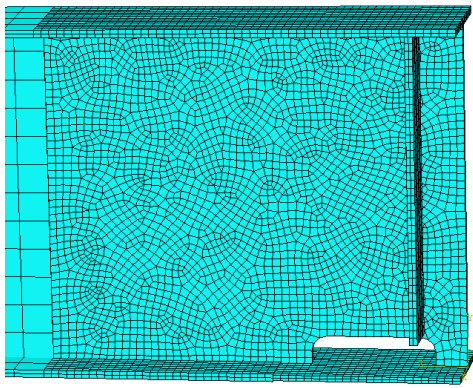


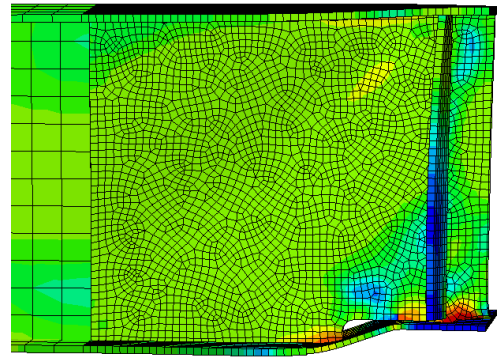
Figure 62 Girder 1A Loaded End Elevation with Maximum (von Mises) Stresses Plotted

6.2.2 Girder 2A

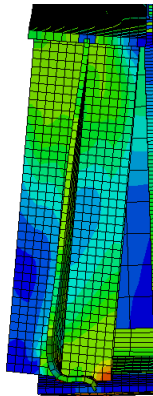
Girder 2A was modeled based on the archetypal damage. The FE-predicted capacity was 16 kips and failure, shown in Figure 63, was characterized as web yield, followed by crippling. Without the bearing stiffener present, the shear capacity observed during testing was 15.1 kips.



a) girder end prior to loading



b) girder end at maximum loading
(elevation view)



c) girder end at maximum loading
(end view)



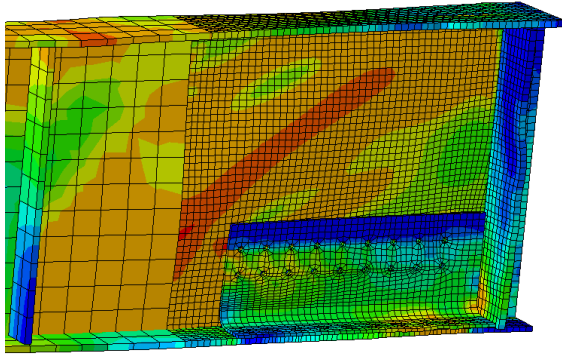
d) observed behavior following testing
(image mirrored)

Figure 63 Bearing Region Failure of Girder 2A

6.2.3 Girder 3A

Bolted steel repairs are modeled in the same manner as the substrate steel using actual geometry, S4R elements, and the same isotropic material model. Mesh size matches the substrate steel and bolts are modelled using tie constraints. Bolts holes were included in the model that matched the pattern of the test specimen. Normal compression is transferred through ‘hard contact’.

The FE-predicted shear capacity was 200 kips. As seen in Figure 64, tension field behavior was predicted. The testing resulted in a shear capacity of 197 kips.



a) girder end view with tension field action evident

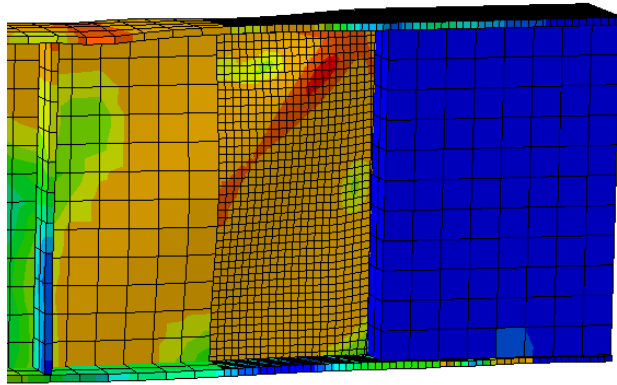


b) observed behaviour following testing (image mirrored)

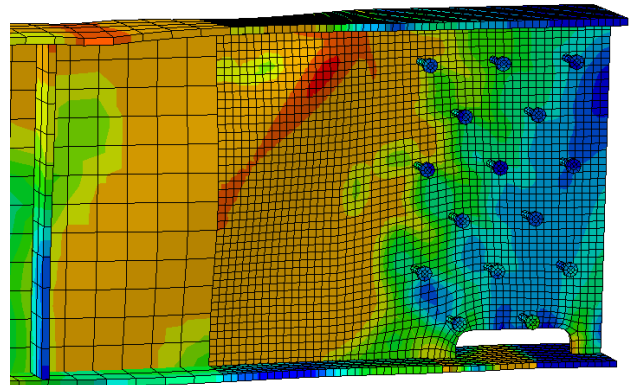
Figure 64 Bolted Steel Repair

6.2.4 Girder 4A

Girder 4A was modeled as tested. The FE-predicted shear capacity was 200 kips. As seen in Figure 65, tension field behavior was observed over the shortened shear panel between the UHPC encasement and bearing stiffener at the applied load. The testing resulted in a shear capacity of 203 kips.



a) failure of UHPC encasement repair with tension field action evident



b) bolted shear studs (UHPC hidden)

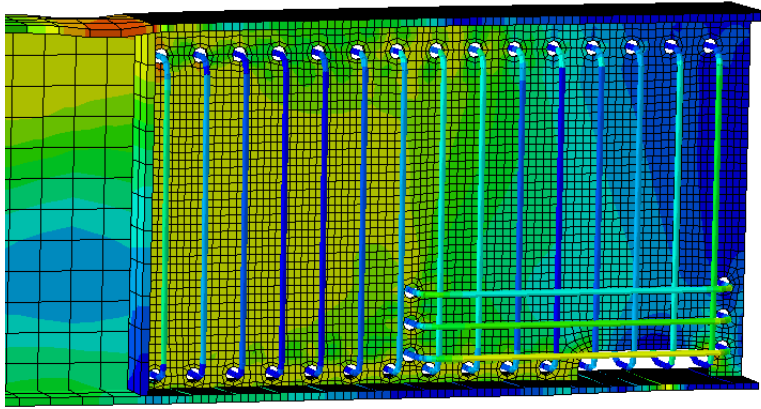


c) observed web buckling behaviour (image mirrored)

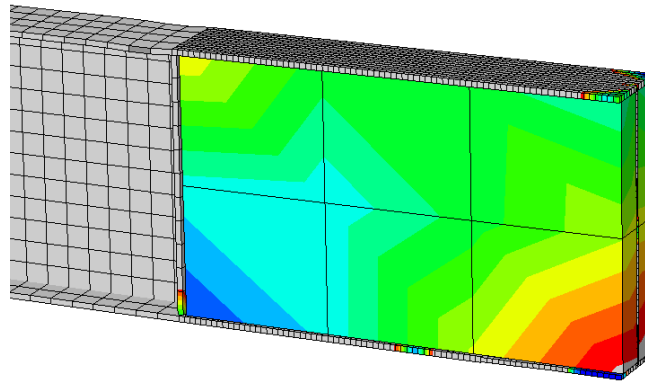
Figure 65 UHPC Encasement Repair

6.2.5 Girder 5A

Girder 5A was modeled as tested. The FE-predicted shear capacity was 200 kips. The specimen failed by concrete crushing (Figure 66). The steel web and internal reinforcing bars remained elastic. The testing resulted in a shear capacity of 199 kips.



a) bearing region shown with concrete elements hidden



b) bearing region with maximum stress plot set to f'_c
note: concrete crushing and strut formation

Figure 66 NSC Encasement Repair

6.3 Modeling Archetypal Plate Girders

The modeling campaign was extended to consider the archetypal 54 in. deep plate girder described in Section 2.3. The model results are compared against AASHTO capacity predictions and are summarized in Table 23. As with the test specimen modeling, the models are shown to be relatively robust, capturing limit states and capacities well.

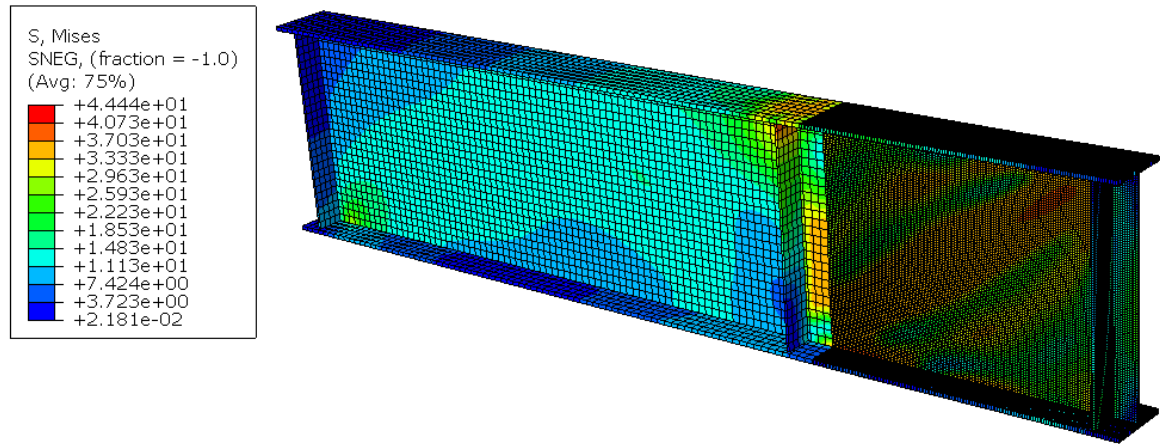
Table 23 Summary of Predicted Capacities for Plate Girder Modeling

model	FE-predicted		AASHTO-predicted	
	capacity (kips)	limit state	capacity (kips)	limit state
undamaged steel	183	web shear	186	web shear
damaged steel with bearing stiffener	100	web yield	99	web yield
damaged steel without bearing stiffener	45	web crippling	80	web shear
			37	web crippling
			99	web yield
conventional steel repair	297	tension field	296	tension field ^a
HPC repair replacing bearing stiffener only	244	tension field	226	web shear
NWC repair	250	web yield	253	web shear
^a AASHTO does not address tension field action in an end panel				

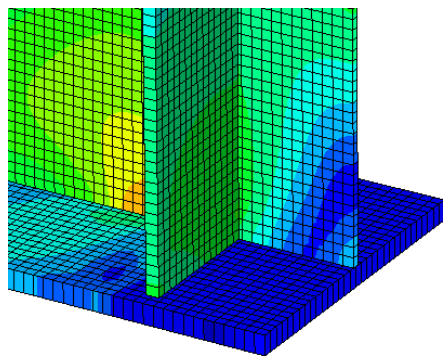
The unrepaired models highlight the complexity of interactions between limit states not captured in standard design equations. In particular, the constraining effects of undamaged regions on the corrosion-damaged regions appears to be captured in the FE models. The models indicate that the repair techniques considered are able to restore the undamaged capacity of the steel plate girders.

6.3.1 Undamaged Plate Girder

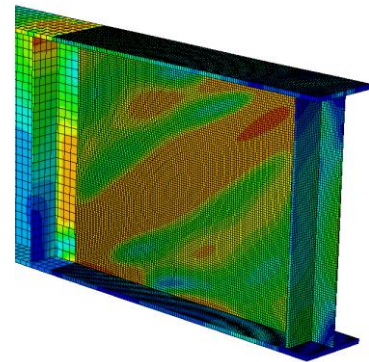
The undamaged plate girder was modeled with the load applied $1.5D = 81$ in. from the centerline of the bearing. The FE-predicted shear capacity was 183 kips in shear (measured as the reaction at the bearing). As seen in Figure 67, local web yield is evident at the bearing although the bearing stiffener remains mostly elastic. The predicted failure is web shear of the panel. The AASHTO-predicted capacity of this section is 186 kips.



a) girder elevation with maximum (von Mises) stresses plotted



b) bearing region detail (stress plot)



c) tension field action evident

Figure 67 Undamaged Girder Predicted Behavior at Failure

6.3.2 Case I Archetypal Damage

The damaged plate girder was modeled based on the archetypal damage described in Section 2.3. The FE-predicted capacity was 100 kips and failure, shown in Figure 68 was characterized as web yield, followed by crippling. Without the bearing stiffener present, the AASHTO-predicted web yield capacity for this case is 99 kips.

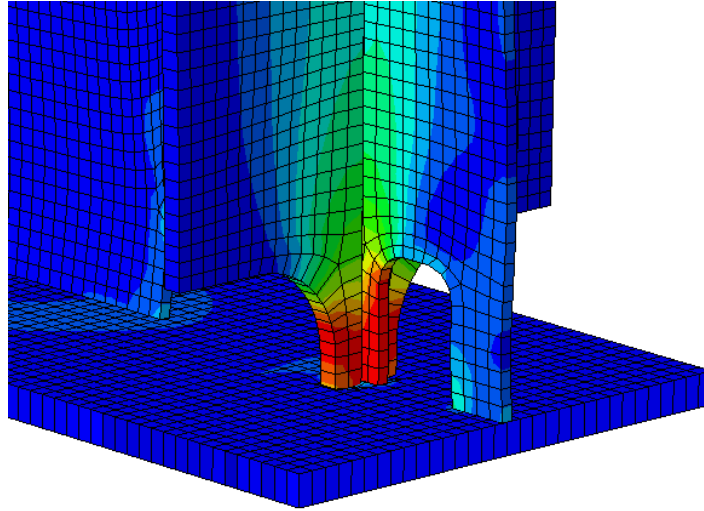


Figure 68 Bearing Region Failure of Case I Archetypical Damage (stress plot on deformed model)

Repeating this analysis without the bearing stiffener, the FE-predicted capacity falls to 45 kips and web instability is clearly evident. For this case, without a stiffener, the AASHTO-predicted web crippling capacity is 37 kips, the web yield capacity is 99 kips while the web shear capacity is approximately 80 kips.

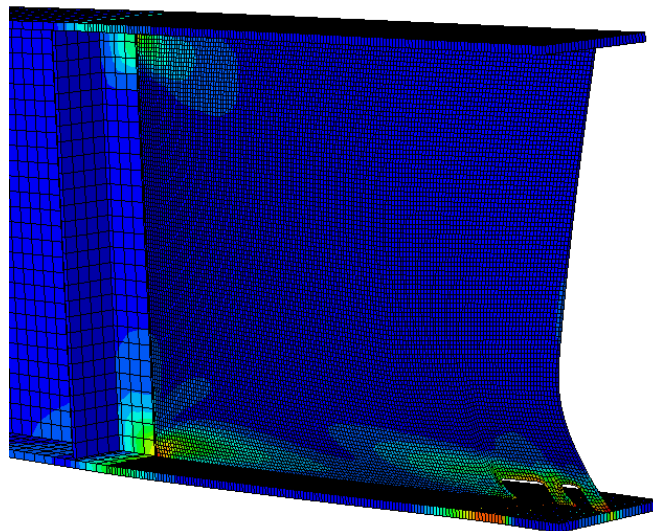


Figure 69 Failure of Case I Damaged Girder without Bearing Stiffener (stress plot on deformed model)

6.3.3 Conventional Bolted Steel Repair

Bolted steel repairs are modeled in the same manner as the substrate steel using actual geometry, S4R elements, and the same isotropic material model. Mesh size matches the substrate steel and bolts are modelled using tie constraints. Normal compression is transferred through ‘hard contact’.

The repair details, shown in Figure 75a are those used to repair Bridge D in the field¹. The 7 x 5/8 in. bearing stiffeners are replaced with considerably stiffer L9.5x5x3/4 SLBB angles. Section loss to the lower region of the 3/8 in. web is repaired with 0.5 in. bent plates, extending 12 in. up the web and across the full width of the flange, on both sides of the web.

Not surprisingly, considering the significant stiffening effect of the repair, the FE-predicted capacity increased to 297 kips. At 297 kips, a tension field has clearly developed in the shear panel as can be seen in Figure 70b. Clearly, the conservatively designed repair plates have mitigated web yield and crippling.

¹ the author of this thesis executed this design in his role as a consulting engineer.

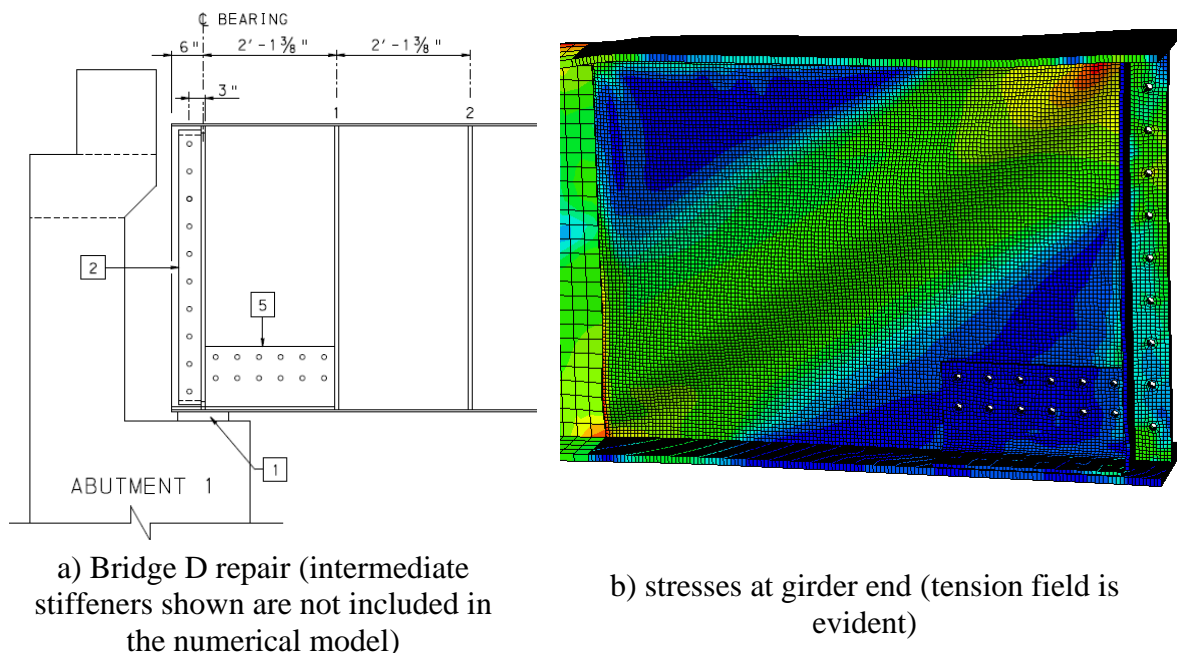


Figure 70 Bolted Steel Repair

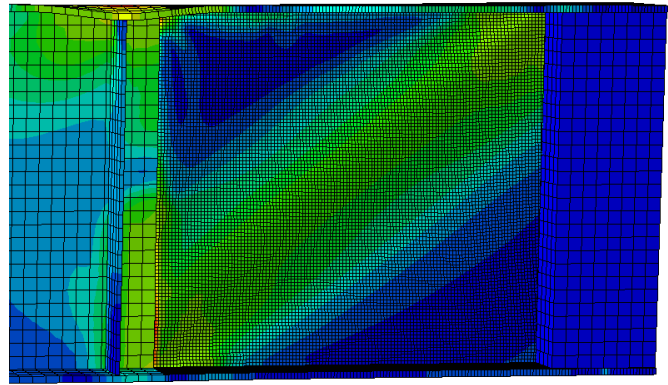
6.3.4 UHPC Encasement

The UHPC encasement modeled is similar to the full height repairs proposed and tested by McMullen and Zaghi (2020) and shown in Figure 71a. In this model, unreinforced 19 ksi UHPC was modeled. The UHPC columns extend the full height of the web, the full breadth of the flanges, and 16 in. along the length of the beam. Four vertical rows of bolted studs are used in the undamaged region of the web. The stud spacing is 8 inches vertically and 4 inches horizontally (Figure 71c).

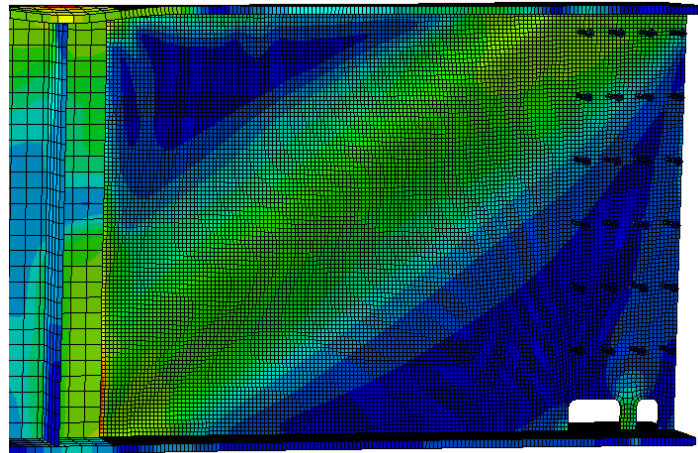
The FE-predicted capacity was 244 kips, exceeding the 183 kip capacity of the undamaged girder. As was reported in McMullen and Zaghi, the model shows evidence that tension field action was being developed over the shorter shear panel bounded by the UHPC and bearing stiffener at the load point (Figure 71b).



a) full height UHPC repair McMullen and Zaghi (2020)



b) Failure of UHPC encasement repair (stress plot on deformed model)



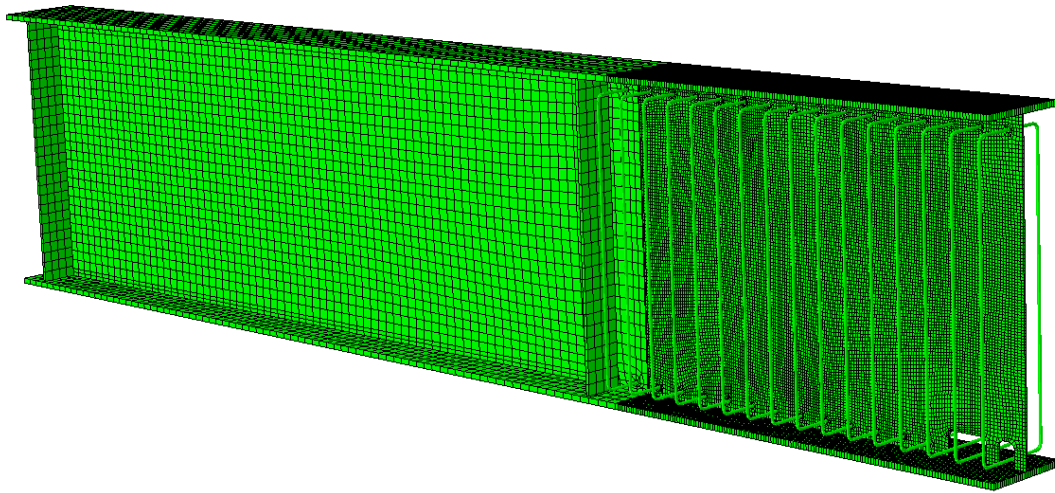
c) UHPC hidden

Figure 71 UHPC Encasement Repair

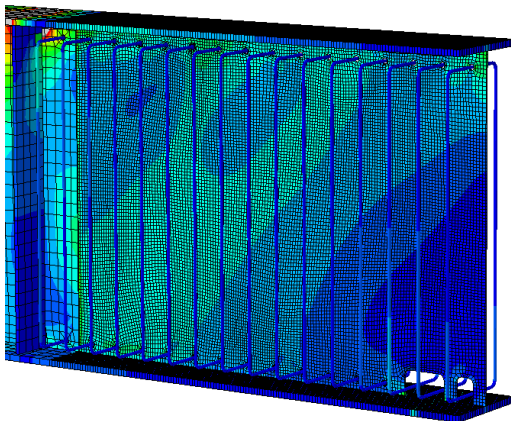
6.3.5 NSC Encasement

In this model, the loaded girder end region was encased in 5 ksi normal strength concrete (Figure 72a). The reinforcement detail includes conventional 60 ksi hairpins passing through the web. This detail provides reinforcement development, continuity through the web, and eliminates the need for shear studs.

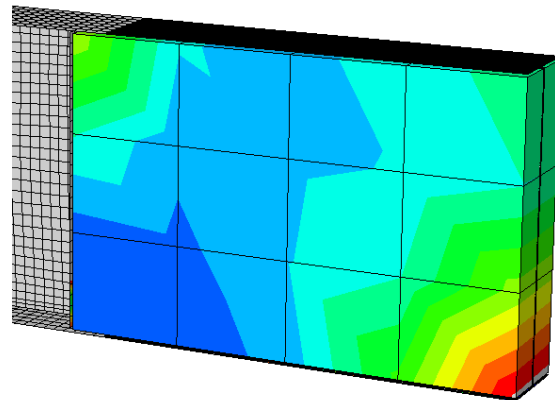
The FE-predicted capacity was 250 kips. The concrete encasement provided adequate lateral support to the damaged web. The web remained stable over its entire depth. Figure 72c shows the stress in the embedded reinforcement.



a) overall view of NSC encased model (concrete hidden)



b) hairpin details used as internal reinforcement; concrete hidden



c) bearing region with maximum stress plot set to f'_c
note: concrete crushing and strut formation

Figure 72 NSC Encasement Repair

6.3.6 Tension Field Action

AASHTO LRFD (2020) does not recognize the potential increase in strength afforded by the development of tension field action in the end panel of a steel girder. Typically, the bearing stiffener is not sufficiently stiff to permit the full development of tension field action since there is little or no inherent resistance to the out-of-balance horizontal force developed at the top flange-web-stiffener junction. In the case of a very stiff bearing stiffener replacement, however, greater tension field action can be developed.

The conventional bolted steel repair is likely overdesigned (an actual field design was modelled) and was stiff enough to permit the development of full tension field action in the girder shear panel and to mitigate local yield and crippling. Based on AISC (2016) calculations, the capacity of the modeled girder including the effects of tension field action is 306 kips (296 kips if AASHTO shear capacity, $0.58F_y$ versus $0.6F_y$, is prescribed). The FE modelled predicted a capacity of 297 kips.

Although AASHTO does not permit tension field action to be considered in design, the numerical analyses presented are able to capture this behavior and should, therefore, illustrate the degree of conservativeness in actual repair designs. The tension field develops because the bearing stiffener is sufficiently stiff about an axis perpendicular to the plane of the web to anchor the unbalanced force imparted by the tension field at the top flange-web-stiffener junction. Additionally, the stiffener must have sufficient flexural stiffness about an axis in the plane of the web to restrain web buckling. Table 24 compares the effective flexural stiffnesses (EI/L) of the bearing stiffeners provided in the conventional steel repair model. The calculations shown in Table 24 reinforce the fact that web buckling can be mitigated with relatively small amounts of lateral

support. Furthermore, the results suggest additional design criteria for repairs that may be appropriate for engaging tension field action.

Table 24 Bearing Stiffener Stiffness and Observed Behavior

	as built	bolted steel
stiffener	7 x 5/8 both sides	L9.5x5x3/4 SLBB
L, in.	54	54
E, ksi	29,000	29,000
I_x (in plane of web), in ⁴	143	457
EI_x/L , k-in	76,800	245,000
adequate to resist web buckling at web shear capacity	yes	yes
I_y (perpendicular to web), in ⁴	0.35	37.8
EI_y/L , k-in	188	20,300
adequate to develop tension field behaviour	no	full tension field developed
FE-predicted shear capacity, kips	183	297
nominal design shear capacity, kips	186	296

6.3.7 Concrete Encasement

Concrete encasement provided lateral restraint to the slender web and permitting continuity of force flow through the damaged region. The behavior observed manifests as an increase in shear capacity. This increase in capacity results from a combination of controlling web buckling and the reduction in the length of the shear panel. Essentially, the encasement acts as a wide bearing stiffener. Table 25 summarizes the effective shear panel length and corresponding shear strength of the exposed steel web for the archetypal models. The beam capacity is easily restored, and the concrete remains largely undamaged. The reinforcing bars remained elastic indicating the likelihood of good crack control.

Table 25 Web Shear Capacity

	as built	UHPC encased	NWC encased
shear panel length, a , in.	81	74	51
a/h	1.50	1.37	0.94
V_{cr} , kips	186	198	273
FE-predicted shear capacity, kips	183	244	250

7.0 Conclusions and Future Work

7.1 Conclusions of Experimental Results

Six girders were tested over a short shear span. For each girder, End A was tested under static load conditions to failure. If an acceptable result was achieved after testing End A, End B was fatigue conditioned for 1 million cycles and subsequently tested to failure in a similar manner to End A.

The AASHTO-prescribed shear capacity of uncorroded control Girder 1A is $V_{cr} = 257$ kips, corresponding to $v_{cr} = 30.8$ ksi. The crippling ($R_{crip} = 91$ kips ($v = 11.8$ ksi)) and yield ($R_{yield} = 140$ kips ($v = 18.2$ ksi)) capacities at the bearing are lower than this although both can be mitigated by providing bearing stiffeners. The AASHTO-prescribed capacity of the bearing stiffeners provided in 1A is $P_{sb} = 150$ kips ($v = 19.5$ ksi) and the bearing capacity is $R_{sb} = 175$ kips ($v = 22.7$ ksi). Thus the in situ as-built AASHTO-prescribed capacity is 150 kips ($v = 19.5$ ksi). The experimentally observed capacity exceeded this and approached the critical buckling capacity; indeed, evidence of initial buckling of the girder web was observed. The following conclusions are drawn from the experimental study:

1. Corrosion-damaged 2A exhibited a load bearing capacity of only 7% of that of undamaged girder 1A. Initial stiffness of 2A was 20% that of 1A.
2. Each of repairs 3A (steel), 4A (UHPC) and 5A (RC) effectively restored the load bearing capacity of corrosion-damaged 2A to that of the undamaged girder 1A. Tests were stopped before the ultimate capacity could be achieved in each case to permit testing of End B.

3. Each of 3A, 4A and 5A also achieved comparable (although marginally reduced) stiffness to 1A. The loss of stiffness may be associated with the fact that the monotonic tests are also ‘shakedown cycles’ for the installed strengthening.
4. Each of the repairs 3B (steel), 4B (UHPC) and 5B (RC) exhibited little deterioration associated with the one million cycles fatigue conditioning performed. 5B exhibited minor cracking.
5. Following fatigue conditioning, each of 3B, 4B and 5B, exceeded the load bearing capacity of 1A.
6. The stiffness of 3B, 4B and 5B exceeded that of the End A tests and 4B and 5B exceeded that of 1A. This confirms the ‘shakedown’ effect of the fatigue conditioning.
7. GFRP-repaired 6A exhibited a catastrophic debonding failure at 42% of the load bearing capacity of 1A. Up to this debonding, behavior was comparable to 1A. Subsequently, 6B was not tested.

7.2 Conclusions of Numerical Modeling Results

Following testing, extensive finite element modeling was conducted and validated based on the experimental program. The modeling of the test specimens proved to be robust and captured observed behavior well. Once the test specimen modeling was “benchmarked” against the observed behavior, the models were expanded to archetypal plate girders to verify the validity of the repair methods. The following conclusions are drawn from the numerical modeling:

1. The modelling approach was sufficiently robust to capture behaviors of interest. Apart from the need for good geometric modeling of section loss, the FE models demonstrated required little special calibration.
2. The models additionally confirmed the validity of adopting AASHTO prescribed equations (described in Section 1.3) for estimating residual capacity of damaged girder ends.
3. Development of tension field action was observed in the steel repair and UHPC repair. Such behavior requires stiff end bearings. The steel angles used for bolted-steel and the stiff UHPC column resulted in sufficient stiffness to anchor the tension field at the top flange-web-stiffener junction.
4. Stability of the steel web through encasement was achieved in the UHPC and reinforced concrete repairs.

7.3 Qualitative Assessment of Repair Methods

In order to assess the pros and cons of each repair strategy, a qualitative assessment was assembled and shown in Table 26. This assessment is based on the experience of the research team designing, fabricating and testing the specimens. The bolted steel repair and UHPC repair provide excellent structural performance while the reinforced concrete repair provided very good structural performance. All were able to restore the design capacity of the undamaged girder. The FRP is inadequate due to catastrophic debonding. For the three viable repair options, all have the capability to provide adequate stiffness to develop tension field action. This results in the repairs exhibiting some reserve capacity since AASHTO does not allow tension field behavior to be considered in an end panel. Furthermore, all methods can be easily designed, require no special

tooling, and contractors generally have familiarity with materials and fabrication processes. UHPC can be costly and specialty contractors may be required for proprietary mixes.

For the UHPC repair, it has been shown that bolted shear connectors are an adequate alternative to welded shear studs. Providing through-web hairpin details for reinforced concrete appears to alleviate the need for shear studs. Both approaches avoid the need for hot work under the bridge.

It is important to note that the steel repair and reinforcing used in the reinforced concrete repair remain susceptible to corrosion if not properly maintained. All viable repair options are nonetheless susceptible to crevice corrosion if interfaces are not properly sealed and maintained.

Taking all factors into account, the author proposes that a conventional bolted steel repair will typically be adequate to restore girder bearing region capacity for an extended life. UHPC is viable but only likely when deployed on site for other uses such as precast deck closure pours. Regardless of repair method selected, none will be successful without first correcting the cause of the deterioration.

Table 26 Quantitative Assessment of Repair Techniques

consideration/parameter	repair technique			
	bolted steel	UHPC encasement	concrete encasement	bonded FRP
structural performance	excellent	excellent	very good	inadequate
performance concerns	corrosion	none	cracking/corrosion	debonding
practical limitation on capacity restored	no	no	high shear may exceed capacity	bond-limited behaviour
develop tension field capacity of end web panel	yes	yes	yes	no
load sharing between beam and repair	possible	no	yes	no
restore or provide bearing stiffener	yes	yes	yes	marginal
<i>potentially</i> fatigue sensitive details	unlikely	no (yes if welded studs used)	no (yes if welded studs used)	adhesive bond line
globally susceptible to further corrosion	yes	no	no	no
susceptible to crevice corrosion around edges of repair	yes	yes	yes	no with good detail
design type	quantitative	prescriptive	semi prescriptive	quantitative
design complexity	easy	easy	easy	moderate
existing design standards applicable or adaptable to technique	AASHTO	no (McMullen 2019)	partially AASHTO	no (FCAPS and C595)
potential for BC/BD standard development	good	very good	very good	good
new Bulletin 15 approvals needed	no	yes	no	yes
practical limitations on beam depth	no	d > 18"	d > 18"	no
address <i>large areas</i> of 100% section loss	yes	yes	yes	yes
shop prefabrication of components	yes	no	no	yes
bespoke adjustment on site	limited	yes	yes	yes
jacking <i>during</i> repair if designed to carry portion of existing load	bolted: no welded: yes	yes	yes	yes

Table 26 (continued)

SSPC surface preparation required	SP3	SP3	SP3	SP5
additional surface treatment required	no	no	no	silane treatment
permitted surface amplitude variation	$\approx 1/16''$	any	any	$\approx 1/8''$
minimum web thickness	none	none	none	none
hot work required	bolted: no welded: yes	no (yes if welded studs used)	no (yes if welded studs used)	no
drilling or machining of existing web (in addition to surface treatment)	yes	no (yes if bolted studs used)	yes	no
power tools larger than 'hand tools' required	no	no (except concrete mixer)	no (except concrete mixer)	no
handling equipment under deck	yes	no	no	possibly
possible interference handling materials in confined area including jacking	yes	not likely	not likely	not likely
concrete placement access required	no	yes	yes	no
formwork required	no	yes	yes	no
sensitivity to temperature and RH during application	no	requires special handling outside range $50^{\circ}\text{F} < T < 85^{\circ}\text{F}$	$>38^{\circ}\text{F}$	$>\approx 50^{\circ}\text{F}$ $> \text{dew point}$
estimated time on site for one beam end	bolted: 1d welded: multiple days	multiple days	multiple days	one day
cure time	none	12h	3-7d	24h
<i>possible</i> OSHA regulated activities <i>not typical</i> of bridge repair	no	particulate	no	inhalant particulate
specialized contractor required	no	yes	no	possibly
proprietary materials required	no	yes	no	no
contractor familiarity	high	moderate	high	low
need for special contractor certification or oversight	no	yes	no	possibly (adhesive handling)
construction inspectability	good	specialist	good	good

Table 26 (continued)

special QC/QA requirements	no	yes	no	yes
in service inspectability	good	good	good	good
special/unfamiliar inspection techniques required	no	no	no	yes
frequency of preventative maintenance	as steel	none	none	similar to steel
compatible with future painting and maintenance	yes	yes	yes	possible painting issues
compatible with future bearing replacement	yes	possible issues	possible issues	yes
estimated design life	50 yr	50+ yr	50 yr	25-50 yr
demonstration projects available	yes	yes	none known	none known
overall perceived complexity	easy	moderate/difficult	easy/moderate	moderate
perceived relative cost	\$	\$\$\$	\$\$	\$\$

7.4 Future Work

Further studies are required to verify the application of the proposed repair methods for different situations encountered in the field. Not all bridge girders are built with a conventional bearing and stiffener arrangement as presented in this study. Some bridge structures, as described in Chapter 2, utilize encased girder ends and integral abutments. Repair of these introduce different objectives and challenges.

Design implementation is required. Proposing a standard for each of the viable repair methods that state departments of transportation and practicing engineers could use would be beneficial. For the steel repair, member sizes such as the repair angles and plates could be detailed on the standard along with bolt size and spacing. Minimum stiffness requirements to achieve tension field action need to be established. For the UHPC repair, the length of the repair along with

bolted shear stud and/or welded shear stud spacing can be detailed. Finally, for the reinforced concrete repair, concrete specifications, dimensions, and hairpin details can all be standardized.

Field implementation of the proposed repair methods is also required. Contactor comments on ease of fabrication and constructability would be highly valuable – supplementing and revising the qualitative assessment presented in Table 26. Finally, once the proposed repair method is in place, long term durability can be monitored during the routine bridge inspection that is required of all bridges.

Appendix A - Test Specimen Fabrication Drawings

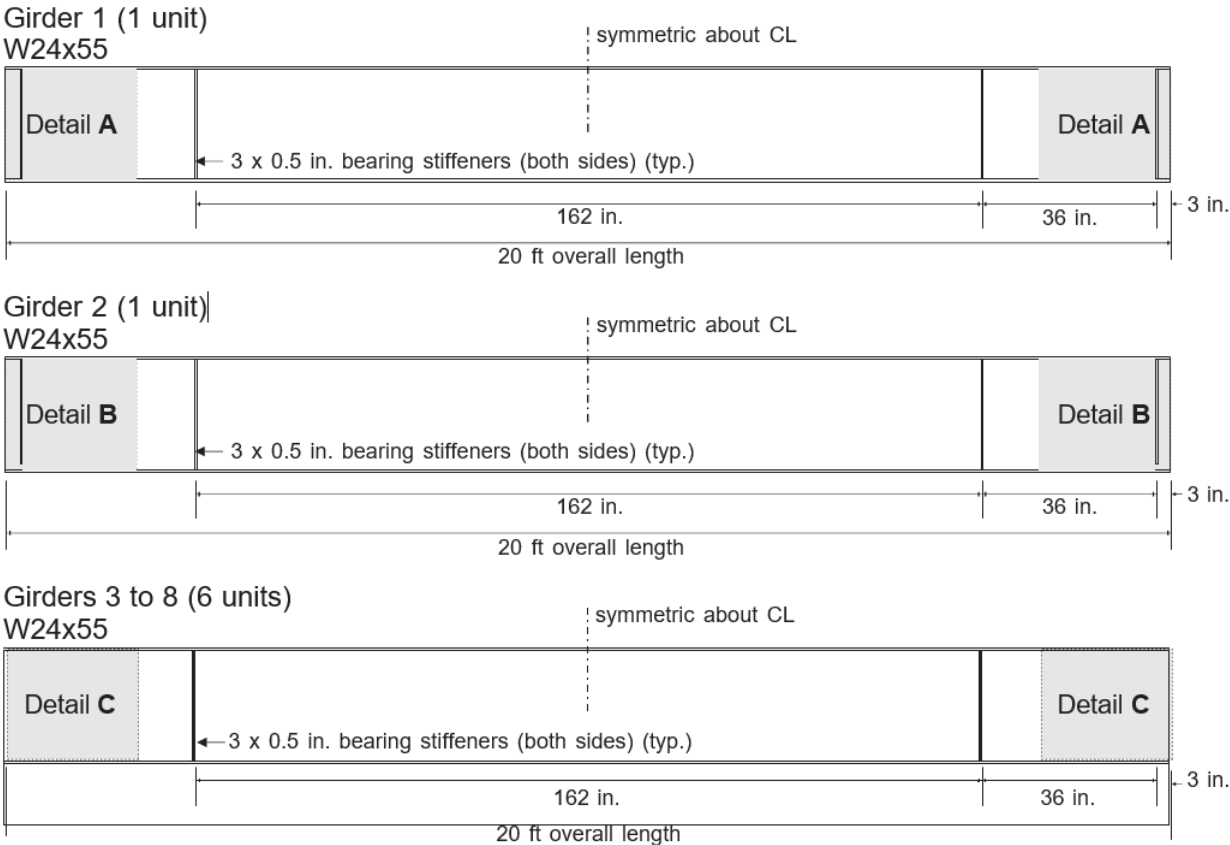


Figure 73 Test Specimen Fabrication Drawings

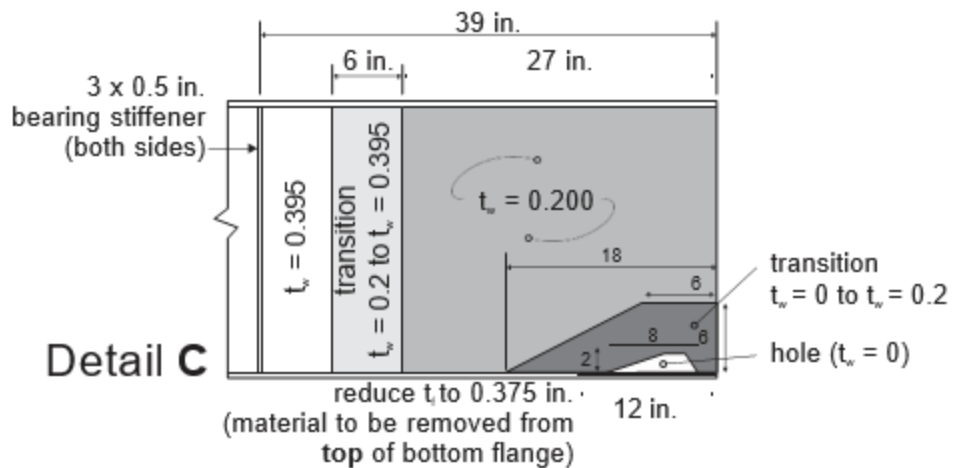
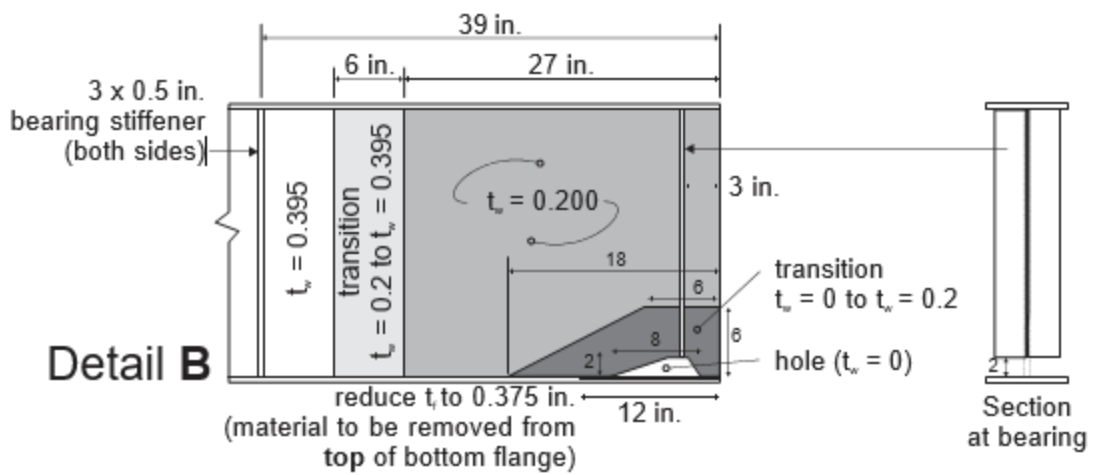
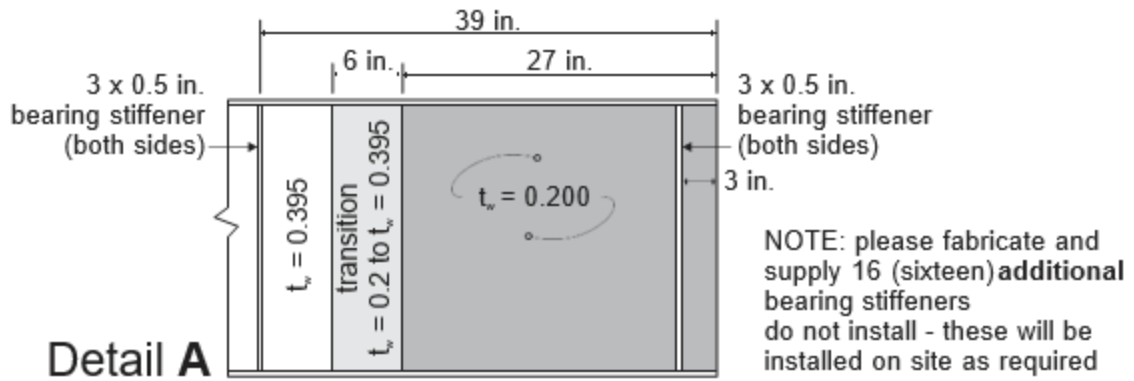
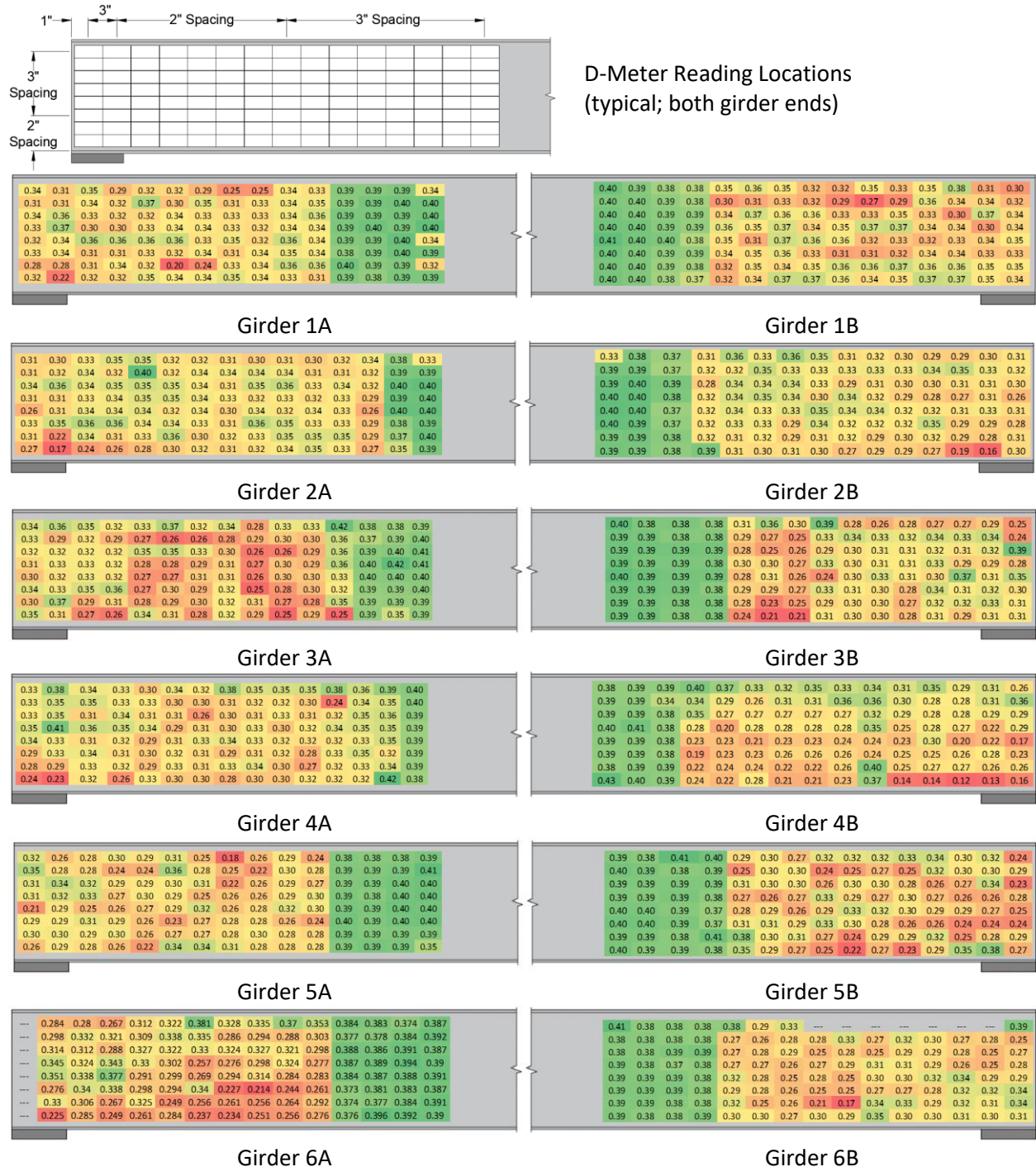


Figure 74 Test Specimen Fabrication Details

Appendix B - Test Specimen Web Thickness Measurements

Table 27 Test Specimen Web Thickness Measurements



Bibliography

AASHTO (2020) LRFD Bridge Design Specifications, 9th edition.

ABAQUS (2020) ABAQUS User's Manual.

https://help.3ds.com/2020/English/DSSIMULIA_Established/SIMULIA_Established_FrontmatterMap/sim-r-DSDocAbaqus.htm?ContextScope=all [login/license required]

ABAQUS (2011) ABAQUS Analysis User's Manual, Volume III: Materials. 22.6.1-2 pp

ACI Committee 318 (2019). Building Code Requirements for Structural Concrete (ACI 318-14) and Commentary (ACI 318r-14), American Concrete Institute.

ACI Committee 215, (2022). ACI PRC 215R-22 *Considerations for Design of Concrete Structures Subjected to Fatigue Loading*

ACI Committee 363 (2010). ACI 363R-10 Report on High Strength Concrete, American Concrete Institute.

Ahn, J-H, Kim, I-T, Kainuma, S. and Lee, M-J (2013) Residual shear strength of steel plate girder due to web local corrosion, *Journal of Constructional Steel Research*, 89, 198-212.

American Welding Society (2015) Structural Welding Code - Steel.

ANSI/AISC 360-16 (2016) Specifications for Structural Steel Buildings, American Institute of Steel Construction.

Australian Standard. (2004). Bridge Design. Part 6: Steel and Composite Construction.

ASCE Fiber Composites and Polymers Standards (FCAPS) Committee. Forthcoming *LRFD Standard for Pultruded GFRP Members*.

Bao, A., Gulasey, M., Guillaume, C., Levitova, N., Moraes, A. and Satter, C. (2018) Structural Capacity Analysis of Corroded Steel Girder Bridges, *Proceedings of the 3rd International Conference on Civil, Structural and Transportation Engineering (ICCSTE'18)*, Niagara Falls, Canada – June 10 – 12, 2018, Paper No. 118.

Barth, K. (2015) Steel Bridge Design Handbook Design Example 2A: Two-Span Continuous Straight Composite Steel I-Girder Bridge, *FHWA-HIF-16-002-Vol 21*.

Bedford Reinforced Plastics (2012) *Design Guide*. https://bedfordreinforced.com/app/uploads/2017/07/BRP_Design-Guide.pdf

Bischoff, P. H. (2003) Tension stiffening and cracking of steel fiber reinforced concrete, *ASCE Journal of Materials in Civil Engineering*, **15**(2), 174–182.

- Cadei, J.M.C., Stratford, T.J., Hollaway, L.C. and Duckett, W.G. (2004) Strengthening Metallic Structures Using Externally Bonded Fibre-Reinforced Polymers. CIRIA Pub. No. C595. 233 pp.
- Cardoso, D., Harries, K.A. and Batista, E. (2014) Closed-Form Equations for Local Buckling of Pultruded Thin-Walled Sections, *Thin-walled Structures*, **79**, 16-22.
- Cunningham, D., Harries, K.A. and Bell, A.J., (2015) Open-Hole Tension Capacity of Pultruded GFRP Having Staggered Hole Arrangement, *Engineering Structures*, **95**, 8-15.
- Ellobody, E. (2014) Finite Element Analysis and Design of Steel and Steel-Concrete Composite Bridges, Elsevier Science and Technology, 522-525.
- El-Tawil, S., Fortney, P., Harries, K.A., Shahrooz, B.M., Kurama, Y., Hassan, M. and Tong, X. (2009) Recommendations for Seismic Design of Hybrid Coupled Wall Systems, ASCE/SEI, 80 pp.
- Eurocode 4 (EC4) (2005). 1994-2:2005 Design of Composite Steel and Concrete Structures, Part 2 – General Rules and Rules for Bridges
- Fernando D., Yu T., Teng J.G. and Zhao X-L (2009) CFRP strengthening of rectangular steel tubes subjected to end bearing loads: effect of adhesive properties and finite element modelling. *Thin-Walled Structures*, 47(10), 1020–8.
- Federal Highway Administration (FHWA) (2021) https://www.fhwa.dot.gov/innovation/everydaycounts/edc_6/uhpc_bridge_preservation.cfm accessed 4.15.21.
- Federal Highway Administration (FHWA) (2019) <https://highways.dot.gov/research/structures/ultra-high-performance-concrete/ultra-high-performance-concrete> accessed 6.19.20.
- Fry, G.T., Bailey, B.M., Farr, J.L., Elliott, J.E. and Keating, P.B. (2005) Behavior and design of dapped steel plate girders. *Report FHWA/TX-05/0-2102-1*, Texas Transportation Institute, Texas A&M University. 174 pp.
- Gerasimidis, S. and Brena, S. (2019) Development of Load Rating Procedures for Deteriorated Steel Beam Ends, massDOT Report 19-008, 278 pp.
- Graybeal, B.A. (2014) Design and Construction of Field-Cast UHPC Connections. FHWA-HRT-14-084.
- Grubb, M.A. and Schmidt, R.E. (2015) Steel Bridge Design Handbook Design Example 1: Three-Span Continuous Straight Composite Steel I-Girder Bridge, *FHWA-HIF-16-002-Vol 20*.
- Haber, Z.B., De La Varga, I., Graybeal, B.A., Nakashoji, B. and El-Helou, R. (2018) Properties and Behavior of UHPC-Class Materials, FHWA-HRT-18-036
- NACE International (2006) Joint Surface Preparation Standard https://webstore.ansi.org/preview-pages/NACE/preview_NACE+No.+1+SSPC-SP+5.pdf accessed 4.12.22

- Hain, A. and Zaghi, A.E. (2021) Learnings from the Field Implementation of a Novel UHPC Beam End Repair on a Corroded Steel Girder Bridge in Connecticut, *TRB Annual Meeting Presentation*, <https://www.youtube.com/watch?v=wIU9CgIITmI>, accessed 4.15.21.
- Harries. K.A., Mash, J.A. and Rogers, C. (2022) Repair Strategies for Corroded Steel Bridge Girder End Regions. *PennDOT Final Report [number to be determined]*.
- Harries, K.A. and Dawood, M., (2012) Behavior and Performance of FRP-to-Steel Bond, Transportation Research Record: Journal of the Transportation Research Board 2313/2012, 181-188.
- Hsu, L.S. and Hsu, C.-T.T. (1994). Complete stress-strain behaviour of high-strength concrete under compression. *Magazine of Concrete Research*, **46** (169), 301-312.
- Khurram, N., Sasaki, E., Katsuchi, H. and Yamada, H. (2014) Experimental and Numerical Evaluation of Bearing Capacity of Steel Plate Girder Affected by End Panel Corrosion, *International Journal of Steel Structures*, 14(3), 659-676.
- Kim, I-T., Lee, M-J. Ahn, J-H. and Kaiuma, S. (2013) Experimental evaluation of shear buckling behaviors and strength of locally corroded web, *Journal of Constructional Steel Research*, 83, 75-89.
- Kruszewski, D. (2018) Performance Evaluation of Shear Connectors Embedded in Ultra-High Performance Concrete as Part of a Bridge Repair Method. PhD Dissertation, University of Connecticut, 281 pp.
- Kulicki, J.M., Prucz, Z., Sorgenfrei, D.F., Mertz, D.R. and Young, W.T. (1990) Guidelines for evaluating corrosion effects in existing steel bridges, NCHRP Report 333, Transportation Research Board.
- Kupfer, H. B. and K. H. Gerstle (1973) Behavior of Concrete under Biaxial Stresses, *ASCE Journal of Engineering Mechanics Division*, **99**, 853.
- Latif, W., White, D. (2021) Flange Local Buckling Resistance and Local-Global Buckling Interactions in Slender-Flange Welded I-Section Beams, *AISC Engineering Journal*, 59, 121.
- Liu, C., Miyahita, T. and Nagai, M. (2011) Analytical Study on Shear Capacity of Steel I-Girders with Local Corrosion nearby Supports, *Procedia Engineering*, 14, 2276-2284.
- McMullen, K.F. (2019) Full-Scale Evaluation of a Novel Repair for Corroded Plate Girders with UHPC, PhD Dissertation, University of Connecticut, 288 pp.
- McMullen, K.F. and Zaghi, A.E. (2020) Experimental Evaluation of Full-Scale Corroded Steel Plate Girders Repaired with UHPC, *ASCE Journal of bridge Engineering*, 25(4): 04020011
- Nayal, R. and Rasheed, H.A. (2006) Tension Stiffening Model for Concrete Beams Reinforced with Steel and FRP Bars. *ASCE Journal of Materials in Civil Engineering*, **18**(6), 831-841.

- Okeil, A., Bingol, Y., and Ferdous, M. (2009) Novel Technique for Inhibiting Buckling of Thin-Walled Steel Structures Using Pultruded Glass FRP Sections. *ASCE Journal of Composites for Construction*, 13(6), 547–557.
- Pavlovic, M., Markovic, Z., Veljkovic, M., and Budevaca, D. (2013) Bolted shear connectors vs. headed studs behaviour in push-out tests, *Journal of Constructional Steel Research*, 88, 134-149.
- PennDOT (2019) Design Manual Part 4, PennDOT Publication 15M.
- PennDOT (2010) Bridge Maintenance Manual, PennDOT Publication No. 55.
- Provines, J.T., Ocel, J.M. and Zmerta, K. (2019) Strength and Fatigue Resistance of Clustered Shear Stud Connectors in Composite Steel Girders, FHWA-HRT-20-005.
- Russell, H.G. and Graybeal, B.A. (2013) Ultra-High Performance Concrete: A State-of-the-Art Report for the Bridge Community, FHWA-HRT-13-060.
- Sika (2020) *SikaDur 32 Product Data Sheet*, <https://usa.sika.com/en/construction/repair-protection/multi-purpose-epoxies/adhesives/sikadur-32-hi-mod.html>, accessed 11.17.21.
- Society for Protective Coatings (SSPC) (2006) *NACE No. 1/SSPC-SP 5-2006 White Metal Blast Cleaning*, SSPC, Pittsburgh, PA, 5 pp.
- Stratford, T.J. and Chen, J.F. (2005) Designing for Tapers and Defects in FRP-Strengthened Metallic Structures, *Proceedings of the International Symposium on Bond Behaviour of FRP in Structures*, Hong Kong.
- Tension Control Bolts (2022) TCB Shear Stud Data Sheet, <https://www.tcbolts.com/en/products/tcb-shear-stud>, accessed 02.10.22.
- TxDOT (2021) Ultra-High Performance Concrete for Bridge Preservation and Repair, *EDC News*, April 8, 2021.
- Tzortzinis, G., Knickle, B.T., Gerasimidis, S., Bardow, A. and Brena, S.F. (2019) Experiments and computations on steel bridge corroded beam ends, *Proceedings of the Annual Stability Conference Structural Stability Research Council*, St. Louis, Missouri, April 2019.
- Wakabayashi, D., Miyashita, T., Okuyama, Y., Kobayashi, A., Hidekuma, Y., Horimoto, W., Koide, N. and Nagai, M. (2013) Repair method using CFRP for corroded steel girder ends, *Proceedings of Fourth Asia-Pacific Conference on FRP in Structures (APFIS 2013)*, Melbourne, December 2013.
- Yamaguchi, E., Akagi, T. and Tsuji, H. (2014) Influence of corrosion on load-carrying capacities of steel I-section main-girder end and steel end cross-girder, *International Journal of Steel Structures*, 14, 831–841.

- Zhao X-L, Fernando D. and Al-Mahaidi R. (2006) CFRP strengthened RHS subjected to transverse end bearing force. *Engineering Structures*, 28(11),1555–65.
- Zhao, X-L and Zhang, L. (2006) Sate-of-the-art review on FRP strengthened steel structures, *Engineering Structures*, 29, 1808-1823.
- Zmert, K.M. (2015) Repair of Corrosion Damaged Steel Bridge Girder Ends by Encasement in Ultra-High Strength Concrete, PhD Dissertation, University of Connecticut, 349 pp.
- Zmert, K.M., McMullen, K.F., Zaghi, A.E. and Wille, K. (2017) Experimental Study of UHPC Repair for Corrosion-Damaged Steel Girder Ends, *ASCE Journal of Bridge Engineering*, 22(8), 04017037.